

**PERYLENE-BASED MATERIALS:
POTENTIAL COMPONENTS IN ORGANIC ELECTRONICS AND
OPTOELECTRONICS**

**A Thesis
Presented to
The Academic Faculty**

by

Zesheng An

**In Partial Fulfillment
of the Requirements for the Degree
Doctor of Philosophy in the
School of Chemistry and Biochemistry**

**Georgia Institute of Technology
December, 2005**

Copyright©Zesheng An 2005

**PERYLENE-BASED MATERIALS:
POTENTIAL COMPONENTS IN ORGANIC ELECTRONICS AND
OPTOELECTRONICS**

Approved by

Dr. Seth R. Marder, Advisor
School of Chemistry and Biochemistry
Georgia Institute of Technology

Dr. Jean-Luc Brédas
School of Chemistry and Biochemistry
Georgia Institute of Technology

Dr. Uwe H. F. Bunz
School of Chemistry and Biochemistry
Georgia Institute of Technology

Dr. Bernard Kippelen
School of Electrical and Computer Engineering
Georgia Institute of Technology

Dr. Joseph Perry
School of Chemistry and Biochemistry
Georgia Institute of Technology

August 17, 2005

ACKNOWLEDGEMENTS

I have been always feeling lucky that I have Dr. Seth Marder as my advisor. During my four years of working with him, I have learnt tremendous things from him, ranging from how to think about science in general to small skills such as how to use laser pointer in a presentation. It is always a pleasure to talk with Seth on various aspects of chemistry and life. Seth's enthusiasm about and dedication to science and education have greatly influenced me, people surrounding him and people who know him.

Five years is not a short time in a person's life. Fortunately, I have my wife Xiaolan with me over this important period of time. Because of her love, I could smile over all the difficulties I encountered and walk forward.

The thesis is a product of collaborations with other groups. I appreciate the SCLC data provided by Prof. Bernard Kippelen and Dr. Junsheng Yu at Georgia Institute of Technology, and the transient absorption data provided by Prof. Michael R. Wasielewski and Dr. David McCamant at Northwestern University. Also I am thankful for my committee members providing valuable suggestions on my thesis and for Susan proofreading my thesis. I would like to thank Simon for taking some XRDs, Qing for providing one starting material, Steve, Xiaowei and Sungae for participating in my Marderization sessions and other group members for their help. I also appreciate Prof. Uwe H. F. Bunz and the Bunz group for their help on DSC.

TABLE OF CONTENTS

ACKNOWLEDGEMENTS	iii
LIST OF TABLES	vii
LIST OF FIGURES	viii
LIST OF SCHEMES	xiii
LIST OF SYMBOLS AND ABBREVIATIONS	xiv
SUMMARY	xvi
CHAPTER 1 INTRODUCTION	
1.1 Organic semiconductors	1
1.2 Charge transport in organic semiconductors	5
1.3 Liquid crystals	10
1.4 Rationale for using discotic liquid crystals as charge transport materials	13
1.5 Charge carrier mobility characterization methods	15
1.6 Charge carrier mobilities of liquid crystals	23
1.7 Alignment of discotic liquid crystals	28
1.8 Organization of the thesis	31
1.9 References	33
CHAPTER 2 ROOM-TEMPERATURE DISCOTIC LIQUID CRYSTALLINE PERYLENE DIIMIDES AS ELECTRON-TRANSPORT MATERIALS	
2.1 Introduction	39
2.2 Synthesis	41

2.3 Absorption properties	43
2.4 Electrochemical properties	45
2.5 Liquid crystalline properties	47
2.6 SCLC characterization	51
2.7 Concluding remarks	54
2.8 Experimental	55
2.9 References	61
 CHAPTER 3 DISCOTIC LIQUID-CRYSTALLINE CORONENE DIIMIDES AS CHARGE-TRANSPORT MATERIALS	
3.1 Introduction	64
3.2 Synthesis	67
3.3 Absorption and emission properties	71
3.4 Electrochemical properties	74
3.5 Aggregation behavior	76
3.6 Liquid crystalline properties	82
3.7 SCLC characterization	88
3.8 Concluding remarks	90
3.9 Experimental	92
3.10 References	104
 CHAPTER 4 ENHANCEMENT OF CHARGE CARRIER MOBILITIES IN CORONENE DIIMIDES WITH BINARY SIDE CHAINS	
4.1 Introduction	106
4.2 Synthesis	108

4.3 Absorption and emission properties	111
4.4 Electrochemical properties	112
4.5 Liquid crystalline properties	115
4.6 SCLC characterization	121
4.7 Concluding remarks	123
4.8 Experimental	125
4.9 References	132
CHAPTER 5 DONOR-SUBSTITUTED PERYLENE DIIMIDES	
5.1 Introduction	133
5.2 Synthesis	138
5.3 UV-Vis absorption properties	139
5.4 Transient absorption properties	143
5.5 Electrochemical properties	147
5.6 Concluding remarks	149
5.7 Experimental	150
5.8 References	159
CHAPTER 6 CONCLUSIONS AND OUTLOOK	161

LIST OF TABLES

Table 1.1	Some discotic liquid crystals and their charge-carrier mobilities.	24
Table 2.1	Summary of the electrochemical data of the perylene diimide LCs vs. Fc^+/Fc .	45
Table 2.2	Summary of the phase transition temperature T [$^{\circ}\text{C}$] and transition enthalpy ΔH [kJ/mol] of PDI1 and PDI2 (second heating-cooling cycle).	48
Table 2.3	Summary of the SCLC characteristics of the perylene diimide liquid crystals.	55
Table 3.1	Summary of the absorption and emission data of the coronene diimides in dichloromethane.	73
Table 3.2	Summary of the phase transition temperature T [$^{\circ}\text{C}$] and the transition enthalpy ΔH [kJ/mol] of coronene diimides 6a - d (second heating-cooling cycle).	82
Table 3.3	Summary of the XRD data of compounds 6a - d .	88
Table 3.4	Summary of the SCLC characteristics of coronene diimide liquid crystals.	90
Table 4.1	Summary of the optical and electrochemical (vs. Fc^+/Fc) data of CDI-C8 and CDI-F7 .	115
Table 4.2	Summary of the XRD data of CDI-C8 and CDI-F7 .	121
Table 5.1	Summary of the Electrochemical data of donor-substituted compounds 1 - 4 vs Fc^+/Fc .	148

LIST OF FIGURES

Figure 1.1	Tang's OLED with a diamine as the hole-transport material and Alq ₃ as both the electron-transport and the light-emitting material.	2
Figure 1.2	Tang's photovoltaic cell with CuPc and PV as both the light-harvesting and the charge-transport materials.	3
Figure 1.3	Field-effect transistor using DCMT as a charge-transport material.	4
Figure 1.4	Schematic illustration of (A) electron transport in the conduction band of inorganic semiconductors (W_c is the bandwidth of the conduction band and W_v is the bandwidth of the valence band; E_g is the energy gap between the conduction band and the valence band); (B) discrete energy levels in organic semiconductors and (C) electron hopping through LUMO levels of organic molecules (E_g is the energy gap between the HOMO and LUMO levels).	7
Figure 1.5	(a) Illustrates a hole transfer from a charged molecule A ⁺ to a neutral molecule B via a transition state where the two molecules adopt the same geometry. (b) illustrates the energy potential change ongoing from neutral to charged molecules.	9
Figure 1.6	Schematic representations of a nematic discotic mesophase and a macrocyclic molecule that forms a nematic phase.	11
Figure 1.7	Four common types of 2D lattice arrangement of columnar mesophases: hexagonal (Col _h), tetragonal (Col _{tet}), oblique (Col _{ob}) and rectangular (Col _r).	12
Figure 1.8	Schematic representations of (A) a columnar mesophase; (B) a column in an ordered (Col _o) mesophase and (C) a column in a disordered (Col _d) mesophase.	12

Figure 1.9	Molecular structures of (A) pentacene and (B) rubrene.	14
Figure 1.10	Schematic representations of two common organic field-effect transistor configurations: (A) top contact and (B) bottom contact.	22
Figure 1.11	An oxadiazole-containing smectic liquid crystal as an electron-transport material.	22
Figure 1.12	Thiophene-containing smectic liquid crystals as hole-transport materials.	23
Figure 2.1	Absorption spectra of PDI1 (top) and PDI2 (bottom) in chloroform solution (solid line) and in thin film prepared by drop-casting (dashed line).	44
Figure 2.2	Cyclic voltammograms of PDI1 (left) and PDI2 (right) in 0.1 M Bu ₄ NPF ₆ dichloromethane solution with Fc ⁺ /Fc as internal standard (reversible waves between 0.5 and 0 V), scan rate = 50 mV/s.	45
Figure 2.3	DSC (second heating-cooling cycle) of PDI2 .	48
Figure 2.4	Optical textures of PDI1 (top, magnification 20 ×) and PDI2 (bottom, magnification 50 ×) between two crossed polarizers.	49
Figure 2.5	XRD of PDI1 (top) and PDI2 (bottom) at room temperature after cooling from the isotropic liquid.	50
Figure 2.6	Double logarithmic plot of the current density (<i>J</i>) vs. applied voltage (<i>V</i>) for PDI2 in the device: (+)ITO/ PDI2 (5 μm)/Ag(-).	53

Figure 2.7	(left) Double logarithmic plot of the current density (J) vs. applied voltage (V) measured in two different samples of PDI1 . The thickness of both samples (1) and (2) was 5 μm ; full line and dashed line for sample (1) show linear and nearly quadratic power laws of the current density as a function of applied voltage respectively. (right) Photograph (a) of sample (1) and (b) of sample (2) obtained by polarized microscopy.	53
Figure 3.1	Coronene monoimide measured by PR-TRMC technique.	66
Figure 3.2	Isomeric ratio of coronene diimide based on 500 MHz ^1H NMR.	70
Figure 3.3	Absorption and emission spectra of compound 6d in dichloromethane.	73
Figure 3.4	Cyclic voltammogram of compound 6a in 0.1 M Bu_4NPF_6 dichloromethane solution with Fc^+/Fc (0.5 - 0 V) as internal standard, scan rate = 50 mV/s.	75
Figure 3.5	Absorption of compound 6b as a function of the concentration in MCH (concentration range from 2.29×10^{-7} M to 3.57×10^{-5} M).	80
Figure 3.6	Absorption spectrum of a thin film of compound 6b prepared by drop casting of dichloromethane solution on a quartz slide.	81
Figure 3.7	Fraction of aggregated molecules as a function of the concentration of coronene diimides in MCH (absorption at 420 nm is used for calculation).	81
Figure 3.8	DSC (second heating-cooling cycle) of compound 6c .	83
Figure 3.9	Optical textures of coronene diimides 6a - d between crossed polarizers (magnification 20 \times).	83
Figure 3.10	XRD of compounds 6a - d at room temperature after cooling from the isotropic phase.	87

Figure 3.11	Double logarithmic plot of the current density (J) vs applied voltage (V) for compound 6b in the device: (+)ITO/ 6b (5 μm)/Ag(-).	89
Figure 4.1	Triphenylene with perfluoroalkyl groups that can realize homeotropic alignment on various substrates.	107
Figure 4.2	Organic semiconducting materials with perfluoroalkyl groups showing improved electron-transport properties.	107
Figure 4.3	Absorption and emission spectra of CDI-F7 in dichloromethane (excitation wavelength is 400 nm).	113
Figure 4.4	Cyclic voltammograms of CDI-C8 (top) and CDI-F7 (bottom) in 0.1 M Bu_4NPF_6 dichloromethane solution with Fc^+/Fc (0.5 – 0 V) as internal standard, scan rate = 50 mV/s.	114
Figure 4.5	DSC traces (second heating-cooling cycle) of CDI-C8 (top) and CDI-F7 (bottom).	117
Figure 4.6	Optical textures of CDI-C8 (top) and CDI-F7 (bottom) between crossed polarizers (magnification 20 \times) at room temperature after cooling from the isotropic liquid.	118
Figure 4.7	XRD of (a) CDI-C8 at room temperature after cooling from the isotropic phase, (b) CDI-F7 at room temperature after cooling from the isotropic phase, (c) CDI-F7 at 100 $^\circ\text{C}$ during the second cooling process.	120
Figure 4.8	Double logarithmic plot of the current density (J) vs. applied voltage (V) for CDI-C8 (top) and CDI-F7 (bottom) in the device geometry: (+)ITO/ CDI (5 μm)/Ag(-).	122
Figure 5.1	Molecular structures of green chromophore 5PDI and the D-A biomimetic systems 5PDI-NI and 5PDI-PDI .	134
Figure 5.2	Cofacial and linear dimers of 5PDI .	135
Figure 5.3	5PDI-TAP used for charge-transfer studies in aggregates.	136

Figure 5.4	Artificial photosynthetic array combining energy and charge transfer.	137
Figure 5.5	Absorption spectra of compound 1 - 3 in toluene (concentration 10^{-6} to 10^{-5} M).	141
Figure 5.6	Normalized absorption spectra of compound 4 (top) and compound 1 (bottom) in toluene.	142
Figure 5.7	Normalized absorption spectra of compound 2 (top) and compound 5 (bottom) in toluene.	143
Figure 5.8	Transient absorption spectra of compound 2 in toluene after excitation at 400 nm.	145
Figure 5.9	Decay of the excited states of compound 2 at 657 nm (top) and 715 nm (bottom) in toluene.	146
Figure 5.10	Cyclic voltammogram of compound 2 with Fc^+/Fc as internal standard, scan rate = 25 mV/s.	149

LIST OF SCHEMES

Scheme 2.1	Synthesis of PDI1.	42
Scheme 2.2	Synthesis of PDI2.	42
Scheme 3.1	Synthesis of coronene diimides 6a - d .	68
Scheme 3.2	Reaction of dibromo-perylene diimide with acetylene in the presence of a secondary amine.	71
Scheme 4.1	Attempted synthesis of coronene diimide with compound 3 bearing an ether-linker.	109
Scheme 4.2	Synthesis of compound 10 with an ester linker.	109
Scheme 4.3	Synthesis of coronene diimides CDI-C8 and CDI-F7 .	110
Scheme 5.1	Synthesis of donor-substituted perylene diimides 1 - 5 .	139

LIST OF SYMBOLS AND ABBREVIATIONS

CV	Cyclic voltammetry
DSC	Differential scanning calorimetry
POM	Polarized optical microscopy
XRD	X-ray diffraction
DBU	1,8-diazabicyclo[5.4.0]undec-7-ene
DCM	Dichloromethane
DMF	Dimethylformamide
TBAF	Tetrabutylammonium fluoride
THF	Tetrahydrofuran
MCH	Methyl cyclohexane
PDI	Perylene diimide
CDI	Coronene diimide
TLC	Thin-layer chromatography
IP	Ionization potential
EA	Electron affinity
PES	Photoelectron spectroscopy
IPES	Inverse photoelectron spectroscopy
NMP	N-methyl pyrrolidinone
HOMO	Highest occupied molecular orbital
LUMO	Lowest unoccupied molecular orbital
TOF	Time of flight

PR-TRMC	Pulse-radiolysis time-resolved microwave conductivity
SCLC	Space-charge limited current
OLED	Organic light-emitting diode
FET	Field-effect transistor
ITO	Indium tin oxide
μ_0	Charge-carrier mobility at zero electric field
ρ	Charge density
μ	Charge-carrier mobility
σ	Conductivity
J	Current density
V	Applied voltage
E	Applied electric field
E_g	Energy gap
E_{op}	Optical energy gap
E_b	Exciton binding energy
ϕ_f	Fluorescence quantum yield
S_m	Smectic mesophase
Col	Columnar mesophase
Col _h	Hexagonal columnar mesophase
Col _r	Rectangular columnar mesophase
Col _{oh}	Ordered hexagonal columnar mesophase
Col _{or}	Ordered rectangular columnar mesophase

SUMMARY

Perylene-based materials, including charge-transport discotic liquid crystals and charge-transfer long-wavelength absorbing chromophores, for potential organic electronic and optoelectronic applications, were designed, synthesized and characterized. Two types of discotic liquid crystals, perylene diimides and coronene diimides, can form columnar liquid crystalline phases over a wide temperature range; many of them can have room-temperature liquid crystalline phases after cooling from isotropic liquid. Their charge transport properties were studied by space-charge limited current method; high charge carrier mobilities, with the highest being up to $6.6 \text{ cm}^2/\text{Vs}$, were found in liquid crystalline phases of these materials under ambient conditions. Structural variables, including aromatic cores and side groups, were examined to get a certain degree of understanding of charge transport properties in these discotic liquid crystals. It was found that mesophase order can have an important effect on charge carrier mobilities. The discotic liquid crystals with high charge carrier mobilities are serious candidates for use in large-area low-cost applications such as solar cells. Long-wavelength, highly absorbing chromophores, featuring donor-substituted perylene diimides, were generated by a combination of charge-transfer process and conjugation extension. The charge-transfer chromophores are expected to lead to further investigation on their potentials as sensitizers in Grätzel solar cells.

CHAPTER 1

INTRODUCTION

1.1 Organic semiconductors

Organic semiconducting materials have emerged as promising candidates for use in electronic and optoelectronic devices.¹ Traditional electronic and optoelectronic devices are composed of inorganic semiconductors such as amorphous, polycrystalline or single crystalline silicon that are usually processed under high temperature and high vacuum conditions.² Compared to inorganic semiconductors, organic semiconducting materials are characterized by immense structural flexibility such that their optical and electrical properties can be easily tuned; they can also have excellent solubility in various organic solvents, which can potentially enable low-cost solution processing techniques such as spin-coating to be used at or close to room temperature.³ The low temperature processing techniques also allow device fabrication onto transparent plastic substrates. Thus, organic semiconducting materials are potentially suitable for low-cost, flexible and lightweight electronic and optoelectronic devices.³

The most successful application of organic semiconductors is in the field of xerography, which accounts for several billions of dollars of business around the world. The semiconducting materials used in xerography are the photoconductors that are responsible for photogeneration of charge carriers and charge transport.^{1g} Today, organic semiconductors are studied for many other electronic and optoelectronic applications. In electronic and optoelectronic devices, one or a combination of several properties of organic semiconducting materials can be utilized. For example, tris(8-hydroxyquinoline)

aluminum (Alq_3) as both a charge-transport and a light-emitting material has been used in Tang's organic light-emitting diode (OLED) (Figure 1.1).^{1a} Copper phthalocyanine (CuPc) as both a light-harvesting and a charge-transport material has been used in photovoltaic cells (Figure 1.2).^{1c} 3',4'-Dibutyl-5,5''-bis(dicyanomethylene)-5,5''-dihydro-2,2':5',2''-terthiophene (DCMT) has been used as a charge-transport material in field-effect transistors (FET) (Figure 1.3).^{1d} In virtually all of the electronic and optoelectronic devices, charge-transport process is one of the key processes. Thus, charge-transport materials are important components in electronic and optoelectronic devices.

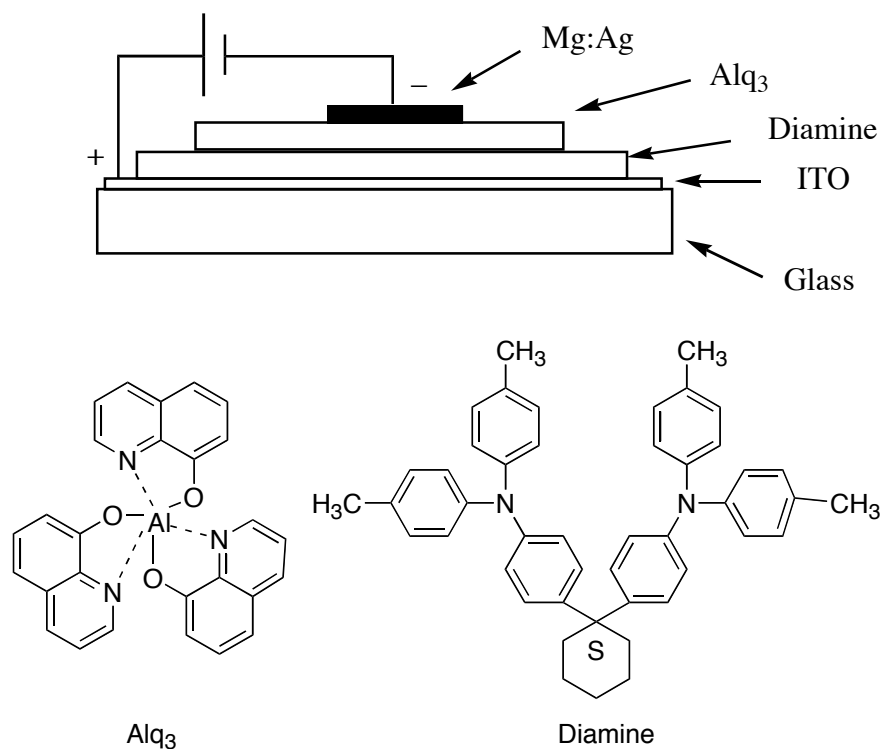


Figure 1.1 Tang's OLED with a diamine as the hole-transport material and Alq_3 as both the electron-transport and the light-emitting material. Holes injected from the indium-tin-oxide (ITO) anode and electrons injected from the Mg:Ag cathode are transported by the diamine and the Alq_3 layer respectively to the interface of the hole-transport and electron-transport layer where the electrons and holes can recombine into excitons (bound electron and hole pairs) and subsequent radiative decay of the excitons leads to emission of light. (From ref. 1a).

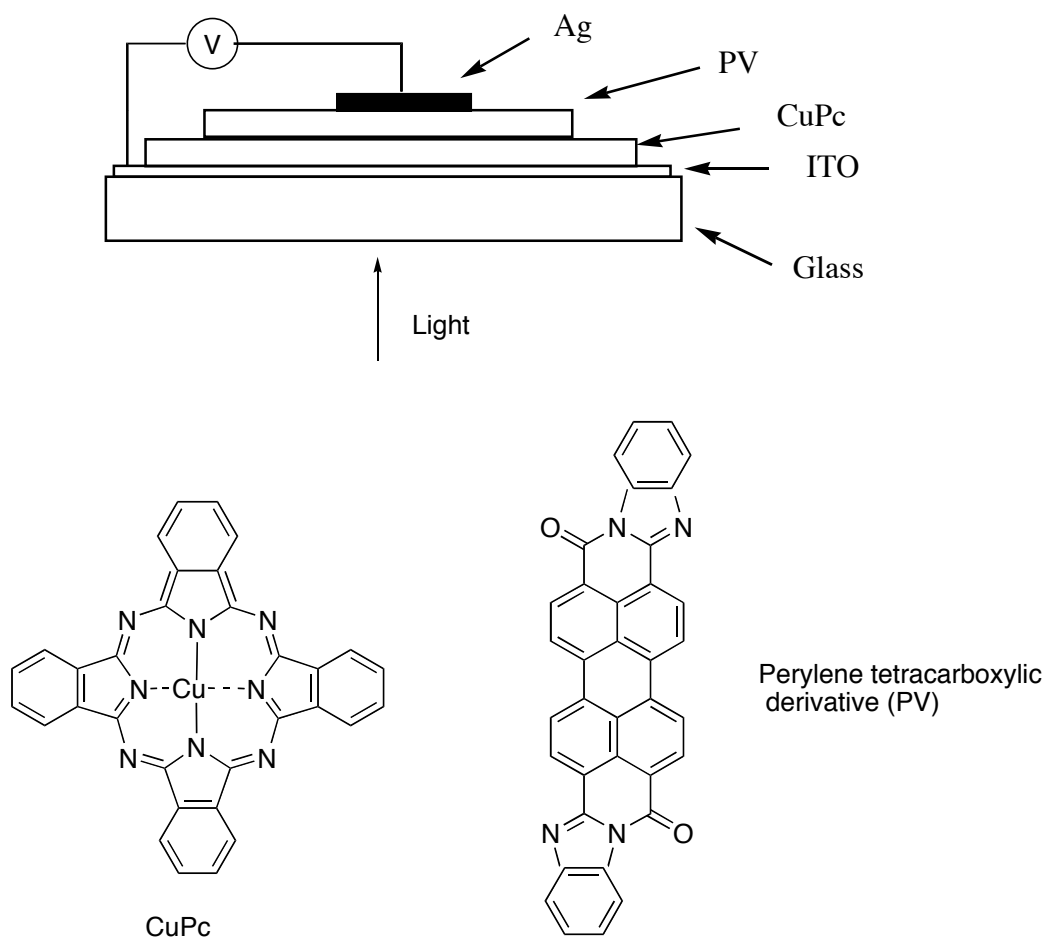


Figure 1.2 Tang's photovoltaic cell with CuPc and PV as both the light-harvesting and the charge-transport materials. Light absorption by these two materials leads to the formation of excitons, which can dissociate into electrons and holes at the interface of the CuPc and PV layers. The electrons and holes can then be transported in the opposite directions to generate current. (From ref. 1c)

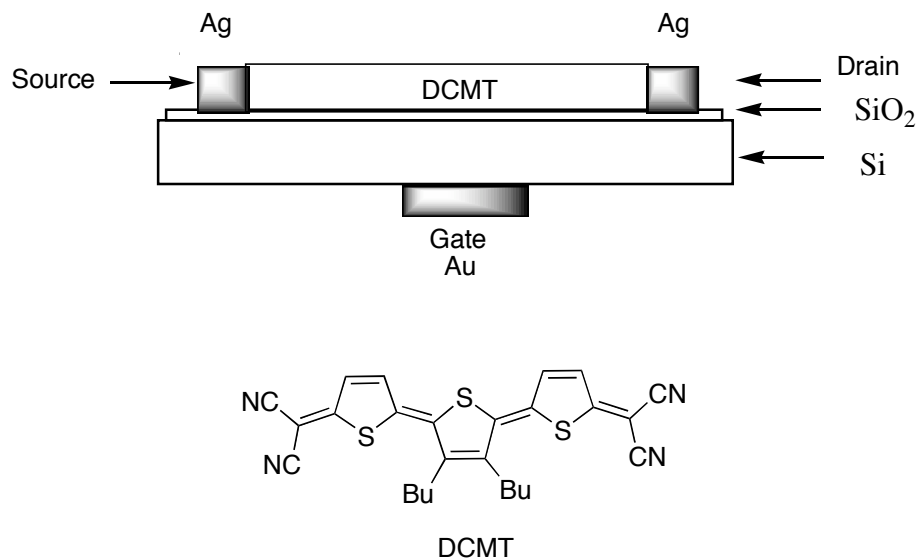


Figure 1.3 Field-effect transistor using DCMT as the charge-transport material. Application of gate voltage induces formation of charges that can be transported between the source and drain electrodes, leading to a source-drain current, which is a function of the gate voltage. (From ref. 1d).

Organic charge-transport materials can be classified into hole-transport materials,⁴ electron-transport materials⁵ or bipolar charge-transport materials.⁶ One of the major parameters that characterize charge-transport materials is charge carrier mobility μ (cm^2/Vs), which can be expressed as

$$\mu = \frac{v_d}{E} \quad (1.1)$$

where v_d is the drift velocity (cm/s) of charge carriers and E (V/cm) is the electric field strength.

Another parameter that is commonly used is conductivity σ (S/cm). The relationship between charge carrier mobility and conductivity is given by

$$\sigma = \rho \mu = n e \mu \quad (1.2)$$

in which ρ is the charge density, n is the charge carrier density and e is the elementary charge.

For organic semiconductors with high purity, the amount of free charge carriers present in the materials is usually negligible and the materials typically show little conductivity. The concentration of free charge carriers in organic materials can be significantly increased by doping with oxidizing/reducing agents or electrochemical methods,⁷ photogeneration,⁸ charge injection from contacting electrodes⁹ and ionization with high energy electrons,¹⁰ and consequently the conductivities of the materials can be dramatically increased. Generally, metals show high conductivities with $\sigma \geq 10^3$ S/cm and insulators have extremely low conductivities with $\sigma \leq 10^{-12}$ S/cm. Semiconductors have conductivities between 10^{-12} and 10^3 S/cm.^{11a} For example, standard grade poly(3,4-ethylenedioxythiophene) : poly(styrenesulfonate) (PEDOT : PSS) can have conductivity of 1 S/cm and its conductivity can be improved to 100 S/cm with sorbitol.^{7c} According to equation 1.2, conductivity is related to charge carrier mobility and charge density. Although typically charge carrier mobilities (between 10 and 100 cm²/Vs) in metals are lower than that in traditional inorganic semiconductors (monocrystalline Si has electron mobilities up to 1500 cm²/Vs), the higher conductivity in metals is mainly attributed to the much higher charge (i.e. free electron) density.^{11b}

1.2 Charge transport in organic semiconductors

Charge-transport process in conventional inorganic semiconductors is usually described using a band model, in which the highest energy occupied band is called the valence band (VB) and the lowest energy unoccupied band is called the conduction band (CB).¹² Charge carriers can be produced by removing electrons from the valence band, by

adding electrons into the conduction band, or by promoting electrons from the valence band to the conduction band to generate excitons that may then dissociate into free charge carriers under an applied electric field or by contacting with an electrode. Free charge carriers can then move in the highly delocalized states within the bands (Figure 1.4A).¹² The charge-transport process in the band model is mainly limited by phonons (lattice vibrations), which scatter the charge carriers. As the temperature T increases, the frequency of the lattice vibrations and the scattering of charge carriers by phonons are increased and thus the charge carrier mobility is decreased as expressed by

$$\mu \propto T^{-n} \quad (1.3)$$

in which n is a number larger than unity.¹³

Generally the band model is no longer applicable for materials with low charge carrier mobilities (usually $\mu \leq 1 \text{ cm}^2/\text{Vs}$), including amorphous silicon and organic semiconductors.¹⁴ For disordered organic materials, intermolecular interactions are weak and are classified as van der Waals forces. Such weak intermolecular interactions lead to the formation of discrete energy levels (Figure 1.4B) instead of energy bands. Thus, charge-transport process is considered as a hopping process of charge carriers between localized states (Figure 1.4C).¹⁴ In such a hopping regime in low mobility materials, the charge carriers can reside on a molecule for a sufficiently long time such that localization of the charge carriers is accompanied by geometry relaxation of the molecules.¹⁵ In contrast to the phonon-limited charge-transport process in the band model, the charge carrier hopping process is a phonon assisted process and thus the charge carrier mobilities are usually increased with increasing temperatures.¹⁴ However, it has been demonstrated that generally the charge carrier mobilities are almost independent of temperatures within the same liquid crystalline phases of columnar discotic liquid crystals (*vide infra*).¹⁶

Similar temperature independent charge carrier mobilities have also been observed in polycrystalline thin films of pentacene.¹⁷ In these cases, it becomes controversial whether the hopping mechanism should be excluded and it remains unclear what other factors should be taken into account to explain such independency of charge carrier mobilities on temperatures.¹⁴

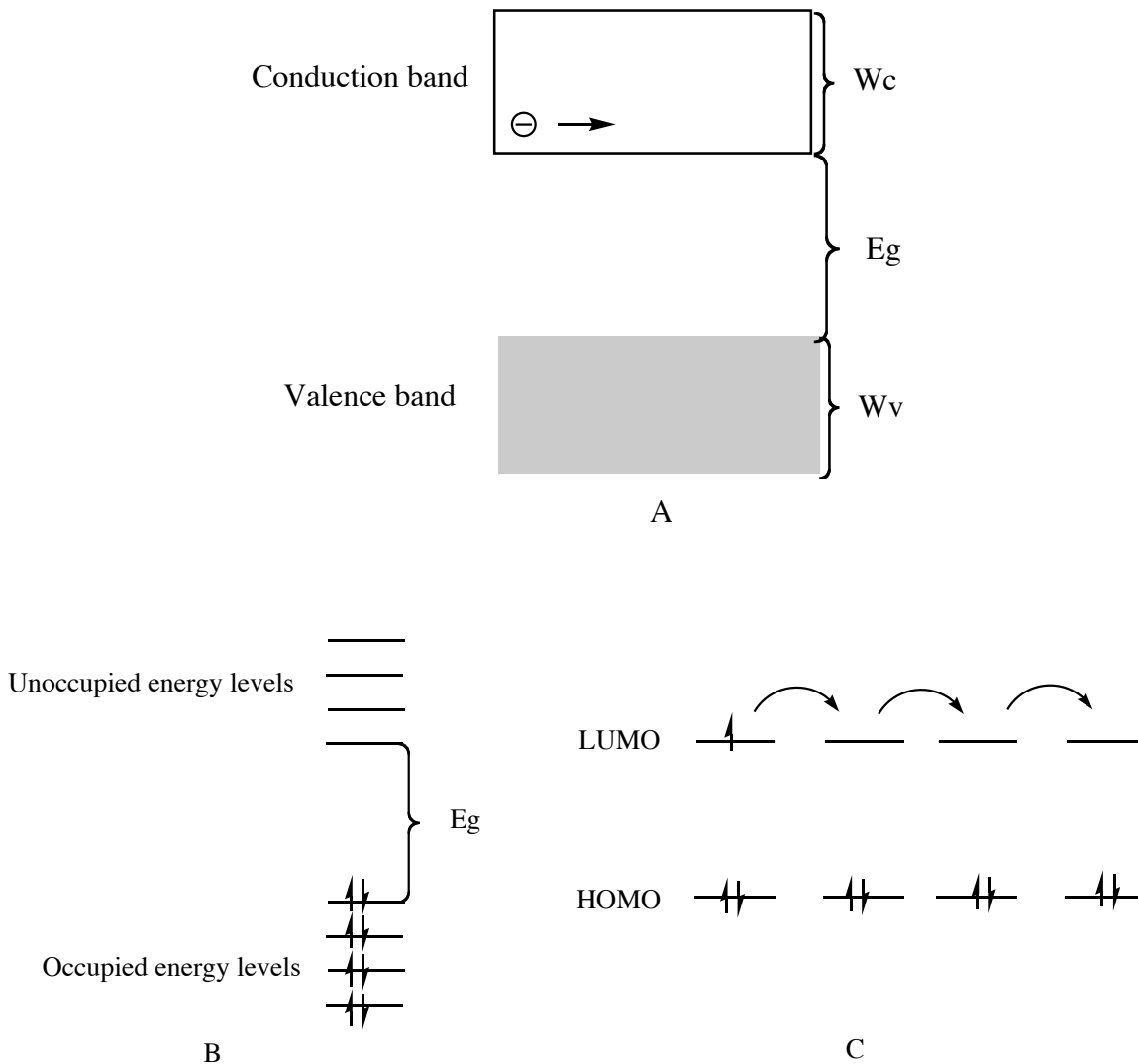


Figure 1.4 Schematic illustration of (A) electron transport in the conduction band of inorganic semiconductors (W_c is the bandwidth of the conduction band and W_v is the bandwidth of the valence band; E_g is the energy gap between the conduction band and the valence band); (B) discrete energy levels in organic semiconductors and (C) electron hopping through LUMO levels of organic molecules (E_g is the energy gap between the HOMO and LUMO levels).

In addition, the hopping process of charge carriers in organic semiconductors is often complicated by the presence of traps. Traps are usually localized at lattice defects (void positions which should be otherwise occupied by molecules as in single crystalline materials), impurities and domain boundaries (often occur in polycrystalline materials composed of small crystalline grains that can have gaps between them) in the materials.^{14,17} Under such conditions, other models such as multiple trapping and release (MTR) model have been developed to take into account the effect of traps.¹⁸

Insightful understanding of the charge-transport process in organic semiconductors at the molecular level based on quantum calculations has also been developed.¹⁹ In such quantum calculations, it is also assumed that the charge-transport process is a phonon-assisted hopping process between molecules. Furthermore, the charge-transport process can be considered as a self-exchange process between charged molecules and neighboring neutral molecules to the first approximation.¹⁹ The charge-transfer rate of such self-exchange process can be described by semiclassical Marcus theory via

$$k_{et} = \left(\frac{4\pi^2}{h} \right) t^2 (4\pi\lambda k_B T)^{-0.5} \exp\left(\frac{-\lambda}{4k_B T} \right) \quad (1.4)$$

where k_{et} is the charge-transfer rate, h is Planck's constant, t is the intermolecular transfer integral, λ is the reorganization energy, k_B is Boltzmann's constant and T is the temperature. This equation clearly indicates that the charge transfer rate is related to both the reorganization energy and the intermolecular transfer integral. The reorganization energy has two components: 1) the inner reorganization energy that reflects the energy changes of the vibration processes ongoing from the charged molecules to the neutral molecules and vice versa (Figure 1.5) and 2) the reorganization energy of the surrounding

dielectric media due to the polarization changes during the charge-transfer process.^{19,20} The intermolecular transfer integral is determined by the strength of the electronic coupling between two molecules. In order to have a large charge-transfer rate between two molecules and thus a large charge carrier mobility of the material, the reorganization energy should be small and the intermolecular transfer integral should be large. To have a small reorganization energy, the π -electrons of the aromatic molecules should be highly delocalized. To have a large intermolecular transfer integral, the molecules should have a large right orbital overlap (rotational disorder can have a significant effect on the intermolecular transfer integral) and a small separation distance.

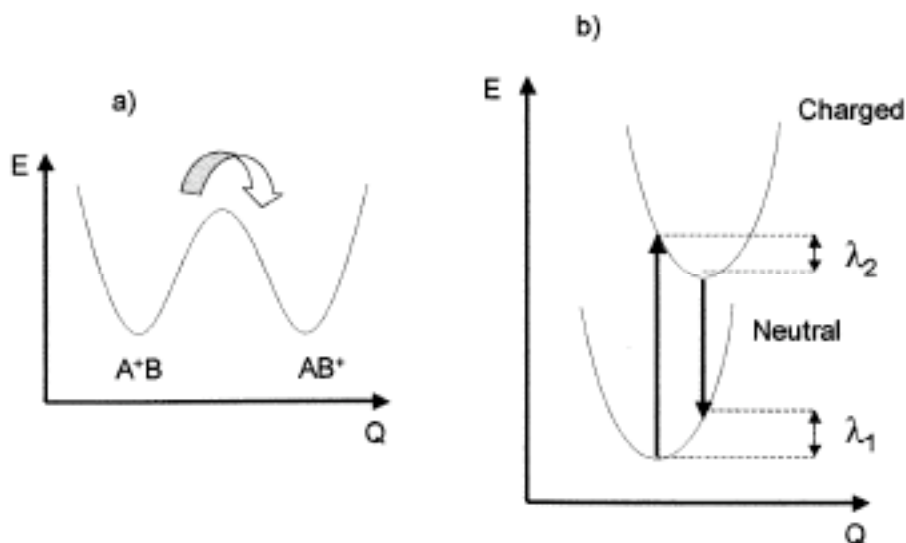


Figure 1.5 (a) illustrates a hole transfer from a charged molecule A^+ to a neutral molecule B via a transition state where the two molecules adopt the same geometry. (b) illustrates the energy potential change ongoing from neutral to charged molecules. The inner reorganization energy is the sum of λ_1 and λ_2 . (Figures taken from ref. 19)

1.3 Liquid crystals

Liquid crystals are a state of matter that lie between crystals and isotropic liquids.²¹ Liquid crystals are generally characterized by a relatively long-range orientational order with the mesogens aligned along the director, but a positional order in three dimensions is lacking.

According to the conditions under which liquid crystals can be formed, liquid crystals can be identified as either lyotropic or thermotropic.²¹ In lyotropic liquid crystals, formation of liquid crystalline phases and phase properties are dependent on the solvent used and the concentration of the solution. On the other hand, in thermotropic liquid crystals, the phase transitions and phase properties are dependent on the temperature. The structure of lyotropic liquid crystals is usually characterized by amphiphilic components: polar part and non-polar part.²² A familiar example of lyotropic liquid crystals is surfactants which usually have a polar head group (in ionic form) and a non-polar alkyl group. Thermotropic liquid crystals usually have a rigid motif and a flexible tail or tails. Most of the liquid crystals that have been studied as charge transport materials have such structural features.

According to the shape of the mesogenic units, thermotropic liquid crystals can be divided into two types: calamitic (rod-like) and discotic (disc-like).²¹

Discotic liquid crystals, usually composed of a rigid (aromatic) core substituted with flexible side groups, can form either nematic (N_D) or columnar (Col) mesophases.²¹ Most discotic liquid crystals form columnar phases and there is only a scarce amount of discotic liquid crystals that form nematic phases.²³ Nematic phases only have an orientational order with the normal of the discs aligned along the director (Figure 1.6); columnar phases have higher orders with the discs organized into columns, which then

arrange themselves into 2D lattices.²¹ Common 2D lattices include, but are not limited to, hexagonal, tetragonal, oblique and rectangular *etc* (Figure 1.7).²⁴ Columnar mesophases can be either disordered (Col_d) or ordered (Col_o), according to the regularity of the discs within the same column.²⁴ When the separation between two neighboring discs is in a random fashion within the same column, the corresponding columnar mesophase is a disordered one; on the other hand, a relatively long-range order is expected when the intracolumnar distance is constant, which defines the columnar mesophase as an ordered columnar mesophase (Figure 1.8).

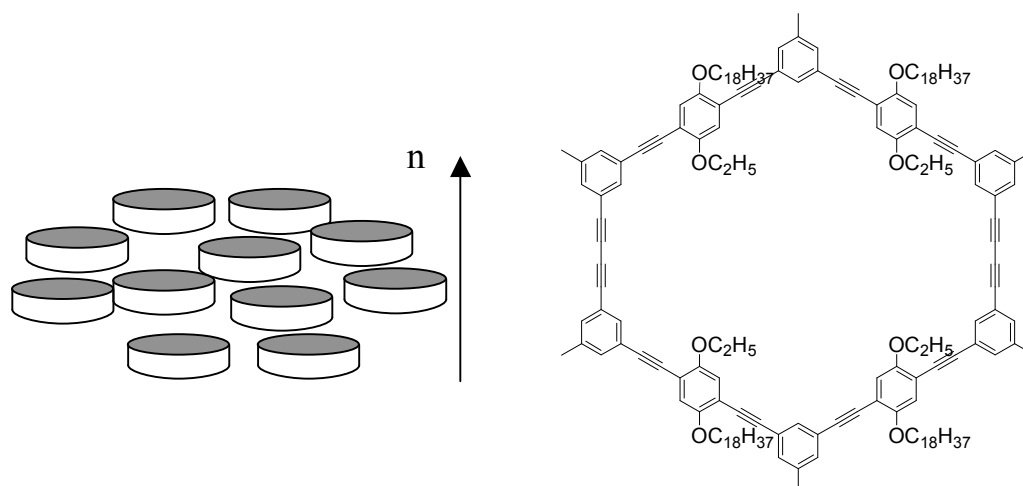


Figure 1.6 Schematic representations of a nematic discotic mesophase and a macrocyclic molecule that forms a nematic phase.

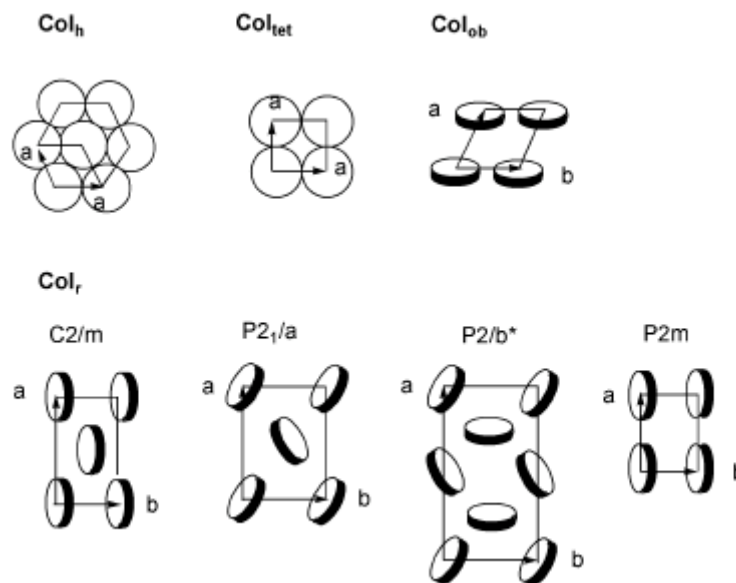


Figure 1.7 Four common types of 2D lattice arrangement of columnar mesophases: hexagonal (Col_h), tetragonal (Col_{tet}), oblique (Col_{ob}) and rectangular (Col_r) (Schemes taken from ref. 24).

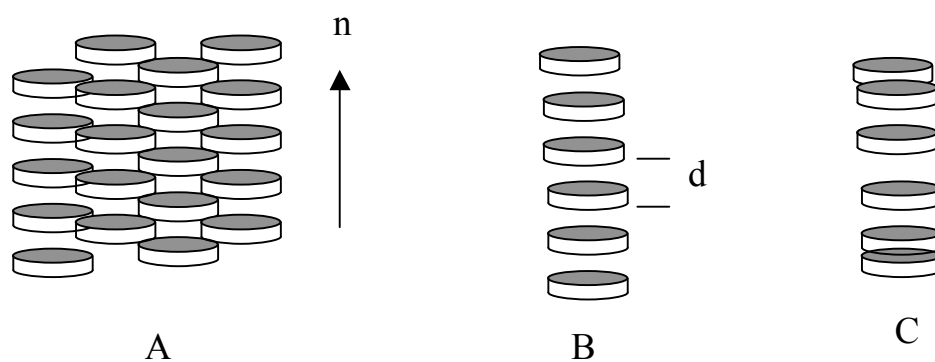


Figure 1.8 Schematic representations of (A) a columnar mesophase, (B) a column in an ordered (Col_o) mesophase and (C) a column in a disordered (Col_d) mesophase.

1.4 Rationale for using discotic liquid crystals as charge-transport materials

Organic semiconducting materials that are being studied for use in organic electronics and optoelectronics can be largely classified into three categories: amorphous, liquid crystalline and crystalline materials.

Amorphous materials are materials that do not have any molecular order.²⁵ In amorphous material, the molecules do not have regular packing and have a small molecular orbital overlap between neighboring molecules. Molecular amorphous materials can be processed by several processing techniques including thermal evaporation and spin-coating. However, amorphous materials usually exhibit low charge carrier mobilities as a result of the high disorder of the molecular arrangements in the materials. For example, *N,N'*-diphenyl-*N,N'*-bis(3-methylphenyl)-[1,1'-biphenyl]-4,4'-diamine (TPD)²⁶ and Alq₃²⁷ are typical amorphous hole-transport and electron-transport materials respectively with charge carrier mobility generally below 10⁻³ cm²/Vs.

Crystalline materials, polycrystalline materials or single crystals, have been extensively studied as charge-transport materials.²⁸ Single crystals possess three-dimensional periodicity of the molecules and have low concentrations of impurities, thus single crystals usually have high charge carrier mobilities. As the benchmark material, pentacene has been extensively studied over several decades. To date, the highest hole mobility found in single crystalline pentacene (Figure 1.9A) was 35 cm²/Vs at room temperature and 58 cm²/Vs at 225 K.²⁹ In another molecular crystal rubrene (Figure 1.9B), hole mobilities in field-effect transistors were found to be as high as 20 cm²/Vs.³⁰ Other interesting molecular crystals include, but are not limited to, tetracyanoquinodimethane (TCNQ),³¹ fullerene,³² tetracene,³³ tetrathiafulvalene (TTF),³⁴ dithiophene-tetrathiafulvalene (DT-TTF),³⁵ thiophene derivatives,³⁶ perylene diimides³⁷

and various combinations of different moieties based upon the specific properties that the researchers want to incorporate into the materials.³⁸ Polycrystalline materials can be deposited by vacuum evaporation or solution-based methods, but the observed mobilities are generally lower than in single crystals.³⁹ Single crystals that have a relatively large size can be incorporated into devices directly; however, the fact that they can not be readily obtained and can not be processed on a large scale would potentially render their practical applications limited.

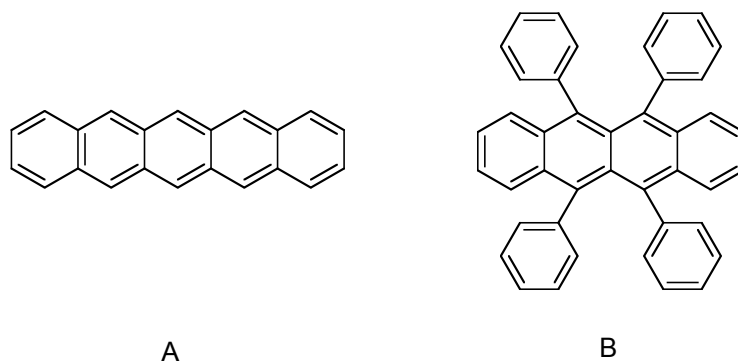


Figure 1.9 Molecular structures of (A) pentacene and (B) rubrene.

Liquid crystals, especially discotic liquid crystals, have been demonstrated to have relatively high charge carrier mobilities due to their high degree of order.⁴⁰ Discotic liquid crystals can self-assemble into one-dimensional columns through π orbital interaction and phase segregation between the usually flat rigid aromatic cores and the flexible side chains. The stacks of the aromatic cores provide efficient channels for the charge carriers to transport along the columns, but the intercolumnar charge transport process is negligible due to the insulating effect of the side chains surrounding the

columns. Moreover, discotic liquid crystals have self-healing capability and mesophase defects can be easily removed. In addition, potential orientation of discotic liquid crystals can be controlled and the materials can be processed from solutions. Therefore, discotic liquid crystals are promising candidates for large area and low cost applications.

1.5 Charge carrier mobility characterization methods

Tremendous efforts have been spent on the charge carrier mobility characterizations of discotic liquid crystals.⁴⁰ Commonly used charge carrier mobility measurement methods include transient photoconductivity technique, also known as time-of-flight (TOF), pulse-radiolysis time-resolved microwave conductivity (PR-TRMC) technique, space-charge limited current (SCLC) method and field-effect transistor (FET).

1.5.1 TOF technique

In the seminal work by Haarer, D. *et al* on discotic liquid crystals as charge-transport materials, TOF method was introduced into the field of discotic liquid crystals.^{8,41} In a TOF experiment, the liquid crystalline materials are filled in a chamber composed of two electrodes, one of which is transparent (usually ITO). Irradiation of a laser pulse from the ITO side on the liquid crystalline materials that can have strong absorption of the laser light can lead to the creation of bound excitons in the vicinity of the electrode, and free charge carriers can then be generated by dissociation of the excitons. The oppositely charged carriers are captured by the electrode from which the material under study is irradiated, by controlling the polarity of the applied electric field, and the free charge carriers of interest then drift under the applied electric field toward

the opposite electrode to generate a transient current. The transient time τ is determined by the distance d over which the charge carriers travel and the velocity (μE) of the charge carriers:

$$\tau = \frac{d}{\mu E} \quad (1.5)$$

the charge carrier mobility is then derived via

$$\mu = \frac{d}{\tau E} = \frac{d^2}{\tau V} \quad (1.6)$$

In TOF method, it is required that the light-absorbing length is much smaller than the thickness of the film, thus relatively thick films are used. Also it is assumed that the electric field under which the charge carriers drift across the material is constant, thus the charge carrier density in the material should be low such that the charge carriers do not affect the electric field significantly. In addition, compared to the drift of charge carriers under the applied electric field, the diffusion of charge carriers is negligible due to the low charge carrier density required in the materials.

One of the advantages of using TOF is that the electron and hole mobility can be studied separately. However, the low density of charge carriers required by this method makes the derived charge carrier mobility highly sensitive to the possible defects and traps present in the liquid crystalline phases. Thus far, TOF method has been used mostly for the measurement of triphenylene liquid crystals, simply due to the fact that many triphenylene liquid crystals can spontaneously form homeotropic alignment between two electrodes.^{8,41,42} Applications of TOF to other columnar discotic liquid crystals are still limited due to the difficulty in homeotropic alignment of columnar discotic liquid crystals.⁴³

1.5.2 PR-TRMC technique

PR-TRMC technique for studying charge carrier mobility of discotic liquid crystals developed by Warman and coworkers has been extensively applied to various liquid crystalline materials.¹⁰ In a PR-TRMC experiment, the pristine material is compressed in a chamber and exposed to a nanosecond pulse of high-energy electrons (3 MeV) from a van der Graaff accelerator to generate uniformly distributed charge carriers with known concentrations in the sample. Mobile charge carriers generated by the high energy electrons lead to an increase in the conductivity of the sample which magnifies itself by a decrease in the power of the microwave over time. In the conductivity transient, the magnitude at the end of the pulse is proportional to the concentration of charge carriers generated and the charge carrier mobility. Subsequent charge carrier recombination/trapping results in the decay of the conductivity transient. The sum of the charge carrier mobilities of both holes and electrons can be estimated from

$$\mu_{total} = \frac{E_p}{W_{eop}} \left(\frac{\Delta\sigma}{D} \right)_{eop} \quad (1.7)$$

where E_p is the average pair-formation energy, $\Delta\sigma$ is the change in the conductivity of the sample, D is the energy absorbed by the sample and W_{eop} is the fraction of initially formed charge carrier pairs that survive the charge recombination/trapping process during the transient.

PR-TRMC technique was established as a valuable method of studying charge carrier mobility and charge carrier dynamics by comparison studies of the helical hexakis-hexylthiotriphenylene (HHTT) liquid crystal using both TOF and PR-TRMC techniques.⁴⁴ The comparison study on the homeotropic triphenylene liquid crystal revealed comparable charge carrier mobilities in both the liquid crystalline phases and the

isotropic phase. Also, charge carrier mobilities in the polycrystalline phase of HHTT were determined, because PR-TRMC technique is not sensitive to defects or domain boundaries due to the nanosecond response time for the detection. Within such short time, the charge carrier mobilities can be considered as the effective mobilities within well-organized domains.

It is claimed that PR-TRMC technique is not sensitive to the morphology of the samples and thus a variety of materials can be potentially studied and compared. Also it is not sensitive to the defects and traps due to the low electric field strength (< 100 V/cm) and the ultrahigh frequency (ca. 30 GHz), therefore the random diffusion of the charge carriers is only slightly perturbed and the derived charge carrier mobility represents zero-field, trap-free values of the materials.^{40c-d} However, the huge van der Graaff accelerator is not readily available, making PR-TRMC technique mainly limited to the groups at the Delft University of Technology in the Netherlands. Also PR-TRMC technique is an “electrodeless” technique and only determines the sum of the charge carrier mobilities rather than that for individual charge carriers.

1.5.3 SCLC technique

Charge injection from metal contacts into an insulator can be treated by SCLC theory⁴⁶ and charge carrier mobilities can be derived from the current-voltage characteristics of the capacitor made of the insulator and the planar contacting electrodes.⁴⁷

In an SCLC experiment, the material under study is sandwiched between two planar electrodes, and the charge carriers are injected from the electrodes and drift across the material under the applied electric field. When the applied voltage is low, the

concentration of charge carriers injected into the material is usually low and does not significantly affect the electric field that is assumed to be constant across the sample as is determined by the applied voltage V and the thickness of the film d via

$$E = \frac{V}{d} \quad (1.8)$$

at a given applied voltage. Under these conditions, the current density J is expressed by Ohm's law

$$J = \sigma E = n e \mu E = \rho \mu E \quad (1.9)$$

where σ is the conductivity, E is the applied electric field strength, n is the charge carrier density, e is the elementary charge, ρ is the charge density and μ is the charge carrier mobility.

When the applied voltage is further increased, the concentration of charge carriers injected into the sample from the electrodes is sufficiently high such that they can significantly modulate the electric field across the sample via Poisson's equation

$$\frac{dE}{dx} = \frac{\rho}{\epsilon_r \epsilon_0} \quad (1.10)$$

where ϵ_r is the dielectric constant of the material, ϵ_0 is the vacuum permittivity. Under such conditions, equation 1.8 can be written as

$$J = \mu \epsilon_r \epsilon_0 E \frac{dE}{dx} \quad (1.11)$$

and integration across the sample provides the Mott-Gurney law:

$$J = \frac{9}{8} \mu \epsilon_r \epsilon_0 \frac{V^2}{d^3} \quad (1.12)$$

which predicts the maximum current that can pass through a given material assuming trap free and ohmic contact. When a single set of traps is assumed to exist in the material, the Mott-Gurney law can be approximated to

$$J = \frac{9}{8} \mu_0 \epsilon_r \epsilon_0 \theta_0 \exp\left(0.891\gamma\sqrt{\frac{V}{d}}\right) \left(\frac{V^2}{d^3}\right) \quad (1.13)$$

assuming ohmic contact, where μ_0 is the charge carrier mobility at zero electric field, θ_0 is the fraction of free charge carriers and γ is a constant.^{45b} This modified Mott-Gurney law can then be rewritten into

$$J = \frac{9}{8} \mu_0 C \theta_0 \exp\left(0.891\gamma\sqrt{\frac{V}{d}}\right) \left(\frac{V^2}{d^2}\right) \quad (1.14)$$

where C is the capacitance per unit area of the SCLC sample and is in the form of

$$C = \frac{\epsilon_r \epsilon_0}{d} \quad (1.15)$$

Data analysis is performed by fitting the J - V curves in the linear region (ohmic region) and the quadratic region (SCLC region), respectively. Generally for the discotic liquid crystals studied in this thesis, in the ohmic region, J is proportional to V^a , where a is slightly higher than unity; in the SCLC region, J is proportional to V^b , where b is slightly higher than 2. Also, values for μ_0 and γ can be obtained by fitting of the SCLC region of the J - V curves, and these values can then be used to calculate charge carrier mobilities at different electric field according to

$$\mu = \mu_0 \exp(\gamma\sqrt{E}) \quad (1.16)$$

which is an empirical equation generally applicable for organic semiconductors.⁴⁷

Charge injection from the electrodes into the material under study is an important feature of SCLC experiments and typically a relative large current can pass through the

material, which in many ways resembles the situations in actual devices. The drawback of SCLC technique is that the sign of the charge carriers can not be determined, although analysis of the interfacial energetics between the material and the electrodes can provide certain information on the ease with which holes or electrons can be injected from the Fermi level of the electrodes into the frontier energy levels of the material.

1.5.4 FET geometry

Figure 1.10 shows two common organic FET configurations: (A) top contact and (B) bottom contact.^{38a} In the top contact configuration, an organic semiconductor thin film is deposited first onto an insulator substrate and then contacting metal electrodes are deposited onto the top of the semiconductor layer. In the bottom contact configuration, metal electrodes are deposited first onto an insulator substrate, followed by the deposition of an organic semiconductor thin film.

Application of a gate voltage (V_G) can induce free charge carriers in the semiconductor layer and depending upon the sign of the gate voltage and the type of the semiconductor, the induced charge carriers in the semiconductor layer can be either electrons or holes. When a source-drain voltage (V_D) is applied, the induced charge carriers will flow between the source and drain electrodes to generate a source-drain current (I_D). When V_D is small, the current-voltage relation is expressed as

$$I_{D,lin} = \frac{W}{L} C_{ox} \mu \left[(V_G - V_T) - \frac{V_D}{2} \right] V_D \quad (1.17)$$

where W is the width of the source-drain channel, L is the length of the channel, C_{ox} is the capacitance of the insulator per unit area, μ is the effective charge carrier mobility and V_T

is the threshold voltage. Equation 1.17 describes the current-voltage behavior in the “linear régime”, where $(V_G - V_T) > V_D$.

The effective charge carrier mobility in the linear régime can be calculated from either of two derivatives — transconductance (g_m) and conductance (g_d):

$$g_m = \left. \frac{\partial I_D}{\partial V_G} \right|_{V_D} = \frac{W}{L} C_{ox} \mu V_D \quad (1.18)$$

$$g_d = \left. \frac{\partial I_D}{\partial V_D} \right|_{V_G} \approx \frac{W}{L} C_{ox} \mu (V_G - V_T) \quad (\text{when } (V_G - V_T) \gg V_D) \quad (1.19)$$

When the source-drain voltage is large ($V_D \geq V_G - V_T$), the source-drain current reaches the saturation régime and is given by

$$I_{D,sat} = \frac{W}{2L} C_{ox} \mu (V_G - V_T)^2 \quad (1.20)$$

The effective charge carrier mobility can also be derived in the saturation régime from the slope of the $(I_{D,sat})^{0.5}$ vs V_G plot.

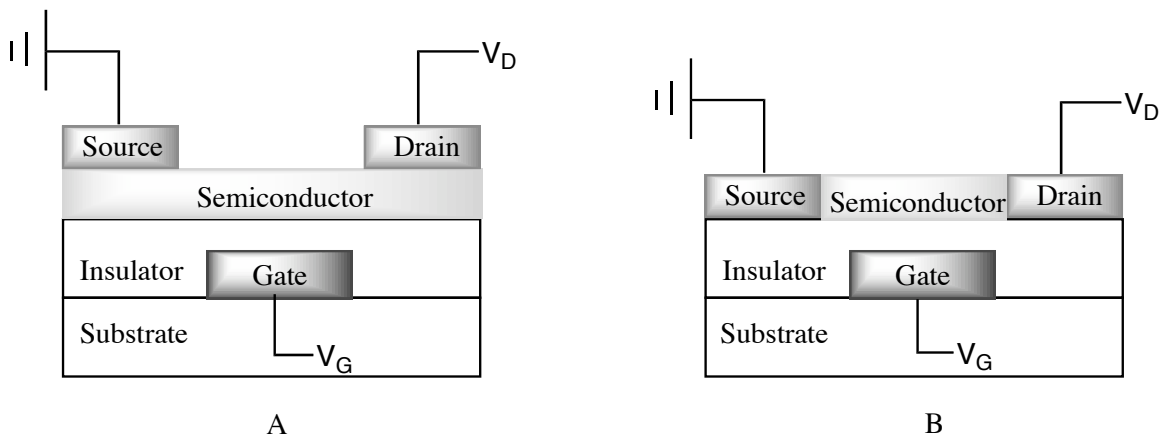


Figure 1.10. Schematic representations of two common organic field-effect transistor configurations: (A) top contact and (B) bottom contact.

1.6 Charge carrier mobilities of liquid crystals

Both calamitic and discotic liquid crystals have been examined as charge-transport materials. For example, calamitic oxadiazole-containing and thiophene-containing liquid crystals have been studied by the TOF technique. Electron mobilities were found on the order of 10^{-3} cm^2/Vs in the liquid crystalline phase at 343 K in an oxadiazole-containing liquid crystal (Figure 1.11)⁴⁸ Hole mobilities close to 0.1 cm^2/Vs were obtained in highly ordered liquid crystalline phases of thiophene-containing liquid crystals (Figure 1.12) at room temperature,⁴⁹ which is comparable to some high charge carrier mobility values found in discotic liquid crystals.

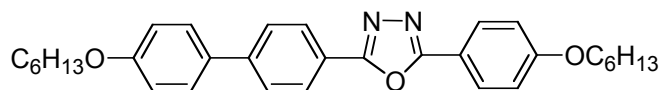


Figure 1.11 An oxadiazole-containing smectic liquid crystal as an electron-transport material.

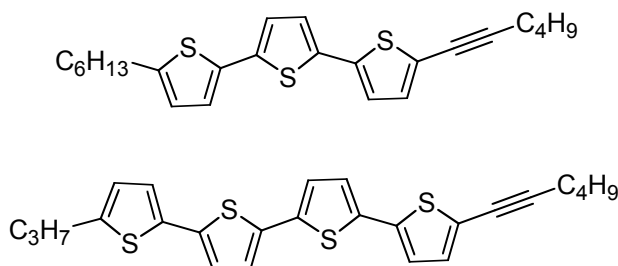


Figure 1.12 Thiophene-containing smectic liquid crystals as hole-transport materials.

Although the first discotic liquid crystals were discovered by Chandrasekhar in 1977,⁵⁰ their utility in organic electronics and optoelectronics as charge-transport materials came in 1994, when a helical triphenylene liquid crystal with a hole mobility of $0.1 \text{ cm}^2/\text{Vs}$ studied by the time-of-flight (TOF) technique was reported.⁸ Since then, discotic liquid crystals have been extensively studied as charge-transport materials. Discotic liquid crystals that have been studied as charge-transport materials include triphenylene, phthalocyanine (metallophthalocyanine), hexabenzocoronene, perylene diimide, coronene monoimide, hexaazatriphenylene, hexaazatrinaphthylene and their derivatives *etc.* The charge carrier mobilities in discotic liquid crystalline materials have been improved gradually and the highest charge carrier mobilities are close to that found in amorphous silicon. Several reviews have summarized the work on mobility measurements of discotic liquid crystals.⁴⁰ Here some discotic liquid crystals with relatively high charge carrier mobilities are compiled in Table 1.1.

Table 1.1 Some discotic liquid crystals and their charge carrier mobilities.

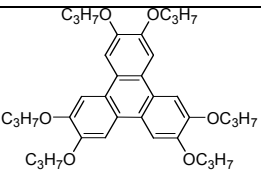
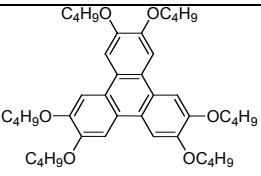
Molecular Structure	Mobility [cm^2/Vs] (phase, temperature [$^{\circ}\text{C}$])	Charge -carrier	Technique	Reference
	1.2×10^{-2} (130)	hole	TOF	51, 52
	1.2×10^{-2} (116, Col _{hp})	hole	TOF	52

Table 1.1 (CONT.)

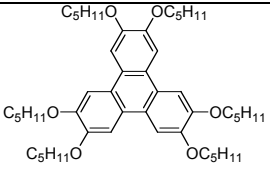
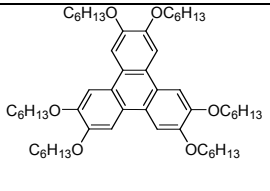
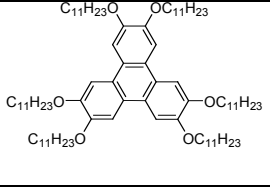
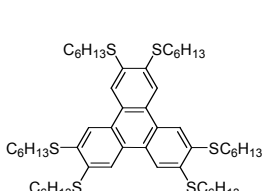
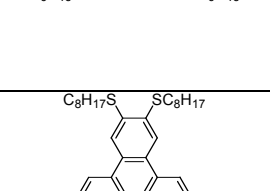
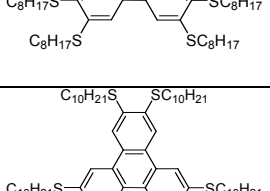
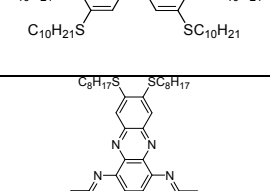
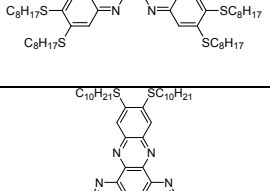
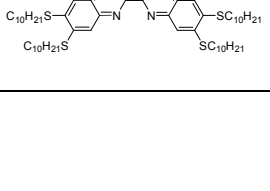
	1.0×10^{-3} (Col _{ho})	hole	TOF	41
	0.71×10^{-3} (Col _h)	hole	TOF	53
	2×10^{-3} (Col _h)	N/A	PR-TRMC	54
	0.1×10^{-3} (Col _h)	hole	TOF	53
	2×10^{-3} (Col _h)	N/A	PR-TRMC	55
	8×10^{-3} (73, Col _h)	N/A	PR-TRMC	30
	8.7×10^{-2} (65, H)	hole	TOF	2
	10^{-3} - 10^{-2} (Col _h)	hole	TOF	2
	0.1 (Col _{hh})			
	0.015 (60, Col _h)	N/A	PR-TRMC	30
	0.02 (70, Col _h)	N/A	PR-TRMC	44
	0.05	N/A	PR-TRMC	19
	0.26	N/A	PR-TRMC	19

Table 1.1 (CONT.)

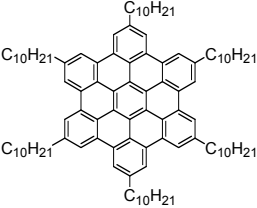
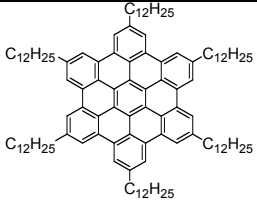
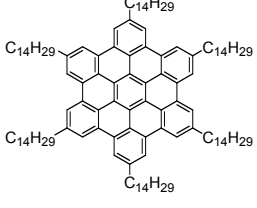
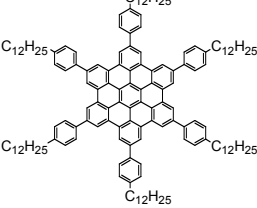
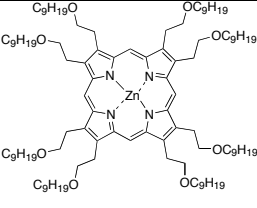
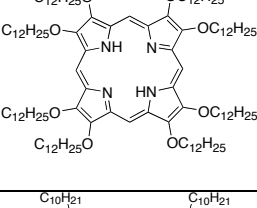
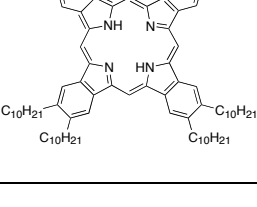
	0.26 (133, Col _h)	N/A	PR-TRMC	56
	0.38 (110, Col _h)	N/A	PR-TRMC	56
	0.31 (116, Col _h)	N/A	PR-TRMC	56
	0.46 (192, Col)	N/A	PR-TRMC	56
	6.0×10^{-3} (130, Col)	N/A	PR-TRMC	10
	0.14 (97, Col)	N/A	PR-TRMC	57
	0.15 (173, Col _h)	N/A	PR-TRMC	58

Table 1.1 (CONT.)

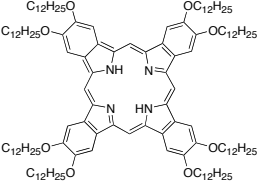
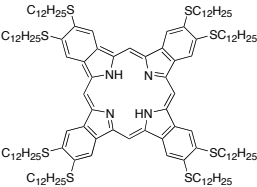
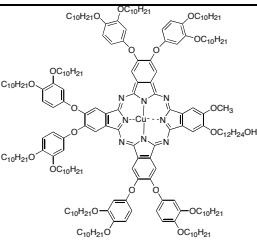
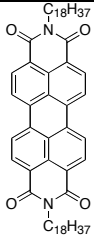
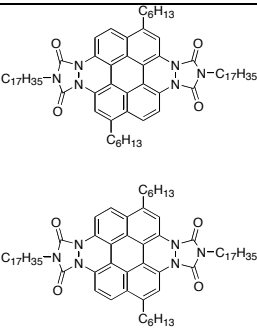
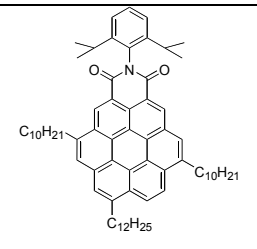
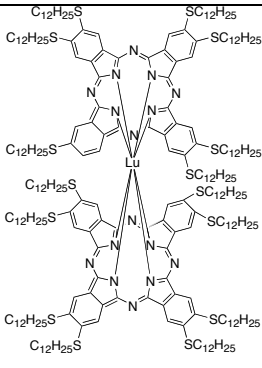
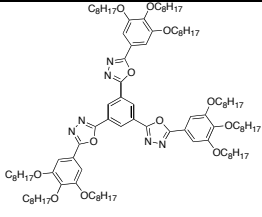
	0.05	N/A	PR-TRMC	58
	0.20	N/A	PR-TRMC	58
	2.4×10^{-3} (110, Col _h)	electron	TOF	43
	2.2×10^{-3} (110, Col _h)	hole		
	0.1 (170-190, Sm)	N/A	PR-TRMC	59
	0.1 (K and Col)	N/A	PR-TRMC	60
	0.2 (RT, Col _h)	N/A	PR-TRMC	61

Table 1.1 (CONT.)

	<p>0.71 (Col_{rh})</p> <p>0.36 (Col_{hh})</p>	<p>N/A</p>	<p>PR-TRMC</p>	<p>62</p>
	<p>$\sim 10^{-3}$ (room temperature)</p>	<p>electron</p>	<p>TOF</p>	<p>63</p>

1.7 Alignment of discotic liquid crystals

Discotic liquid crystals can self-assemble into 1-D columns, providing efficient channels for charge carriers to transport through the materials, such that they can have relatively high charge carrier mobilities. Ideally, if all the columns that are formed in the columnar liquid crystalline phases can be aligned parallel to each other and perpendicular to the electrodes when used in devices, the charge carriers would travel the shortest distance through the materials and the charge carrier mobilities would have the largest component (100%) along the direction normal to the electrodes, thus, providing the devices with the best possible performance if other parameters are optimal at the same time. Moreover, in uniformly aligned columnar phases, the charge carriers will experience minimum amount of boundaries between otherwise randomly distributed

columns. Therefore, alignment of discotic liquid crystals is important to improve the charge-transport process in columnar liquid crystalline materials and the performance of the devices using discotic liquid crystals as charge-transport materials.

There are two types of alignments of discotic liquid crystals that can be beneficial for electronics and optoelectronics. When the director of the discs is perpendicular to the plane of the substrate, the alignment is called *homeotropic* alignment where the discs take the “face-on” orientation.²¹ On the other hand, when the director of the discs is parallel to the plane of the substrate, the alignment is called *homogeneous* alignment where the discs take the “edge-on” orientation.²¹ Unfortunately, it has been found that most discotic liquid crystals do not form these two types of alignment spontaneously.⁶⁴ Thereby, surface treatments of the substrate or external driving forces have to be applied when attempting to align discotic liquid crystals.

Although significant efforts have been directed toward the design, synthesis and characterization of charge carriers mobilities of discotic liquid crystals, the success of incorporating them into efficient devices is still limited presumably due to the challenges in both material processing and alignment of the discs. Compared to the alignment of nematic liquid crystals,⁶⁵ uniform alignments of columnar discotic liquid crystals over a large area have proven more difficult to realize and only few methods have been reported. Lyotropic perylene diimide liquid crystals have been reported to form uniform alignment with the discs perpendicular to the glass substrate using ionic self-assembly (ISA) method.⁶⁶ In this method, the materials are dissolved in solvents in which the materials can form lyotropic liquid crystalline phases when certain concentrations are reached. After casting the solution onto the substrate, the solvent is allowed to evaporate. Evaporation of the solvent is faster along the edge of the solution than the inner area and

the non-uniform evaporation of the solvent leads to the formation of a concentration gradient. When certain concentration is reached along the edge of the solution, the molecules start to form lyotropic liquid crystalline phase at this so called “phase-transition front” (PTF). It was observed that PTF directed alignment of liquid crystals occurred over several square centimeters.⁶⁶ In another recent example, triphenylene derivatives have been demonstrated to have an appreciable degree of uniform “edge-on” orientation on friction transfer poly(tetrafluoroethylene) (PTFE) orientation layers after annealing the spin-coated films.⁶⁷ Photoswitching of a triphenylene derivative from its homeotropic alignment to homogeneous or oblique alignment has recently achieved by vibrational excitation of the mesogens using an infrared laser source.⁶⁸ In this method, a near infra-red (NIR) light source was irradiated onto a homeotropic thin film of a hexakisheptyloxy triphenylene derivative heated at 90 - 99 °C, absorption of light by the C=C bonds of the mesogens led to excited vibronic states. As suggested by the authors that liberation of the thermal energy from the excited vibronic states can lead to alignment of the discs in a new direction.⁶⁸ The friction transfer PTFE method has been applied to the fabrication of thin-film transistors of hexabenzocoronene derivatives.⁶⁹ Well-ordered “edge-on” orientation of hexabenzocoronene discs was observed over micrometer domains by casting the hexabenzocoronene solution onto the PTFE orientation layer without further annealing the liquid crystalline thin film and field-effect hole mobilities up to 10^{-3} cm²/Vs have been obtained. However, hole mobilities of the hexabenzocoronene derivative in field effect transistors with the PTFE aligned thin films are still three orders of magnitude lower than that measured by PR-TRMC method.⁵⁶ The Müllen group has developed a so-called “zone-casting” technique to achieve large area thin films of hexabenzocoronene liquid crystals from solution with uniaxial “edge-on”

orientation of the discs, although detailed interactions between the discs and the substrates that effect such orientation are not well understood.⁷⁰ Zone casting was performed by depositing a solution of hexabenzocoronene liquid crystal through a flat nozzle onto a moving glass substrate. Thin films of aligned hexabenzocoronene liquid crystals from zone-casting method have shown to have at least one order of magnitude improvement of the field-effect hole mobilities compared to the films prepared from friction transfer PTFE method.⁷¹ In addition, Langmuir-Blodgett films of self-organized phthalocyanine liquid crystals were horizontally transferred to field-effect transistor substrates; hole mobilities up to $5 \times 10^{-6} \text{ cm}^2/\text{Vs}$ were obtained.⁷² In the examples discussed above, the device performance using aligned discotic liquid crystals is still significantly lower than would be expected from the charge carrier mobility results derived from either PR-TRMC or TOF measurements presumably due to the presence of defects within the domains and to the poor contact of the disc columns with the electrodes or substrates.^{71,72} Therefore, development of effective alignment methods for columnar discotic liquid crystals that can produce high quality thin films with minimum defects over a large area is still representing the challenges of achieving technological applications of columnar discotic liquid crystals.⁷³ It is expected that a combination of supramolecular architecture design and control of interfacial interactions through elegant self-assembly processes would lead to the development of solution processing methods for assembling columnar discotic liquid crystals into devices.

1.8 Organization of the thesis

This thesis is organized as the following: Chapter 1 provides general background on charge-transport process, charge carrier mobility characterization techniques and

discotic liquid crystals as charge-transport materials. Chapter 2 and Chapter 3 describe the syntheses, characterizations of discotic liquid crystalline perylene diimides and coronene diimides, respectively. Chapter 4 describes that the charge carrier mobility in discotic coronene diimide liquid crystals can be improved by incorporation of binary side chains. Chapter 5 describes charge-transfer chromophores other than discotic liquid crystals. Motivation and background on the charge-transfer chromophores are also briefly mentioned therein. Chapter 6 summarizes the research described in the thesis and suggests future directions that may lead to improvement of the research in charge-transport discotic liquid crystals and charge-transfer chromophores.

1.9 References

1. (a) Tang, C. W.; VanSlyke, S. A. *Appl. Phys. Lett.* **1987**, *51*, 913-915. (b) Horowitz, G.; Fichou, D.; Peng, X.; Xu, Z.; Garnier, F. *Solid State Comm.* **1989**, *72*, 381-384. (c) Tang, C. W. *Appl. Phys. Lett.* **1985**, *48*, 183-185. (d) Chesterfield, R. J.; Newman, C. R.; Pappenfus, T. M.; Ewbank, P. C.; Haukaas, M. H.; Mann, K. R.; Miller, L. L.; Frisbie, C. D. *Adv. Mater.* **2003**, *15*, 1278-1282. (e) Kozlov, V. G.; Bulovic, V.; Burrows, P. E.; Forrest, S. R. *Nature*, **1997**, *389*, 362-364. (f) Peumans, P.; Bulovic, V.; Forrest, S. R. *Appl. Phys. Lett.* **2000**, *76*, 3855-3857. (g) Pope, M.; Swenberg, C. E. *Electronic Processes in Organic Crystals and Polymers*, Oxford, New York, 1999.
2. Lewerenz, H. J.; Jungblut, H. *Photovoltaic – Grundlagen und Anwendungen* Springer, Berlin, Heidelberg, New York, 1995.
3. (a) Ling, M. M.; Bao, Z. *Chem. Mater.* **2004**, *16*, 4824-4840. (b) Kelley, T. W.; Baude, P. F.; Gerlach, C.; Endre, D. E.; Muyres, D.; Haase, M. A.; Vogel, D. E.; Theiss, S. D. *Chem. Mater.* **2004**, *16*, 4413-4422.
4. Stolka, M.; Janus, J. F.; Pai, D. M. *J. Phys. Chem.* **1984**, *88*, 4707
5. Naka, S.; Okada, H.; Onnagawa, H.; Tsutsui, T. *Appl. Phys. Lett.* **2000**, *76*, 197
6. Wu, C.-C.; Liu, T.-L.; Hung, W.-Y.; Lin, Y.-T.; Wong, K.-T.; Chen, R.-T.; Chen, Y.-M.; Chien, Y.-Y. *J. Am. Chem. Soc.* **2003**, *125*, 3710.
7. (a) Chiang, C. K.; Fincher, C. R.; Park, Y. W.; Heeger, A. J.; Shirakawa, H.; Louis, E. J.; Gau, S. G.; MacDiarmid, A. G. *Phys. Rev. Lett.* **1977**, *39*, 1098-1101. (b) Shirota, Y.; Noma, N.; Shimizu, Y.; Kanega, H.; Jeon, I.-R.; Nawa, K.; Kakuta, T.; Yasui, H.; Namba, K. *Synth. Met.* **1991**, *41-43*, 3031. (c) Timpanaro, S.; Kemerink, M.; Touwslager, F. J.; De Kok, M. M.; Schrader, S. *Chem. Phys. Lett.* **2004**, *394*, 339-343.
8. Adam, D.; Schuhmacher, P.; Simmerer, J.; Häussling, L.; Siemensmeyer, K.; Etzbach, K. H.; Ringsdorf, H.; Haarer, D. *Nature*, **1994**, *371*, 141-143.
9. Jain, S. C.; Geens, W.; Mehra, A.; Kumar, V.; Aernouts, T.; Poortman, J.; Mertens, R.; Willander, M. *J. Appl. Phys.* **2001**, *89*, 3804-3810.
10. Schouten, P. G.; Warman, J. M.; de Haas, M. P.; Fox, M. A.; Pan, H.-L. *Nature*, **1991**, *353*, 736-737.

11. (a) Roth, S. *One-Dimensional Metals* Wiley-VCH, Weinheim, 1995. (b) Fichou, D. *Handbook of Oligo- and Polythiophenes* Wiley-VCH, Weinheim, 1999.
12. Ashcroft, N. W.; Mermin, N. D. *Solid State Physics* Holt-Saunders, London, 1976.
13. Warta, W.; Stehle, R.; Karl, N. *Appl. Phys. A* **1985**, *36*, 163.
14. Horowitz, G. *Adv. Mater.* **1998**, *10*, 365-377.
15. (a) Brédas, J.-L.; Cornil, J.; Beljonne, D.; Dos Santos, D. A.; Shuai, Z. *Acc. Chem. Res.* **1999**, *32*, 267. (b) Duke, C. B.; Schein, L. B. *Phys. Today*, **1980**, *33*, 42.
16. (a) van de Craats, A. M.; Warman, J. M.; Müllen, K.; Geerts, Y.; Brand, J. D. *Adv. Mater.* **1998**, *10*, 36-38. (b) Palenberg, M. A.; Silbey, R. J.; Malagoli, M.; Brédas, J.-L. *J. Chem. Phys.* **2000**, *112*, 1541-1546.
17. Nelson, S. F.; Lin, Y.-Y.; Gundlach, D. J.; Jackson, T. N. *Appl. Phys. Lett.* **1998**, *72*, 1854.
18. Le Comber, P. G.; Spear, W. E. *Phys. Rev. Lett.* **1970**, *25*, 509.
19. Lemaire, V.; da Silva Filho, D. A.; Coropceanu, V.; Lehmann, M.; Geerts, Y.; Piris, J.; Debije, M. G.; van de Craats, A. M.; Senthilkumar, K.; Siebbeles, L. D. A.; Warman, J. M.; Brédas, J.-L.; Cornil, J. *J. Am. Chem. Soc.* **2004**, *126*, 3271-3279.
20. Barbara, P. F.; Meyer, T. J.; Ratner, M. A. *J. Phys. Chem.* **1996**, *100*, 13148-13168.
21. Demus, D.; Goodby, J.; Gray, G. W.; Spiess, H. W.; Vill, V. *Handbook of Liquid Crystals* Wiley-VCH, Weinheim, New York, 1998.
22. Friberg, S. *Lyotropic Liquid Crystals*, Advances in Chemistry Series, American Chemical Society, Washington, DC, **1976**.
23. Hoger, S.; Enkelmann, V.; Bonrad, K.; Tschierske, C. *Angew. Chem. Int. Ed.* **2000**, *39*, 2268-2270.
24. Maeda, F.; Hatsusaka, K.; Ohta, K.; Kimura, M. *J. Mater. Chem.* **2003**, *13*, 243-251.
25. Strohriegel, P.; Grazulevicius, J. *Adv. Mater.* **2002**, *14*, 1439-1452

26. Maldonado, J.-L.; Bishop, M.; Fuentes-Hernandez, C.; Caron, P.; Domercq, B.; Zhang, Y.; Barlow, S.; Thayumanavan, S.; Malagoli, M.; Bredas, J.-L.; Marder, S. R.; Kippelen, B. *Chem. Mater.* **2003**, *15*, 994-999.
27. Tang, C. W.; VanSlyke, S. A. *Appl. Phys. Lett.* **1987**, *51*, 913-915.
28. (a) Newman, C. R.; Frisbie, C. D.; da Silva Filho, D. A.; Bredas, J.-L.; Ewbank, P. C.; Mann, K. R. *Chem. Mater.* **2004**, *16*, 4436-4451. (b) Katz, H. E. *Chem. Mater.* **2004**, *16*, 4748-4756.
29. Jurchescu, O. D.; Baas, J.; Palstra, T. T. M. *Appl. Phys. Lett.* **2004**, *84*, 3061-3063.
30. (a) Podzorov, V.; Sysoev, S. E.; Loginova, E.; Pudalov, V. M.; Gershenson, M. E. *Appl. Phys. Lett.* **2003**, *83*, 3504-3506. (b) Sundar, V. C.; Zaumseil, J.; Podzorov, V.; Menard, E.; Willett, R. L.; Someya, T.; Gershenson, M. E.; Rogers, J. A. *Science*, **2004**, *303*, 1644-1646. (c) Podzorov, V.; Menard, E.; Borissov, A.; Kiryukhin, V.; Rogers, J. A.; Gershenson, M. E. *Phys. Rev. Lett.* **2004**, *93*, 086602.
31. Menard, E.; Podzorov, V.; Hur, S.-H.; Gaur, A.; Gershenson, M. E.; Rogers, J. A. *Adv. Mater.* **2004**, *16*, 2097-2101
32. Haddon, R. C.; Perel, A. S. Morris, R. C.; Palstra, T. T. M.; Hebard, A. F.; Flemming, R. M. *Appl. Phys. Lett.* **1995**, *67*, 121-123.
33. (a) Tulevski, G. S.; Miao, Q.; Fukuto, M.; Abram, R.; Ocko, B.; Pindak, R.; Steigerwald, M. L.; Kagan, C. R.; Nuckolls, C. *J. Am. Chem. Soc.* **2004**, *126*, 15048-15050. (b) de Boer, R. W.; Klapwijk, T. M.; Morpurgo, A. F. *Appl. Phys. Lett.* **2003**, *83*, 4345-4347. (c) Katz, H. E.; Kloc, C.; Sundar, V.; Zaumseil, J.; Briseno, A.; Bao, Z. *J. Mat. Res.* **2004**, *19*, 1995-1998.
34. Bendikov, M.; Wudl, F. *Chem. Rev.* **2004**, *104*, 4891-4945.
35. Mas-Torrent, M.; Durkut, M.; Hadley, P.; Ribas, X.; Rovira, C. *J. Am. Chem. Soc.* **2004**, *126*, 984-985.
36. (a) Halik, M.; Klauk, H.; Zschieschang, U.; Schmid, G.; Radlik, W.; Ponomarenko, S.; Kirchmeyer, S.; Weber, W. *J. Appl. Phys.* **2003**, *93*, 2977-2983. (b) Facchetti, A.; Mushrush, M.; Yoon, M.-H.; Hutchison, G. R.; Ratner, M. A.; Marks, T. J. *J. Am. Chem. Soc.* **2004**, *126*, 13859-13874.
37. (a) Malenfant, P. R. L.; Dimitrakopoulos, C. D.; Gelorme, J. D.; Kosbar, L. L.; Graham, T. O.; Curioni, A.; Andreoni, W. *Appl. Phys. Lett.* **2002**, *80*, 2517-2519. (b) Chesterfield, R. J.; McKeen, J. C.; Newman, C. R.; Frisbie, C. D. *J. Appl. Phys.* **2004**, *95*, 6396-6405.

38. (a) Newman, C. R.; Frisbie, C. D.; da Silva Filho, D. A.; Bredas, J.-L.; Ewbank, P. C.; Mann, K. R. *Chem. Mater.* **2004**, *16*, 4436-4451. (b) Katz, H. E. *Chem. Mater.* **2004**, *16*, 4748-4756.
39. (a) Moon, H.; Zeis, R.; Borkent, E.-J.; Besnard, C.; Lovinger, A. J.; Siegrist, T.; Kloc, C.; Bao, Z. *J. Am. Chem. Soc.* **2004**, *126*, 15322-15323. (b) Payne, M. M.; Parkin, S. R.; Anthony, J. E.; Kuo, C.-C.; Jackson, T. N. *J. Am. Chem. Soc.* **2005**, *127*, 4986-4987.
40. (a) Eichhorn, H. *J. Porphyrins Phthalocyanines* **2000**, *4*, 88-102 (b) Ohta, K.; Hatsusaka, K.; Sugibayashi, M.; Ariyoshi, M.; Ban, K.; Maeda, F.; Naito, R.; Nishizawa, K.; van de Craats, A. M.; Warman, J. M. *Mol. Cryst. Liq. Cryst.* **2003**, *397*, 25-45. (c) Warman, J. M.; de Haas, M. P.; Dicker, G.; Grozema, F. C.; Piris, J.; Debije, M. G. *Chem. Mater.* **2004**, *16*, 4600-4609 (d) Warman, J. M.; van de Craats, A. M. *Mol. Cryst. Liq. Cryst.* **2003**, *396*, 41-72.
41. Adam, D.; Closs, F.; Frey, T.; Funhoff, D.; Haarer, D.; Ringsdorf, H.; Schuhmacher, P.; Siemensmeyer, K. *Phys. Rev. Lett.* **1993**, *70*, 457-460.
42. (a) Simmerer, J.; Glusen, B.; Paulus, W.; Kettner, A.; Schuhmacher, P.; Adam, D.; Etzbach, K. H.; Siemensmeyer, K.; Wendorff, J. H.; Ringsdorf, H. *Adv. Mater.* **1996**, *8*, 815. (b) Kreouzis, T.; Donovan, K. J.; Boden, N.; Bushby, R. J.; Iozman, O. R.; Liu, Q. *J. Chem. Phys.* **2001**, *114*, 1797.
43. Fujikake, H.; Murashige, T.; Sugibayashi, M.; Ohta, K. *Appl. Phys. Lett.* **2004**, *85*, 3474-3476.
44. van de Craats, A. M.; Warman, J. M.; de Haas, M. P.; Adam, D.; Simmerer, J.; Haarer, D.; Schuhmacher, P. *Adv. Mater.* **1996**, *8*, 823.
45. (a) Mott, N. F.; Gurney, D. *Electronic Processes in Ionic Crystals* Academic, New York, 1970. (b) Murgatroyd, P. N. *J. Phys.* 1970, D3, 151-156.
46. (a) Bozano, L.; Carter, S. A.; Scott, J. C.; Malliaris, G. G.; Brock, P. J. *Appl. Phys. Lett.*, **1999**, *74*, 1132-1134 (b) Reynaert, J.; Arkhipov, V. I.; Borghs, G.; Heremans, P. *Appl. Phys. Lett.*, **2004**, *85*, 603-605 (c) Blom, P. W. M.; Tanase, C.; de Leeuw, D. M.; Coehoorn, R. *Appl. Phys. Lett.*, **2005**, *86*, 092105-1-3.
47. Bäessler, H. *Phys. Status Solidi B* **1993**, *175*, 15.
48. Tokuhisa, H.; Era, M.; Tsutsui, T. *Adv. Mater.* **1998**, *10*, 404-407.
49. Funahashi, M.; Hanna, J.-I. *Adv. Mater.* **2005**, *17*, 594-598.
50. Chandrasekhar, S.; Sadashiva, B. K.; Suresh, K. A. *Pramana* **1977**, *9*, 471

51. Donovan, K. J. ; Kreouzis, T.; Scott, K.; Bunning, J. C.; Bushby, R. J.; Boden, N.; Lozman, O. R.; Movaghar, B. *Mol. Cryst. Liq. Cryst.* **2003**, *396*, 91-112.
52. Bushby, R.; Lozman, O. R. *Curr. Opin. Sol. St. Mater. Sci.* **2002**, *6*, 569-578.
53. Kreouzis, T.; Donovan, K. J.; Boden, N.; Bushby, R. J.; lozman, O. R.; Liu, Q. *J. Chem. Phys.* **2001**, *114*, 1797.
54. van de Craats, A. M. ; de Haas, M. P. ; Warman, J. M. *Syn. Met.* **1997**, *86*, 2125.
55. van de Craats, A. M. ; Schouten, P. G. ; Warman, J. M. *J. Jap. Liq. Cryst. Soc.* **1998**, *2*, 12.
56. van de Craats, A. M. ; Warman, J. M. ; Fechtenkötter, A. ; Brand, J. D.; Harbison, M. A.; Müllen, K. *Adv. Mater.* **1999**, *11*, 1469-1472.
57. Schouten, P. G.; Warman, J. M.; de Haas, M. P.; van der Pol, J. F.; Zwikker, J. W. *J. Am. Chem. Soc.* **1992**, *114*, 9028-9034.
58. Van de Craats, A. M.; Warman, J. M. *Syn. Met.* **2001**, *121*, 1287-1288.
59. Struijk, C. W.; Sieval, A. B.; Dakhorst, J. E. J.; Dijk, M.; Kimkes, P.; Koehorst, R. B. M.; Donker, H.; Schaafsma, T. J.; Picken, S. J.; Craats, A. M.; Warman, J. M.; Zuilhof, H.; Sudhölter, E. J. R. *J. Am. Chem. Soc.* **2000**, *122*, 11057-11066.
60. van de Craats, A. M.; Warman, J. M.; Schlichting, P.; Rohr, U.; Geerts, Y.; Müllen, K. *Syn. Met.* **1999**, *102*, 1550-1551.
61. Rohr, U.; Kohl, C.; Müllen, K.; van de Craats, A.; Warman, J. *J. Mater. Chem.* **2001**, *11*, 1789-1799.
62. Ban, K.; Nishizawa, K.; Ohta, K.; van de Craats, A. M.; Warman, J. M.; Yamamoto, I.; Shirai, H. *J. Mater. Chem.* **2001**, *11*, 321-331.
63. Zhang, Y. D.; Jespersen, K. G.; Kempe, M.; Kornfield, J. A.; Barlow, S.; Kippelen, B.; Marder, S. R. *Langmuir*, **2003**, *19*, 6534-6536.
64. (a) Hatsusaka, K.; Ohta, K.; Yamamoto, I.; Shirai, H. *J. Mater. Chem.* **2001**, *11*, 423-433. (b) Simpson, C. D.; Wu, J.; Watson, M. D.; Müllen, K. *J. Mater. Chem.* **2004**, *14*, 494-504.
65. (a) Ikeda, T.; Sasaki, T.; Ichimura, K. *Nature*, **1993**, *361*, 428. (b) Ikeda, T.; Tsutsumi, O. *Nature*, **1995**, *268*, 1873. (c) Tsutsumi, O.; Ikeda, T. *Curr. Opin. Sol. St. Mater. Sci.* **2002**, *6*, 563-568. (d) Wilderbeek, H. T. A.; Teunissen, J.-P.; Bastiaansen, C. W. M.; Broer, D. J. *Adv. Mater.* **2003**, *15*, 985-988. (e) Varghese, S.; Narayanankutty, S.; Bastiaansen, C. W. M.; Crawford, G. P.; Broer, D. J. *Adv. Mater.* **2004**, *16*, 1600-1605. (f) Wilderbeek, H. T. A.; van der Meer, F. J. A.;

- Feldman, K.; Broer, D. J.; ; Bastiaansen, C. W. M. *Adv. Mater.* **2002**, *14*, 655-658.
66. Zakrevskyy, Y.; Faul, C. F.J.; Guan, Y.; Stumpe, J. *Adv. Funct. Mater.* **2004**, *14*, 835-841.
67. Zimmermann, S.; Wendorff, J. H.; Weder, C. *Chem. Mater.* **2002**, *14*, 2218-2223.
68. Monobe, H.; Awazu, K.; Shimizu, Y. *Adv. Mater.* **2000**, *12*, 1495-1499.
69. van der Craats, A. M.; Stutzmann, N.; Bunk, O.; Nielsen, M. M.; Watson, M.; Müllen, K.; Chanzy, H. D.; Siringhaus, H.; Friend, R. H. *Adv. Mater.* **2003**, *15*, 495-499.
70. Tracz, A.; Jeszka, J. K.; Watson, M. D.; Pisula, W.; Müllen, K.; Pakula, T. *J. Am. Chem. Soc.* **2003**, *125*, 1683-1684
71. Pisula, W.; Menon, A.; Stepputat, M.; Lieberwirth, I.; Kolb, U.; Tracz, A.; Siringhaus, H.; Pakula, T.; Müllen, K. *Adv. Mater.* **2005**, *17*, 684-689.
72. Donley, C. L.; Zangmeister, R. A. P.; Xia, W.; Minch, B.; Drager, A.; Cherian, S. K.; LaRussa, L.; Kippelen, B.; Domercq, B.; Mathine, D. L.; O'Brien, D. F.; Armstrong, N. R. *J. Mater. Res.* **2004**, *19*, 1087-2099.
73. Kawata, K. *Chem. Rec.* **2002**, *2*, 59-80.

CHAPTER 2

**ROOM-TEMPERATURE DISCOTIC LIQUID CRYSTALLINE PERYLENE
DIIMIDES AS ELECTRON-TRANSPORT MATERIALS**

2.1 Introduction

For organic semiconductors including discotic liquid crystals, the development of electron-transport materials is still behind that for hole-transport materials.¹ In general, there are more examples of good hole-transport materials than that of electron-transport materials. Also it has been demonstrated that electron mobilities can be significantly decreased when exposed to oxygen or air.² In order to make efficient organic electronic devices such as photovoltaic cells, field-effect transistors *etc.*, it is necessary to improve charge carrier mobility and air-stability of electron-transport materials.

To obtain electron-transport discotic liquid crystals with high electron mobilities and air-stability, it is important to choose an appropriate aromatic core, which can largely determine the electronic properties of the liquid crystals. As an entry point to this research, perylene diimides were chosen based on several considerations. Firstly, perylene diimides are relatively electron-deficient and usually exhibit two reversible one-electron reductions. The first reduction potential of perylene diimides typically occurs around -1.0 V *vs.* ferrocenium/ferrocene.³ Therefore, perylene diimides have been used as electron acceptors in photoinduced charge transfer systems.⁴ Secondly, the relatively large aromatic core of perylene diimides is beneficial to the formation of discotic liquid crystals, as is evidenced by the fact that both lyotropic and thermotropic perylene diimide liquid crystals have been reported in the literature.⁵ Most importantly, perylene diimides

have been demonstrated to have fairly high charge carrier mobilities. Charge carrier mobilities of $0.1 \text{ cm}^2/\text{Vs}$ and $0.2 \text{ cm}^2/\text{Vs}$ have been measured by PR-TRMC technique for *N,N'*-dioctadecyl-3,4,9,10-perylene diimide in its liquid crystalline and polycrystalline states respectively.⁶ A similar value was found for a tetrachloro-substituted perylene diimide analogue.⁷ High field-effect mobilities have also been demonstrated in *n*-type thin-film transistors using vapor deposited *N,N'*-dialkyl-perylene diimides; electron mobilities as high as $1.7 \text{ cm}^2/\text{Vs}$ have been observed in *N,N'*-dioctadecyl-3,4,9,10-perylene diimide.^{2c,8} These high charge carrier mobilities indicate that perylene diimides are promising candidates for use as electron-transport liquid crystals. The perylene diimides reported are usually polycrystalline or form liquid crystals only at high temperatures and some of them have several thermal transitions with narrow temperature range of the liquid crystalline phases. Charge carrier mobilities typically experience abrupt change upon phase transitions and roughly maintain the same value within the same liquid crystalline phase.⁹ Therefore, it is desirable to have discotic liquid crystals that can form liquid crystalline phases at room temperature with a wide temperature range for practical applications.

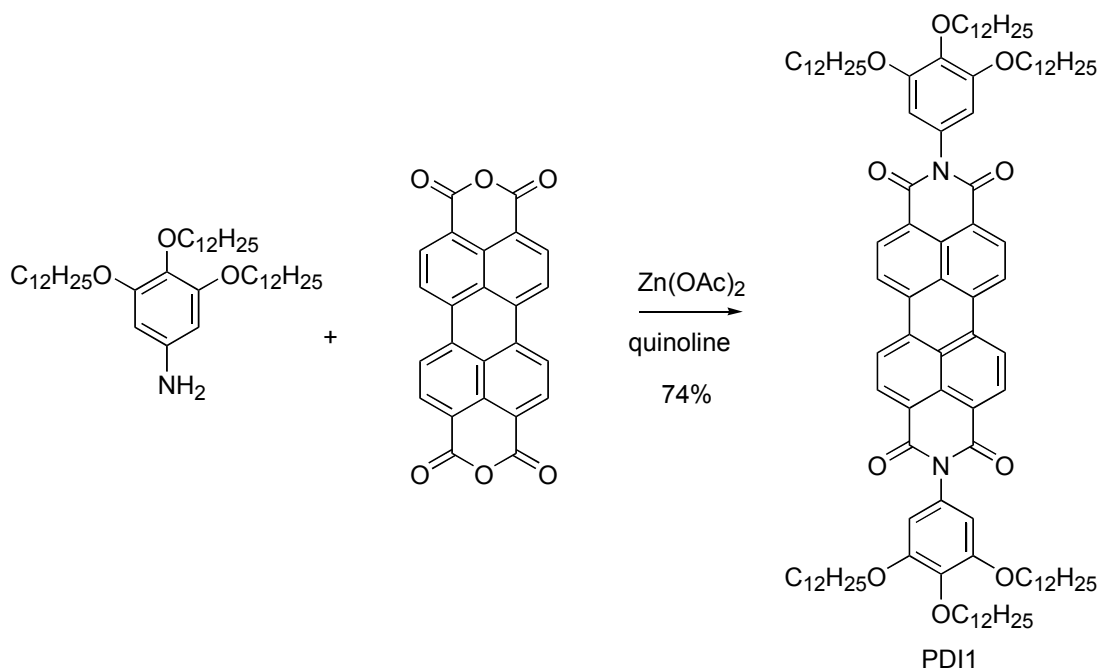
N,N'-Bis[3,4,5-tri(dodecyloxy)phenyl]-3,4,9,10-tetracarboxylic perylene diimide (**PDI1**) displays a liquid crystalline phase in the range of $-10 \text{ }^\circ\text{C}$ — $360 \text{ }^\circ\text{C}$.^{5c} This room-temperature liquid crystal attracted our attention as we were seeking charge transport materials that could be used as liquid crystals at room temperature. However, the high clearing point of **PDI1** makes processing of the material rather difficult. Introduction of a flexible $-\text{CH}_2-$ linker between the 3,4,5-tri(dodecyloxy)phenyl group and the imide nitrogen in *N,N'*-bis[3,4,5-tri(dodecyloxy)benzyl]-3,4,9,10-tetracarboxylic perylene diimide (**PDI2**)¹⁰ lowers the clearing point of the material from $360 \text{ }^\circ\text{C}$ in **PDI1** to $226 \text{ }^\circ\text{C}$

in **PDI2**. Therefore, thermal processing of **PDI2** from its melt becomes significantly easier. In addition, due to the smaller twist of the side group expected in **PDI2** (benzyl) than in **PDI1** (phenyl), the molecules of **PDI2** may have a stronger intermolecular interaction than the molecules of **PDI1**.

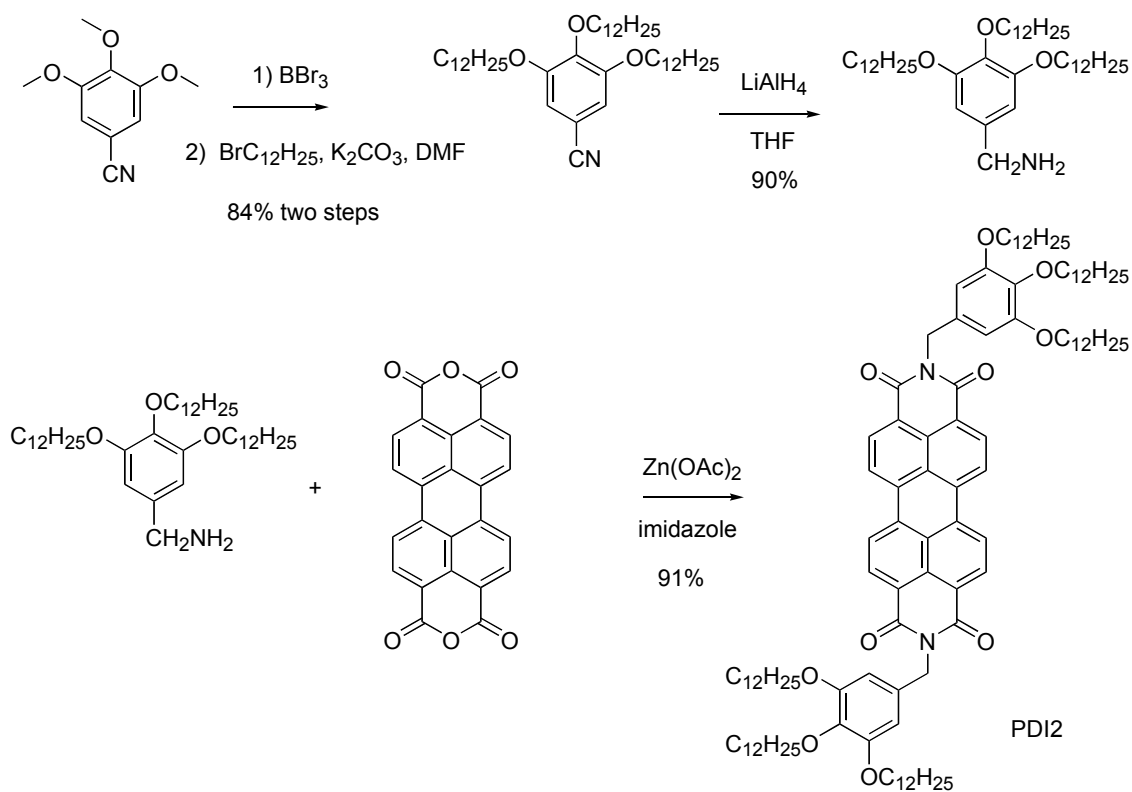
This chapter describes the properties of two room-temperature perylene diimide liquid crystals (**PDI1** and **PDI2**) and their SCLC characteristics (by Junsheng Yu, Kippelen group).

2.2 Synthesis

The perylene diimide derivatives were synthesized by condensation of the corresponding amines with perylene dianhydride under basic conditions. **PDI1** was synthesized with tridodecyloxyaniline in quinoline with $Zn(OAc)_2$ as the catalyst according to the literature procedure^{5c} (Scheme 2.1). **PDI2** was synthesized with tridodecyloxybenzyl amine in melted imidazole (Scheme 2.2), the synthesis of which was also recently reported¹⁰.



Scheme 2.1 Synthesis of **PDI1**



Scheme 2.2 Synthesis of **PDI2**

2.3 Absorption properties

The absorption spectra of the two PDIs in chloroform and in thin films prepared by drop-casting method are shown in Figure 2.1. The absorption spectra of both compounds in chloroform have the characteristic $S_0 \rightarrow S_1$ transition with the fine vibronic signature of perylene diimides. Usually the absorption maximum of **PDIs** does not change significantly with different imide groups due to the presence of nodes in both HOMO and LUMO at the imide nitrogen atom.¹¹ A relatively large difference has been observed for a perylene diimide with an electron deficient pentafluorophenyl group; its absorption maximum is red-shifted by 5 nm, compared to that of its phenyl group analogue.¹² The $0 \rightarrow 0$ transition for these two **PDIs** differs only by 1 nm (**PDI1** at 528 nm and **PDI2** at 529 nm). The low intensity band at 365 nm is attributed to the $S_0 \rightarrow S_2$ electronic transition¹³ which results from the polarization along the shorter molecular axis of perylene diimides and may be responsible for two-photon absorption observed in some perylene derivatives.¹⁴ It is interesting to note that the absorption spectra of the two compounds in solid state have different characteristics than that in solution. The absorption maximum for both compounds is shifted from the $0 \rightarrow 0$ transition (529 nm for **PDI1** and 528 nm for **PDI2**) in solution to the $0 \rightarrow 1$ transition (498 nm for **PDI1** and 507 nm for **PDI2**) in solid state, possibly due to strong exciton-phonon coupling in solid state.¹⁵ For both compounds, the $0 \rightarrow 0$ transition (539 nm for **PDI1** and 550 nm for **PDI2**) in solid state is red-shifted compared to that in solution, suggesting possible formation of *J*-aggregates.¹⁶

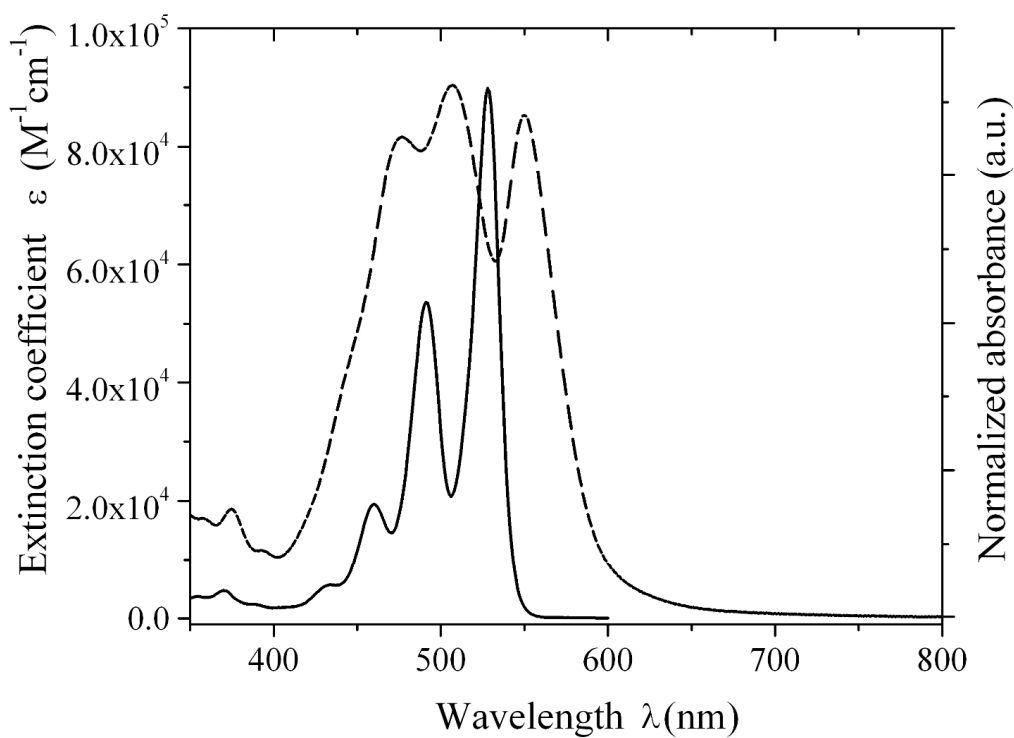
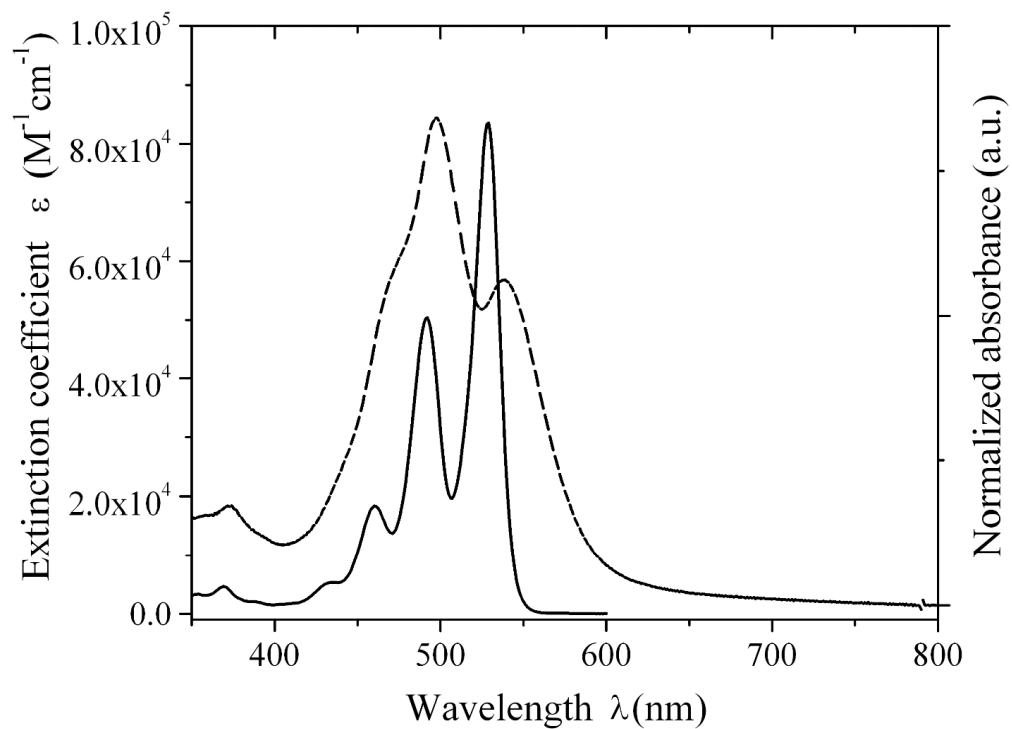


Figure 2.1 Absorption spectra of **PDI1** (top) and **PDI2** (bottom) in chloroform solution (solid line) and in thin film prepared by drop-casting (dashed line).

2.4 Electrochemical properties

The cyclic voltammetry (CV) of the two **PDI**s reveals two successive reversible one-electron reduction waves (Figure 2.2). Their reduction potentials are slightly different with **PDI1** being easier to reduce than **PDI2** (Table 1.1). No oxidation was observed in the solvent window for both compounds.

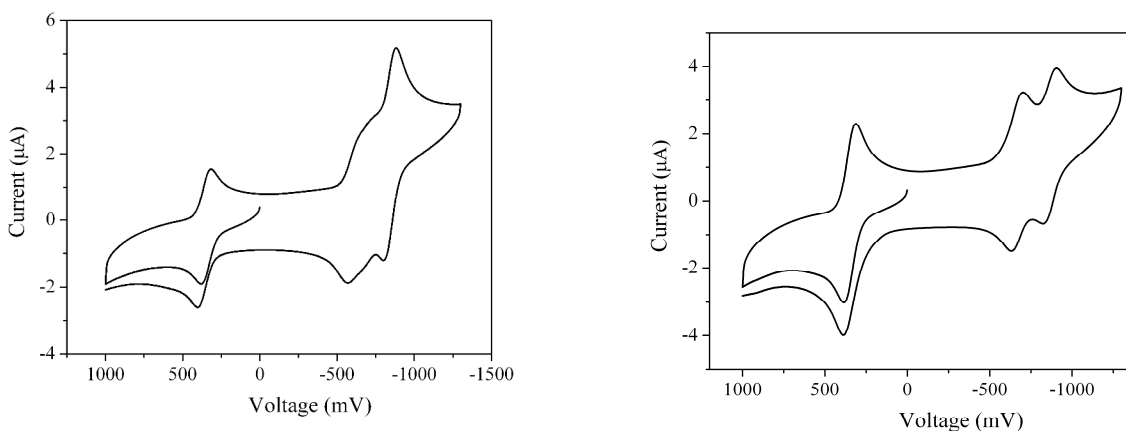


Figure 2.2 Cyclic voltammograms of **PDI1** (left) and **PDI2** (right) in 0.1 M Bu_4NPF_6 dichloromethane solution with Fc^+/Fc as internal standard (reversible waves between 0.5 and 0 V), scan rate = 50 mV/s.

Table 2.1 Summary of the electrochemical data of perylene diimide LCs vs. Fc^+/Fc

	X^+/X (V)		X^{2-}/X^- (V)	
	Experimental data	Literature data	Experimental data	Literature data
PDI1	-0.97	-0.98 (ref. 5c)	-1.19	-1.19 (ref. 5c)
PDI2	-1.02	N/A	-1.21	N/A

The ionization potential (IP) and electron affinity (EA) of the materials in solid state can be estimated by comparison of the electrochemical and/or photospectroscopic data between the **PDI**s and reference compounds, such as TPD and Alq₃, with known IP and EA measured directly from photoelectron spectroscopy (PES) and inverse photoelectron spectroscopy (IPES) respectively.¹⁷ The EA of the **PDI**s can be estimated by comparing them with Alq₃, according to:

$$EA(\mathbf{PDI}) - EA(\text{Alq}_3) = E_{1/2}(\text{Alq}_3^{0/-}) - E_{1/2}(\mathbf{PDI}^{0/-}) \quad (2.1)$$

Taking $E_{1/2}(\text{Alq}_3^{0/-}) = -2.30 \text{ V}$ ¹⁸, $EA(\text{Alq}_3) = -2.3 \text{ eV}$ ¹⁹ and $E_{1/2}(\mathbf{PDI}^{0/-}) = -1.0 \text{ V}$, a value of -3.6 eV can be obtained for $EA(\mathbf{PDI})$.

Reversible one-electron oxidation of a similar perylene diimide has been previously observed in CV with $E_{1/2}(\mathbf{PDI}^{+/0})$ of ca. 1.2 V .²⁰ It has been shown that the substituents at the imide position do not affect the energy levels of the perylene diimides significantly,²⁰ although the substitutions can affect the molecular packing of **PDI**s in thin films and thus leading to variation in the HOMO and LUMO bandwidth.¹ Therefore, it is reasonable to expect that our **PDI**s should have similar oxidation potentials as those previously reported. Thus, the IP of the **PDI**s can be estimated by comparing them with TPD via the relation:

$$IP(\mathbf{PDI}) - IP(\text{TPD}) = E_{1/2}(\mathbf{PDI}^{+/0}) - E_{1/2}(\text{TPD}^{+/0}) \quad (2.2)$$

An $IP(\mathbf{PDI})$ of ca. 6.3 eV can be obtained, using $IP(\text{TPD}) = 5.4 \text{ eV}$,¹⁹ and $E_{1/2}(\text{TPD}^{+/0}) = 0.26 \text{ V}$ measured in similar solutions.²¹

The bulk transport gap of the **PDI**s can then be estimated to be $(EA + IP) = 2.7 \text{ eV}$, which is close to the value of 2.54 eV obtained from quantum calculation,¹ but is much larger than the optical energy gap of $E_{\text{op}} = 2.2 \text{ eV}$ estimated from the absorption onset (550 nm). The relatively large difference between the electrical energy gap and the

optical energy gap is possibly due to the overlook of the exciton binding energy. However, the HOMO (6.3 eV) and LUMO (3.6 eV) (can be experimentally probed by PES and IPES, respectively) obtained from the estimated IP and EA here, are quite different from the HOMO (5.32 eV) and LUMO (3.29 eV) levels alternatively estimated from the thin-film oxidation potential and the absorption spectrum for a similar perylene diimide by Schmidt-Mende *et al.*²² The difference may come from different estimation method employed (though Schmidt-Mende did not specify the estimation method), different stabilizations and polarizations in solution and solid state. Thus, the energy levels of the materials could be more accurately obtained through measurements by PES and IPES directly.

2.5 Liquid crystalline properties

The thermotropic properties of the two perylene diimides were studied by differential scanning calorimetry (DSC) (Figure 2.3 and Table 2.2) and polarized optical microscopy (POM) (Figure 2.4). Both materials show two thermal transitions and there is only one phase between the two transitions. Compared to **PDI1** with clearing point of 365 °C, **PDI2** has a much lower clearing point of 226°C, as expected by the introduction of a flexible -CH₂- group in **PDI2**. This lower clearing point benefits material processing of SCLC samples from the melt of the material. Typical textures²³ of columnar mesophases with focal conic fan texture for **PDI1** and broken fan texture for **PDI2** can be seen when cooling the isotropic liquid to room temperature.

The liquid crystalline phase structure was studied by X-ray diffraction (XRD) (Figure 2.5). **PDI1** has only one sharp peak in the low angle region, thus a specific mesophase can not be assigned. For **PDI2**, the presence of three well-resolved peaks in

the low angle region leads to the assignment of a hexagonal columnar mesophase with reciprocal d spacing of ca. $1: (3)^{0.5} : 2$ and a lattice parameter of 31.9 Å. Both materials lack a sharp peak in the wide-angle region of XRD, suggesting disordered mesophases.

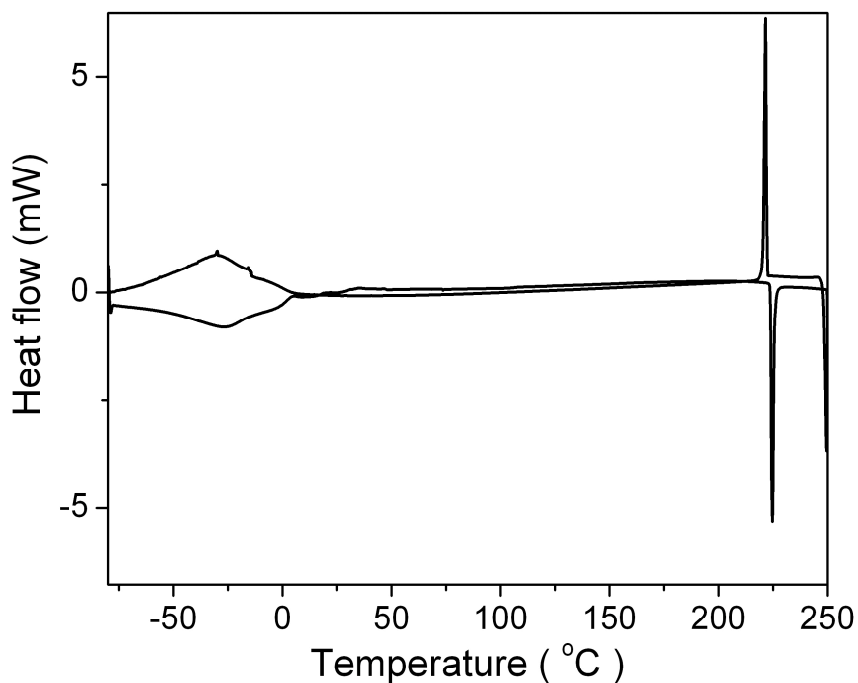


Figure 2.3 DSC (second heating-cooling cycle) of **PDI2**.

Table 2.2 Summary of the phase transition temperature T [°C] and transition enthalpy ΔH [kJ/mol] of **PDI1** and **PDI2** (second heating-cooling cycle).

	Heating		Cooling	
	T [°C] (ΔH [kJ/mol])			
PDI1	-33.0 (-11.6)	365.0 (-17.7)	354.1 (16.0)	-40.0 (12.6)
PDI2	-27.9 (-32.0)	226.0 (-17.0)	224.2 (16.7)	-30.8 (35.5)

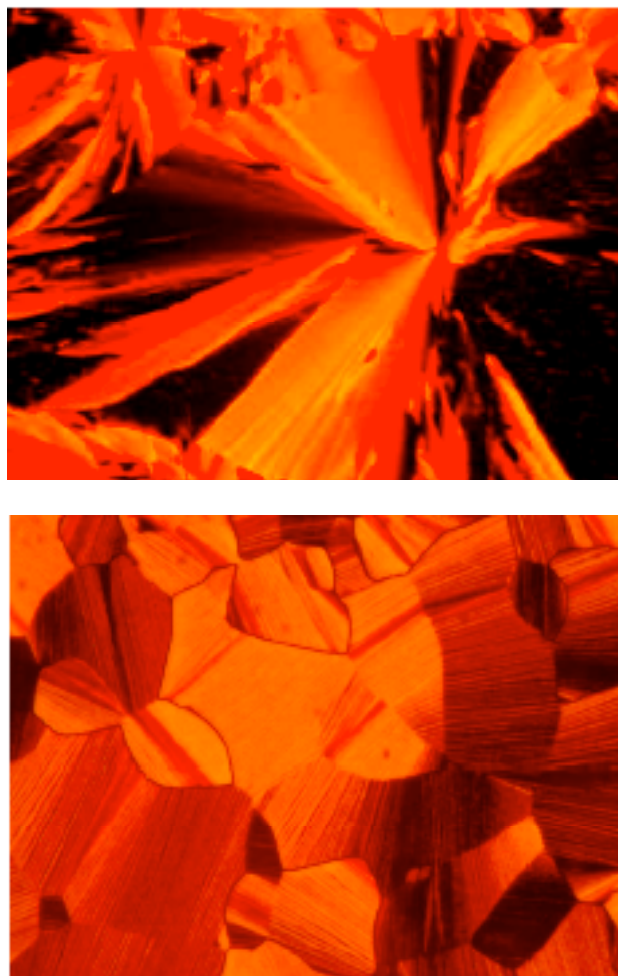


Figure 2.4 Optical textures of **PDII** (top, magnification 20 ×) and **PD12** (bottom, magnification 50 ×) between two crossed polarizers.

75

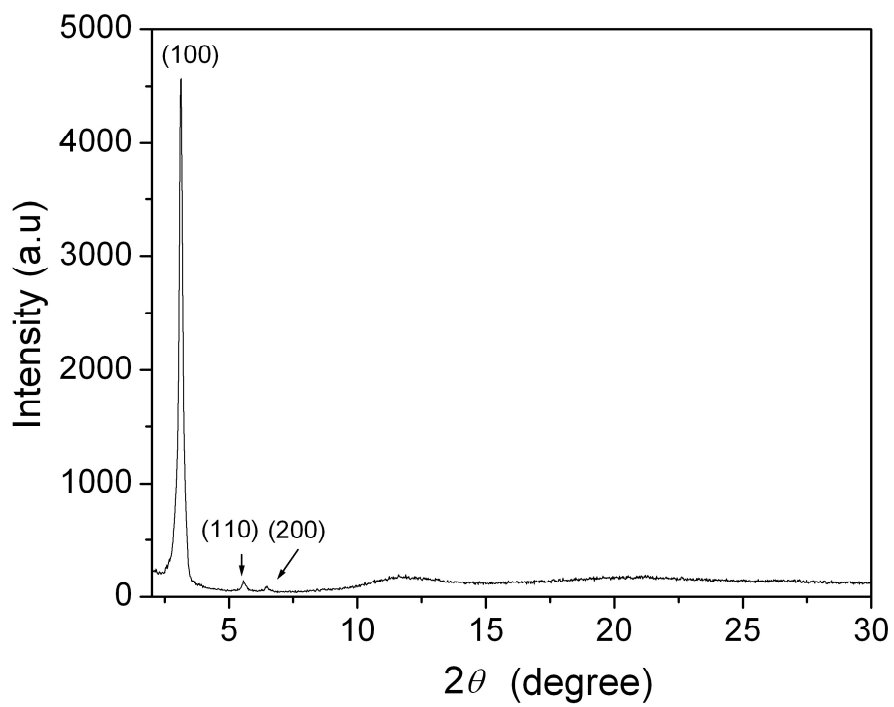
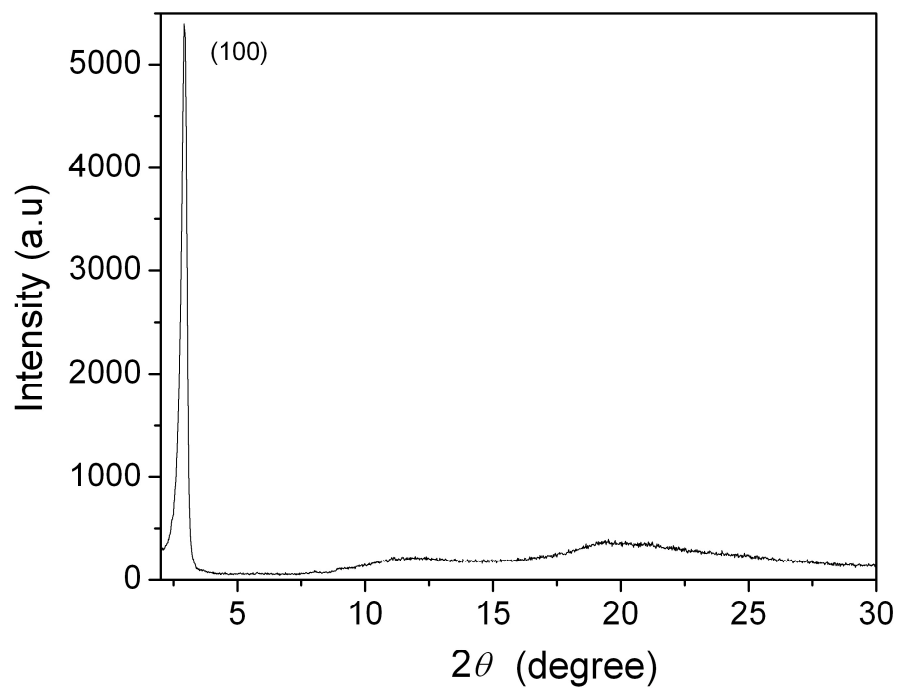


Figure 2.5 XRD of **PDI1** (top) and **PDI2** (bottom) at room temperature after cooling from the isotropic liquid.

2.6 SCLC characterization

The J - V characteristics of the perylene diimide liquid crystals were studied by SCLC technique under ambient conditions as described in Chapter 1. For **PDI2**, different cathode electrodes (Ag, ITO) were used to study the effect of charge injection process on the SCLC characteristics with ITO as the anode. Figure 2.6 shows the J - V curve of **PDI2** with the device geometry of (+)ITO/**PDI2** (5 μm)/Ag(-). At low voltage from 0.0 to 0.4 volts, the J - V curve is approximately in the ohmic region with a slope of 1.1, slightly higher than 1. The SCLC region is from 2.0 to 3.0 volts with a power of 2.4. The charge carrier mobility derived from the SCLC region is 2.2 cm^2/Vs . When ITO is used as the cathode, a charge carrier mobility of 0.5 cm^2/Vs is obtained. The Fermi level of Ag (4.2 eV) is closer to the LUMO level (3.6 eV) of the material than ITO (4.5 eV), thus electron injection from Ag into the LUMO of the material is expected to be more efficient than from ITO. The current for the device with Ag as the cathode is higher than that for the device with ITO as the cathode under same applied voltage. Thereby, the effective mobility derived for the device with Ag as the cathode is larger than that for the device with ITO as the cathode. Also noticeably, the energy barrier for hole injection from the anode (ITO, 4.5 eV) into the HOMO level (6.3 eV) of the material is significantly larger than that for electron injection from the cathode (Ag or ITO) into the LUMO level (3.6 eV) of the material. Hence the majority of the charge carriers injected into and transported through the material are most likely electrons. In addition, perylene diimides have been shown to function primarily as electron-transport materials, as demonstrated by transistor studies of other similar perylene diimides in which no hole mobility could be observed.^{8a}

For **PDI1**, the highest charge carrier mobility found in (+)ITO/**PDI1** (5 μm)/ITO(-) is $0.2 \text{ cm}^2/\text{Vs}$. It is also found that the charge carrier mobility is highly dependent on the morphology of the thin films resulting from the details in the sample preparation process. As shown in Figure 2.7, for the two devices of **PDI1** with the same geometry (+)ITO/**PDI2** (5 μm)/ITO(-), the J - V curve for sample 1 is much higher and, thus a much higher charge carrier mobility ($0.2 \text{ cm}^2/\text{Vs}$) is observed than for sample 2 ($\mu < 10^{-4} \text{ cm}^2/\text{Vs}$). Sample 1 displays a texture consistent with the material being in the columnar mesophase, thus a reasonably high charge carrier mobility. The observed low charge carrier mobility in sample 2 suggests that the material in sample 2 possibly has a lower molecular order, given that the texture is not a typical columnar mesophase texture and both homeotropic and homogeneous alignment can be excluded because of the bright red image of the thin film when observed between two crossed polarizers. The difference in the morphology of the two samples may stem from small differences in the material processing and device fabrication process, such as the melting temperature, cooling rate and shear applied. It is expected that realization of homeotropic alignment of discotic liquid crystals would greatly improve both the reproducibility from device to device and the charge carrier mobility.

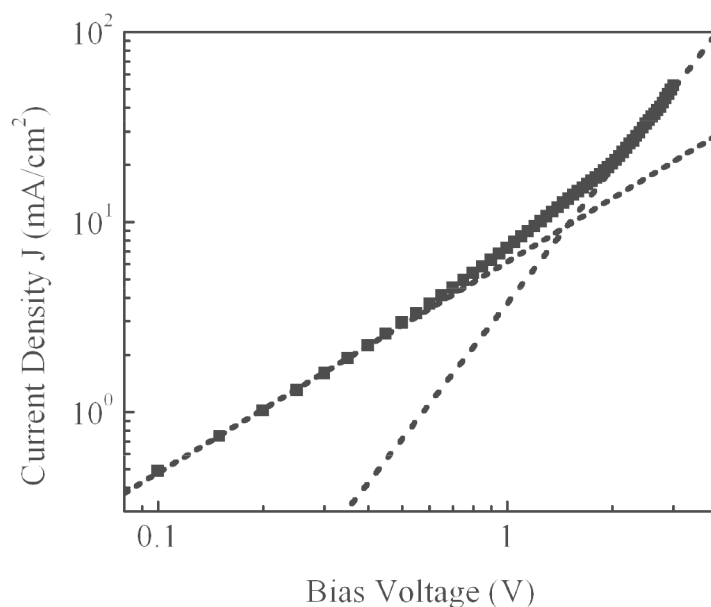


Figure 2.6 Double logarithmic plot of the current density (J) vs. applied voltage (V) for **PDI2** in the device: (+)ITO/**PDI2** ($5\ \mu\text{m}$)/Ag(-).

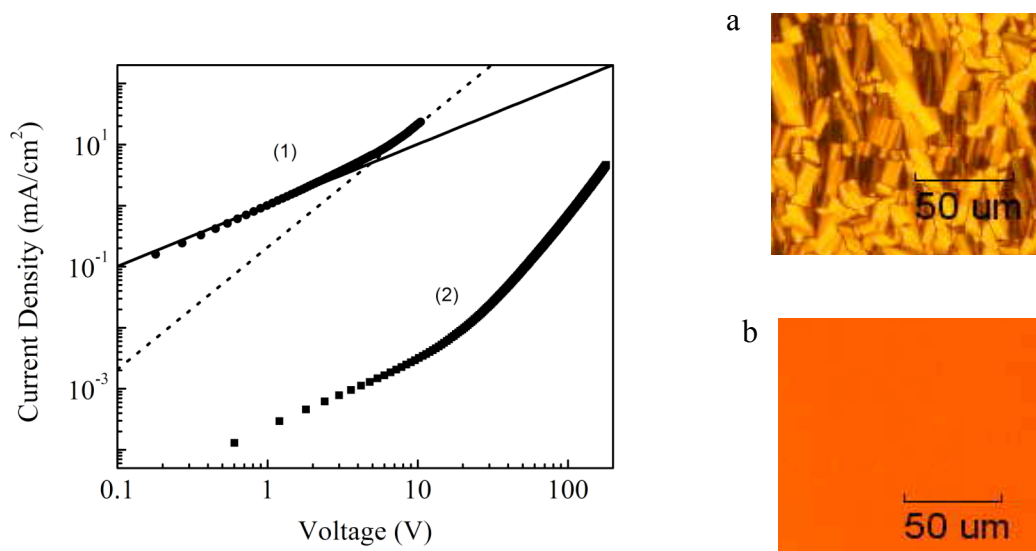


Figure 2.7 (left) Double logarithmic plot of the current density (J) vs. applied voltage (V) measured in two different samples of **PDI1**. The thickness of both samples (1) and (2) was $5\ \mu\text{m}$; full line and dashed line for sample (1) show linear and nearly quadratic power laws of the current density as a function of applied voltage respectively. (right) Photograph (a) of sample (1) and (b) of sample (2) obtained by polarized microscopy.

2.7 Concluding remarks

Charge carrier mobilities, as high as $2.2 \text{ cm}^2/\text{Vs}$, in a columnar discotic perylene diimide liquid crystal (**PDI2**) have been derived from the J - V curves in the SCLC régime under ambient conditions (Table 2.3). These charge carrier mobilities, which we assign as being predominately electron mobilities, are higher than that in amorphous silicon ($0.1 - 1 \text{ cm}^2/\text{Vs}$).²⁴ It is worth noting that these charge carrier mobilities are measured in the liquid crystalline phase of the materials at room temperature without any specific efforts to control the alignment of the discs. The presence of multiple liquid crystalline domains rather than homeotropic mono-domain may lower the effective charge carrier mobilities in these samples due to the high barrier for charge carrier hopping at domain boundaries and to the non-uniform alignment of the columns that ideally would span perpendicularly between the electrodes in the SLCL geometry. In addition, the fact that the use of different cathodes can lead to different J - V curves and therefore the derived charge carrier mobilities suggests that the contact between the materials and the electrodes are not ohmic.²⁵ As a result, the observed SCLC is charge-injection limited and consequently the derived charge carrier mobilities may represent the lower limits of the charge carrier mobilities in these materials by assuming ohmic contact and trap-free as described in the SCLC section in Chapter 1. Base on these considerations, the “intrinsic” charge carrier mobilities in these materials could be higher than have been determined here. Therefore, it would be of great value to find ways to make ohmic contact between the electrodes and the **PDIs** and to control the uniform alignment of the discotic liquid crystals. In addition, although the solid-state absorption suggests that these two materials form J -aggregates in solid state, experimental data that can provide detailed insight into the orientation and the displacement of neighboring discs has yet to be obtained. However, the SCLC

measurements undoubtedly demonstrate that these materials are among the discotic liquid crystals with high charge carrier mobilities.²⁶

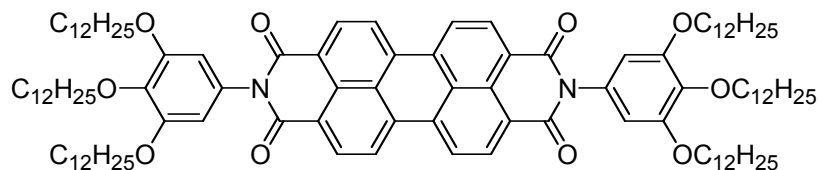
Table 2.3 Summary of the SCLC characteristics of perylene diimide liquid crystals

	Device geometry	μ_0 (cm ² /Vs)	γ (cm/V) ^{0.5}	μ_{max} (cm ² /Vs)
PDI1	(+)ITO/ PDI1 (5 μ m)/ITO(-)	0.2	2.7×10^{-4}	0.2 at 10.5 V
PDI2	(+)ITO/ PDI2 (5 μ m)/ITO(-)	0.4	3.8×10^{-3}	0.5 at 3 V
PDI2	(+)ITO/ PDI2 (5 μ m)/Ag(-)	0.9	1.2×10^{-2}	2.2 at 3 V

2.8 Experimental

General: All chemicals were purchased from Aldrich, Acros Organics, Alfa Aesar or Lancaster and were used without further purification. The ¹H and ¹³C NMR spectra were taken on Varian 300 MHz or Bruker 500 MHz spectrometer using tetramethylsilane (TMS; $\delta = 0$ ppm) as an internal standard. EI and FAB mass spectra were obtained on a VG 70SE spectrometer and MALDI mass spectra were obtained on an Applied Biosystems 4700 Proteomics Analyzer. Flash column chromatography was performed on silica gel (32-63 μ m, 60 Å, Sorbent Technologies). Elemental analyses were carried out by Atlantic Microlabs using a LECO 932 CHNS elemental analyzer. UV-Vis absorption spectra were recorded on a Varian Cary 5E UV-Vis-NIR spectrophotometer using photospectroscopic grade solvents. Extinction coefficients were measured on three solutions with concentration in the range of 10⁻⁶ to 10⁻⁴ M prepared on three samples with different masses. Thin films for solid-state absorption were prepared by drop-casting method from chloroform solution onto quartz slides. Electrochemical measurements

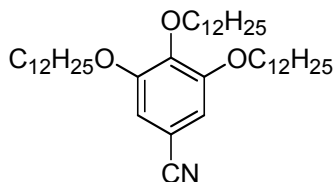
were performed under nitrogen on deoxygenated solutions of tetra-*n*-butylammonium hexafluorophosphate (0.1 M) in methylene chloride with ferrocene as an internal standard using a computer-controlled BAS 100B electrochemical analyzer, a glassy-carbon working electrode, a platinum-wire auxiliary electrode, and a Ag wire anodized with AgCl as a pseudo-reference electrode. Potentials were referenced to the ferrocenium/ferrocene (Fc^+/Fc) couple. DSC traces were taken on a Mettler Toledo DSC 822e instrument at 10 °C/min. XRD data was collected on a Scintag X1 diffractometer with a Cu $K\alpha$ source ($\lambda = 1.5406 \text{ \AA}$) in a continuous scan mode with a step size of 0.02 degree. Optical textures were obtained using an Olympus BX51 microscope equipped with an Olympus U-TU1 X digital camera and an Instec STC200 hot stage. SCLC measurements were performed by measuring the steady-state current-voltage characteristics with a Keithley 2400 source meter on samples prepared by cooling the isotropic liquid of the materials between two glass-supported electrodes and the thickness of the samples was controlled by calibrated glass spacers.



Synthesis of *N,N*-bis[3,4,5-tri(dodecyloxy)phenyl]-3,4,9,10-tetracarboxylic diimide (PDI1)

A mixture of perylene dianhydride (10.9 g, 27.8 mmol), tri(dodecyloxy)phenyl amine (37.9 g, 58.7 mmol) and $\text{Zn}(\text{OAc})_2$ (5.0 g, 27.2 mmol) in quinoline (400 mL) was heated at 180 °C under N_2 for 5 h. After cooling to room temperature, methanol (200 mL)

was added. The mixture was left in refrigerator (- 10 °C) overnight and the resulting precipitate was isolated by filtration and washed with methanol. The red solid was purified by column chromatography eluting with chloroform. After removal of solvent, 33.5 g (78%) of a red solid was obtained. ¹H NMR (500 MHz, CDCl₃): δ (ppm): 8.44 (d, *J* = 8.0 Hz, 4H), 7.99 (d, *J* = 7.0 Hz, 4H), 6.65 (s, 4H), 4.01 (t, *J* = 6.5 Hz, 4H), 3.81 (t, *J* = 6.5 Hz, 8H), 1.80 (m, 4H), 1.70 (m, 8H), 1.52 (m, 4H), 1.36 – 1.21 (m, 104H), 0.88 (t, *J* = 6.5 Hz, 6H), 0.83 (t, *J* = 7.0 Hz, 12H). ¹³C NMR (125 MHz, CDCl₃): 162.9, 153.7, 138.1, 133.6, 130.9, 129.7, 128.4, 125.3, 123.2, 122.7, 106.9, 73.4, 69.1, 31.98, 31.93, 30.55, 29.89, 29.86, 29.77, 29.72, 29.56, 29.45, 29.40, 26.27, 26.11, 22.72, 22.67, 14.12, 14.08. (Eight aliphatic carbon resonances were not observed presumably due to near equivalencies leading to overlap of resonances). Elemental analysis: calcd. for C₁₀₈H₁₆₂N₂O₁₀, C 78.69, H 9.91, N 1.70; found C 78.63, H 10.00, N 1.74.

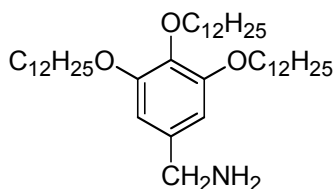


Synthesis of 3,4,5-tri(dodecyloxy)-benzonitrile

To a solution of 3,4,5-tri(methoxy)benzonitrile (4.88 g, 25.25 mmol) in dry dichloromethane (30 mL) cooled at -78 °C under nitrogen, was added a solution of boron tribromide (9.3 mL, 98.34 mmol) in dry dichloromethane (10 mL) dropwise. The reaction was slowly warmed to room temperature and stirred overnight. Then the reaction was cooled to -78 °C again, and ice water (40 mL) was added dropwise carefully. The mixture was stirred at room temperature for 2 h, then was extracted with ethyl acetate,

and the organic solution was dried over anhydrous magnesium sulfate and was filtered. The solvent was removed and slightly yellow solid was obtained.

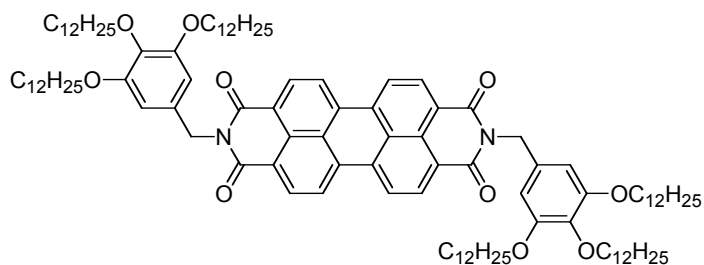
The solid obtained above was dissolved in DMF (100 mL), to which potassium carbonate (13.2 g, 95.51 mmol) and bromododecane (22.15 g, 88.89 mmol) were added. The reaction was heated at 100 °C for 42 h. After cooling to room temperature, water (100 mL) was added and the mixture was extracted with dichloromethane. The organic solution was dried over anhydrous magnesium sulfate and was filtered. The solvent was removed and the residue was recrystallized from acetone. 13.84 g (84%) of a white solid was obtained. ¹H NMR (500 MHz, CDCl₃): δ (ppm): 6.79 (s, 2H), 3.98 (t, *J* = 6.5 Hz, 2H), 3.94 (t, *J* = 6.5 Hz, 4H), 1.78 (m, 4H), 1.71 (m, 2H), 1.44 (m, 6H), 1.27 (m, 48H), 0.86 (t, *J* = 7.0 Hz, 9H). ¹³C NMR (125 MHz, CDCl₃): δ (ppm): 153.4, 142.5, 119.3, 110.4, 106.1, 73.7, 69.4, 31.9, 30.3, 29.73, 29.70, 29.68, 29.65, 29.60, 29.52, 29.38, 29.35, 29.33, 29.2, 26.0, 22.7, 14.1. HRMS (EI): calcd. for C₄₃H₇₇NO₃ m/z: 655.5904; found 655.5925. Elemental analysis: calcd. for C₄₃H₇₇NO₃, C 78.72, H 11.83, N 2.13; found C 78.90, H 11.96, N 2.18.



Synthesis of 3,4,5-tri(dodecyloxy)-benzylamine

To a suspension of LiAlH₄ (1.57 g, 42.37 mmol) in dry THF (100 mL), was added 3,4,5-tri(dodecyloxy)benzonitrile (12.43 g, 18.95 mmol) solution in dry THF (200 mL) at 0 °C. The reaction mixture was warmed to room temperature and was then heated to reflux for 2 h. After cooling to room temperature, the reaction mixture was cooled again to 0 °C, ice water (40 mL) was added dropwise followed by addition of 20% NaOH

solution (40 mL). The mixture was extracted with ethyl acetate. The organic solution was washed with brine and was then dried over anhydrous magnesium sulfate. The solution was filtered and the solvent was removed. The residue was recrystallized from acetone and 11.23 g (90%) of a white solid was obtained. ^1H NMR (500 MHz, C_6D_6): δ (ppm): 7.08 (s, 2H), 4.21 (t, $J = 6.5$ Hz, 2H), 3.67 (t, $J = 6.5$ Hz, 4H), 1.87 (m, 2H), 1.63 (m, 6H), 1.37 (m, 56H), 0.92 (t, 9H). ^{13}C NMR (125 MHz, C_6D_6): δ (ppm): 190.4, 154.1, 144.4, 132.3, 108.1, 73.6, 69.1, 32.33, 32.32, 30.96, 30.22, 30.20, 30.19, 30.15, 30.12, 30.08, 30.02, 29.83, 29.82, 29.79, 29.66, 26.6, 26.5, 23.1, 14.3. HRMS (EI): calcd. for $\text{C}_{43}\text{H}_{81}\text{NO}_3$ m/z : 659.6216; found 659.6209.



Synthesis of *N,N*-bis[3,4,5-tri(dodecyloxy)benzyl]-3,4,9,10-tetracarboxylic diimide (PDI2)

A mixture of 3,4,5-tri(dodecyloxy)-benzylamine (11.12 g, 16.85 mmol), perylene tetracarboxylic dianhydride (3.0 g, 7.5 mmol), $\text{Zn}(\text{OAc})_2$ (0.81 g, 4.4 mmol) and imidazole (50 g) was heated at 150 °C under argon for 12 h. After cooling to room temperature, ethanol was added and the resulting precipitate was filtered. The solid was washed with ethanol and was dissolved in dichloromethane. The solution was washed with 2 N HCl solution twice and was dried over anhydrous magnesium sulfate. The solvent was removed and the residue was purified by column chromatography eluting with chloroform. 11.6 g (92%) of the title compound was obtained as red solid. ^1H NMR (500 MHz, CDCl_3): δ (ppm): 8.58 (d, $J = 8.0$ Hz, 4H), 8.44 (d, $J = 8.0$ Hz, 4H), 6.83 (s,

4H), 5.27 (s, 4H), 3.98 (t, $J = 6.2$ Hz, 8H), 3.88 (t, $J = 6.2$ Hz, 8H), 1.76 (m, 8H), 1.67 (m, 4H), 1.42 (m, 12H), 1.22 (m, 96H), 0.85 (m, 18H). ^{13}C NMR (125 MHz, CDCl_3): δ (ppm): 163.3, 153.0, 137.9, 134.6, 132.0, 131.5, 129.2, 126.3, 123.3, 123.0, 108.2, 73.4, 69.2, 43.9, 31.9, 30.3, 29.72, 29.71, 29.67, 29.61, 29.47, 29.45, 29.37, 26.1, 22.7, 14.1. (Ten carbon resonances were not observed presumably due to near equivalencies leading to overlap of resonances). HRMS (MALDI): calcd. for $\text{C}_{110}\text{H}_{166}\text{N}_2\text{O}_{10}$, m/z : 1675.2537; found: 1675.2556. Elemental Analysis: calcd. for $\text{C}_{110}\text{H}_{166}\text{N}_2\text{O}_{10}$, C 78.81, H 9.98, N 1.67; found C 78.66, H 10.06, N 1.70.

2.9 References

1. Newman, C. R.; Frisbie, C. D.; da Silva Filho, D. A.; Brédas, J.-L.; Ewbank, P. C.; Mann, K. R. *Chem. Mater.* **2004**, *16*, 4436-4451.
2. (a) de Leeuw, D. M.; Simenon, M. M. J.; Brown, A. R.; Einerhand, R. E. F. *Synth. Met.* **1997**, *87*, 53. (b) Katz, H. E.; Johnson, J.; Lovinger, A. J.; Li, W. *J. Am. Chem. Soc.* **2000**, *122*, 7787-7792. (c) Chesterfield, R. J.; McKeen, J. C.; Newman, C. R.; Ewbank, P. C.; Miller, L. L.; Mann, K. R.; Frisbie, C. D. *J. Appl. Phys.* **2004**, *95*, 6396-6405.
3. Würthner, F. *Chem. Comm.* **2004**, 1564-1579
4. (a) Muthukumar, K.; Loewe, R. S.; Kirmaier, C.; Hindin, E.; Schwartz, J. K.; Sazanovich, I. V.; Diers, J. R.; Bocian, D. F.; Holten, D.; Lindsey, J. S. *J. Phys. Chem. B*, **2003**, *107*, 3431 (b) van der Boom, T.; Hayes, R. T.; Zhao, Y.; Bushard, P. J.; Weiss, E. A.; Wasielewski, M. R. *J. Am. Chem. Soc.* **2002**, *124*, 9582 (c) Peeters, E.; van Hal, P. A.; Meskers, S. C. J.; Janssen, R. A. J.; Meijer, E. W. *Chem. Eur. J.* **2002**, *8*, 4470-4474 (d) Schenning, A. P. H. J.; herrikhuyzen, J.; Jonkheijm, P.; Chen, Z.; Würthner, F.; Meijer, E. W. *J. Am. Chem. Soc.* **2002**, *124*, 10252-10253.
5. (a) Iverson, I. K.; Tam-Chang, S.-W. *J. Am. Chem. Soc.* **1999**, *121*, 5801-5802 (b) Liu, S.-G.; Sui, G.; Cormier, R. A.; Leblanc, R. M.; Gregg, B. A. *J. Phys. Chem. B* **2002**, *106*, 1307-1315 (c) Würthner, F.; Thalacker, C.; Diele, S.; Tschierske, C. *Chem. Eur. J.* **2001**, *7*, 2245-2253.
6. Struijk, C. W.; Sieval, A. B.; Dakhorst, J. E. J.; Dijk, M.; Kimkes, P.; Koehorst, R. B. M.; Donker, H.; Schaafsma, T. J.; Picken, S. J.; Craats, A. M.; Warman, J. M.; Zuilhof, H.; Sudhölter, E. J. R. *J. Am. Chem. Soc.* **2000**, *122*, 11057-11066.
7. Chen, Z.; Debije, M. G.; Debaerdemaeker, T.; Osswald, P.; Würthner, F. *Chem. Phys. Chem.* **2004**, *5*, 137-140.
8. (a) Chesterfield, R. J.; McKeen, J. C.; Newman, C. R.; Ewbank, P. C.; da Silva Filho, D. A.; Brédas, J.-L.; Miller, L. L.; Mann, K. R.; Frisbie, C. D. *J. Phys. Chem. B*, **2004**, *108*, 19281-19292. (b) Malenfant, P. R. L.; Dimitrakopoulos, C. D.; Gelorme, J. D.; Kosbar, L. L.; Graham, T. O.; Curioni, A.; Andreoni, W. *Appl. Phys. Lett.* **2002**, *80*, 2517-2519.
9. (a) Adam, D.; Schuhmacher, P.; Simmerer, J.; Häussling, L.; Siemensmeyer, K.; Eitzbach, K. H.; Ringsdorf, H.; Haarer, D. *Nature*, **1994**, *371*, 141-143. (b) van de Craats, A. M.; Warman, J. M.; Müllen, K.; Geerts, Y.; Brand, J. D. *Adv. Mater.*

- 1998**, *10*, 36-38. (c) Palenberg, M. A.; Silbey, R. J.; Malagoli, M.; Brédas, J.-L. *J. Chem. Phys.* **2000**, *112*, 1541-1546.
10. van Herrikhuyzen, J.; Syamakumari, A.; Schenning, A. P. H. J.; Meijer, E. W. *J. Am. Chem. Soc.* **2004**, *126*, 10021-10027.
 11. Langhals, H.; Demmig, S.; Huber, H. *Spectrochim. Acta* **1988**, *44A*, 1189
 12. Shi, M.; Chen, H.; Sun, J.; Ye, J.; Wang, M. *Chem. Comm.* **2003**, 1710
 13. Gvishi, R.; Reisfeld, R.; Burshtein, Z. *Chem. Phys. Lett.* **1993**, *213*, 338
 14. Boni, L. D.; Constantino, C. J. L.; Misogutim, L.; Aroca, R. F.; Zilio, S. C.; Mendonca, C. R. *Chem. Phys. Lett.* **2003**, *371*, 744
 15. Davydov, A. S. *Theory of Molecular Excitons*, Plenum, New York, 1971.
 16. Harrison, W. J. *J. Phys. Chem.* **1996**, *100*, 2310-2321.
 17. Zhan, X.; Risko, C.; Amy, F.; Chan, C.; Zhao, W.; Barlow, S.; Kahn, A.; Brédas, J.-L.; Marder, S. R. *J. Am. Chem. Soc.* **2005**, *127*, 9021-9029.
 18. Anderson, J. D.; McDonald, E. M.; Lee, P. A.; Anderson, M. L.; Ritchie, E. L.; Hall, H. K.; Hopkins, T.; Nash, E. A.; Wang, J.; Padias, A.; Thayumanavan, S.; Barlow, S.; Marder, S. R.; Jabbour, G.; Shaheen, S.; Kippelen, B.; Peyghambarian, N.; Wightman, R. M.; Armstrong, N. R. *J. Am. Chem. Soc.* **1998**, *120*, 9646-9655
 19. Cahen, D.; Kahn, A. *Adv. Mater.* **2003**, *15*, 271-277.
 20. (a) Salbeck, J.; Kunkely, H.; Langhals, H.; Saalfrank, R. W.; Daub, J. *Chimia* **1989**, *43*, 6-9. (b) Lee, S. K.; Zu, Y.; Herrmann, A.; Geerts, Y.; Müllen, K.; Bard, A. J. *J. Am. Chem. Soc.* **1999**, *121*, 3513-3520.
 21. Hreha, R. D.; George, C. P.; Haldi, A.; Domercq, B.; Malagoli, M.; Barlow, S.; Brédas, J.-L.; Kippelen, B.; Marder, S. R. *Adv. Func. Mater.* **2003**, *13*, 967-973
 22. Schmidt-Mende, L.; Fechtenkötter, A.; Müllen, K.; Moons, E.; Friend, R. H.; MacKenzie, J. D. *Science*, **2001**, *293*, 1119-1122.
 23. Dierking, I. *Textures of Liquid Crystals*, 2003, Wiley-VCH Verlag, GmbH & Co. KGaA, Weinheim.
 24. Garnier, F.; Horowitz, G.; Peng, X. Z.; Fichou, D. *Synth. Met.* **1991**, *45*, 163-171.
 25. Shen, Y.; Hosseini, A. R.; Wong, M. H.; Malliaras, G. G. *Chem. Phys. Chem.* **2004**, *5*, 16-25.

26. (a) van de Craats, A. M.; Warman, J. M.; Fechtenkötter, A.; Brand, J. D.; Harbison, M. A.; Müllen, K. *Adv. Mater.* **1999**, *11*, 1469-1472. (b) Debije, M.G.; Piris, J.; de Haas, M. P.; Warman, J. M.; Simpson, C. D.; Watson, M. D.; Müllen, K. *J. Am. Chem. Soc.* **2004**, *126*, 4641-4645. (c) van der Craats, A. M.; Warman, J. M.; Hasebe, H.; Naito, R.; Ohta, K. *J. Phys. Chem. B*, **1997**, *101*, 9224-9232.

CHAPTER 3

DISCOTIC LIQUID-CRYSTALLINE CORONENE DIIMIDES AS CHARGE- TRANSPORT MATERIALS

3.1 Introduction

While charge carrier mobilities in organic semiconductors have been steadily increased over the past several years, a general strategy on how to improve the charge carrier mobilities in organic semiconducting materials has yet to be established.¹ Lemaire *et al* have suggested that charge-transport process through π -stacks of discotic liquid crystals is related to the reorganization energy and the intermolecular transfer integral.² This quantum chemical calculation sheds insightful light on the charge-transport process in discotic liquid crystals. However, it still remains a challenging issue when attempting to apply this basic understanding to the design of materials with high charge carrier mobilities, since it is not trivial to determine the reorganization energy experimentally, and the intermolecular transfer integral is not necessarily related to the aromatic core size of discotic liquid crystals due to possible rotational, transverse and longitudinal displacements between neighboring discs.² In 2001, van de Craats and Warman proposed an empirical relationship between the charge carrier mobility along the columns and the core size of discotic liquid crystals:³

$$\sum \mu_{1D} = 3 \exp(-83/n) \text{ [cm}^2\text{/Vs]} \quad (3.1)$$

where $3 \text{ cm}^2\text{/Vs}$, the sheet-to-sheet charge carrier mobility in graphite,⁴ was used as the limiting value for discotic liquid crystals by the authors and n is the total number of

atoms (second row elements C, N, O) constituting the aromatic core. Soon, with the PR-TRMC measurements on a series of discotic mesogens, Debije *et al* demonstrated there is no such relationship between charge carrier mobilities and aromatic core size of disc liquid crystals.⁵ To date, charge carrier mobilities approaching that found in amorphous silicon (0.1-1 cm²/Vs) have been obtained in the mesophase of discotic liquid crystals: 0.46 cm²/Vs in a hexabenzocoronene (HBC) derivative⁶ and 0.71 cm²/Vs in a Lutetium containing phthalocyanine sandwich complex⁷ as measured by PR-TRMC method. However, these charge carrier mobilities are still lower than that in graphite, and it remains unknown whether 3 cm²/Vs is the limiting value for charge carrier mobilities in discotic liquid crystals.

In Chapter 2, charge carrier mobilities up to 2.2 cm²/Vs have been found using SCLC technique under ambient conditions for a perylene diimide liquid crystal, which is already larger than that in amorphous silicon. Although, charge carrier mobility does not necessarily increase with the core size of the discotic liquid crystals,^{2,5} larger aromatic cores can potentially increase the order of the mesophase due to more favorable phase segregation between the planar rigid aromatic core and the flexible side chains, as evidenced from hexabenzocoronene liquid crystals that have substantially higher thermal stability over a wider temperature range than triphenylene liquid crystals.^{6,8} Therefore, we decided to increase the core size of the perylene diimides to the coronene diimides while maintaining the desirable liquid crystalline properties of being room-temperature liquid crystal with a wide temperature mesophase range. Rohr and coworkers developed an efficient synthesis of coronene diimides from 1,7-bis(alkynyl)-substituted perylene diimides under basic conditions.⁹ A charge carrier mobility has only been measured in a coronene *monoimide* derivative (Figure 3.1) with a value of ca. 0.2 cm²/Vs in its liquid

crystalline phase at room temperature by PR-TRMC technique.^{9b} We were interested in exploring other coronene diimide derivatives as charge-transport materials. Firstly, with two imide groups, instead of one imide group, the compounds can be more electron-deficient, which may render the compounds as promising electron transport materials as have been demonstrated that diimides usually function as electron transport materials.¹⁰ Secondly, the sterically bulky 2,6-di(*iso*-propyl)phenyl group in the coronene monoimide, which is twisted out of plane, is replaced by a tri(dodecyloxy)benzyl group to encourage stronger intermolecular interactions between neighboring discs within the same column.

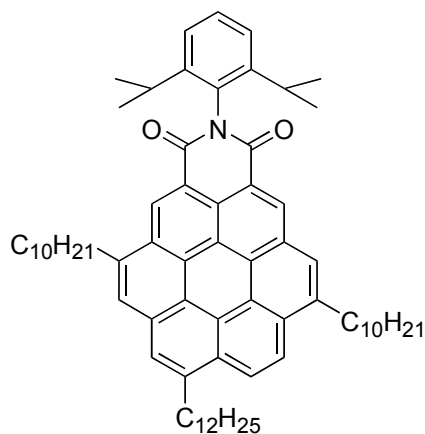
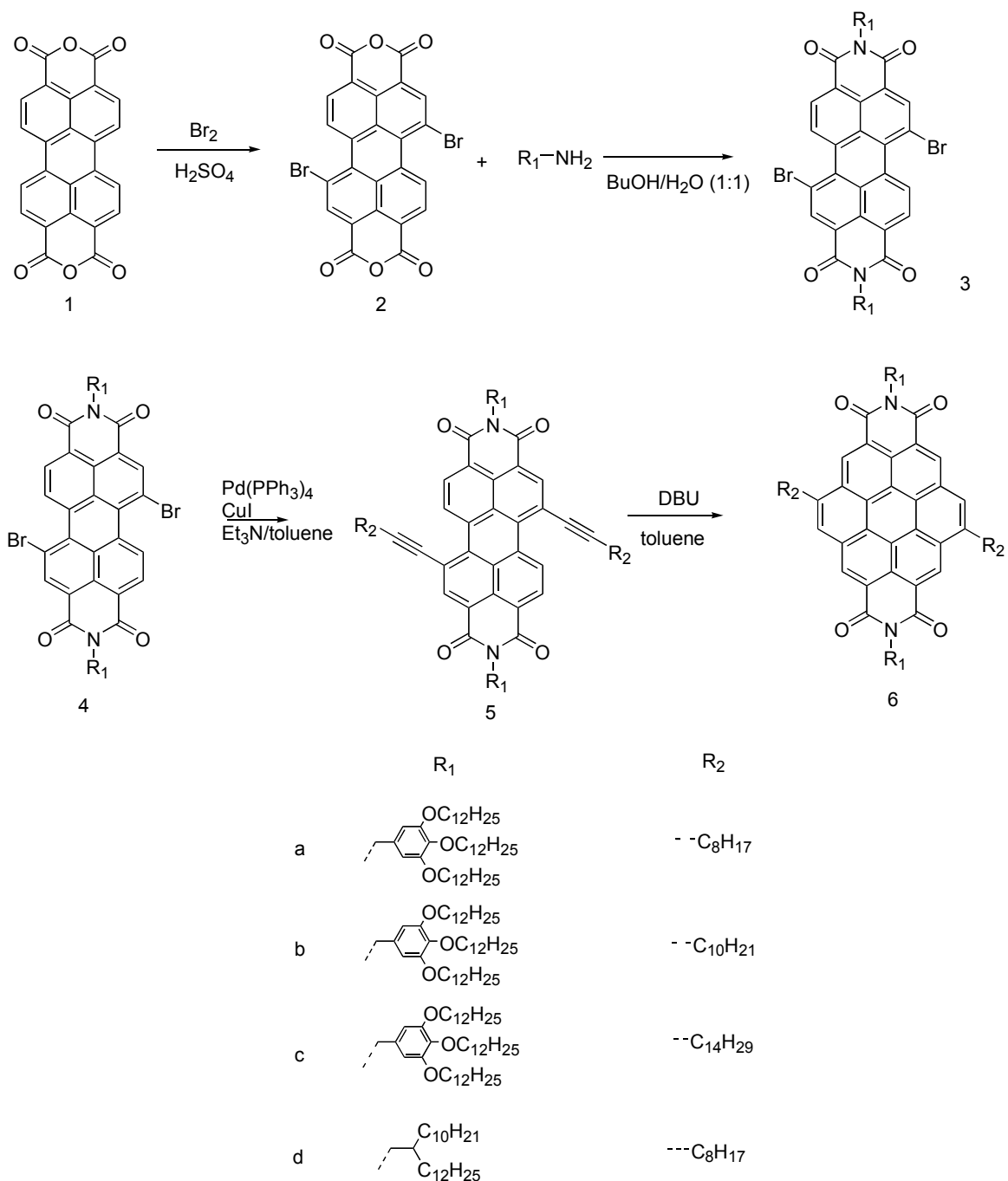


Figure 3.1 Coronene monoimide measured by PR-TRMC technique.

This chapter describes the synthesis, properties of coronene diimide liquid crystals and their SCLC characteristics (by Junsheng Yu, Kippelen group).

3.2 Synthesis

The coronene diimide liquid crystalline materials were synthesized from the 1,7-bis(alkynyl)-substituted-perylene diimides by treatment with a non-nucleophilic base 1,8-diazabicyclo[5.4.0]undec-7-ene (DBU), using the reaction developed by Rohr *et al*⁹ (Scheme 3.1). Bromination of perylene dianhydride in concentrated sulfuric acid provided the 1,7-bisbromoperylene dianhydride,¹¹ which was then condensed with various primary amines to yield the 1,7-bisbromoperylene diimides. Subsequent cross-coupling reactions between the 1,7-bisbromoperylene diimides and terminal acetylenes gave the 1,7-bis(alkynyl)-substituted-perylene diimides which were then cyclized to generate the coronene diimides under basic conditions.



Scheme 3.1 Synthesis of coronene diimides **6a - d**.

Depending upon the reaction conditions, bromination of perylene dianhydride in concentrated sulfuric acid can give 1,6,7-tribromoperylene dianhydride and 1,6-

dibromoperylene dianhydride along with 1,7-dibromoperylene dianhydride as the major product.¹² Subsequent reactions of the brominated perylene dianhydrides leading to soluble diimides enables purification of the 1,7-dibromoperylene diimide, which can be separated from the tribromoperylene diimide by column chromatography and can be further separated from its 1,6-isomer by multiple recrystallizations. It was found the ratio of tribromoperylene diimide, 1,6-dibromoperylene diimide and 1,7-dibromoperylene diimide was 4 : 20 : 76. When synthesizing the coronene diimides, Rohr also noticed the formation of isomers of 1,6- and 1,7-bis(alkynyl)-substituted perylene diimides, with the ratio being 4 : 96.^{9b} We found that the trans/cis isomeric ratio of the coronene diimide was 12 : 88, estimated from ¹H NMR (500 MHz, CDCl₃) (Figure 3.2). From the literature reports and our own experience, the ratio of the two isomers may vary depending upon the reaction conditions of the bromination of perylene dianhydride. Generally, more bromine, higher temperature and longer reaction time tend to produce more 1,6-dibromoperylene dianhydride.

Choosing an appropriate base (usually amines) in the Sonogashira coupling reaction is important to produce the desired product, since different amines may lead to the formation of different products, and sometimes several products can be formed. It was demonstrated that when a secondary amine was used, no desired double-coupled product was produced, but three other compounds were formed (Scheme 3.2).^{9b} The mono or bis amino-substituted compounds were formed by aromatic nucleophilic substitution on the bisbromoperylene diimide derivatives by the secondary amine, and the coronene diimide was probably generated from the bis(alkynyl)-substituted intermediate, which was ring-closed *in situ* in the presence of the amine. Therefore, non-nucleophilic tertiary amines such as triethylamine were suggested as the appropriate amine for the

coupling reaction. However, stronger tertiary amines such as ethyldiisopropyl amine can also lead to direct formation of coronene diimides to some extent in this step from our experience. On the other hand, the *in situ* formation of coronene diimides suggests that the ring-closure step is very efficient, and a two-step one-pot strategy may be employed to simplify the synthesis. For example, coronene diimides **6a** and **6d** were synthesized using such one-pot method.

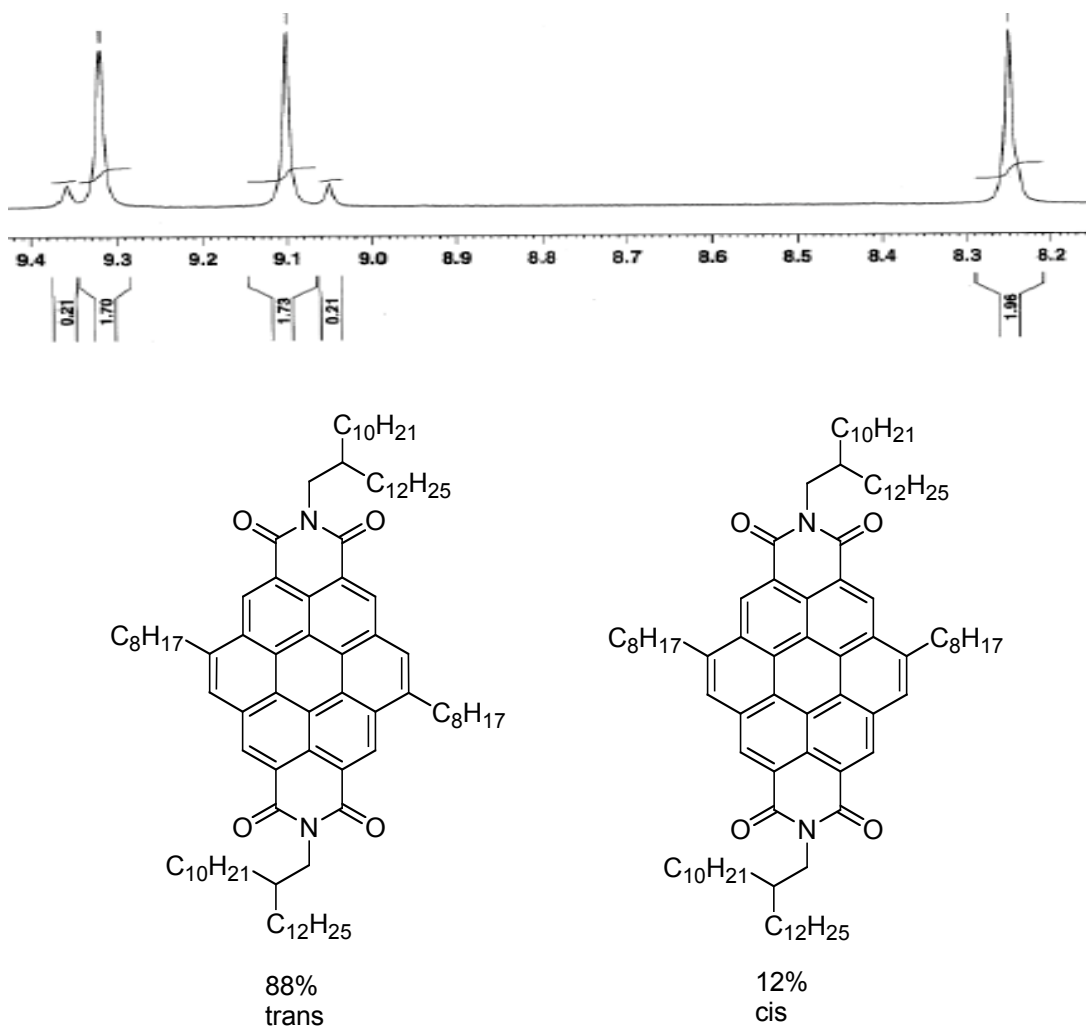
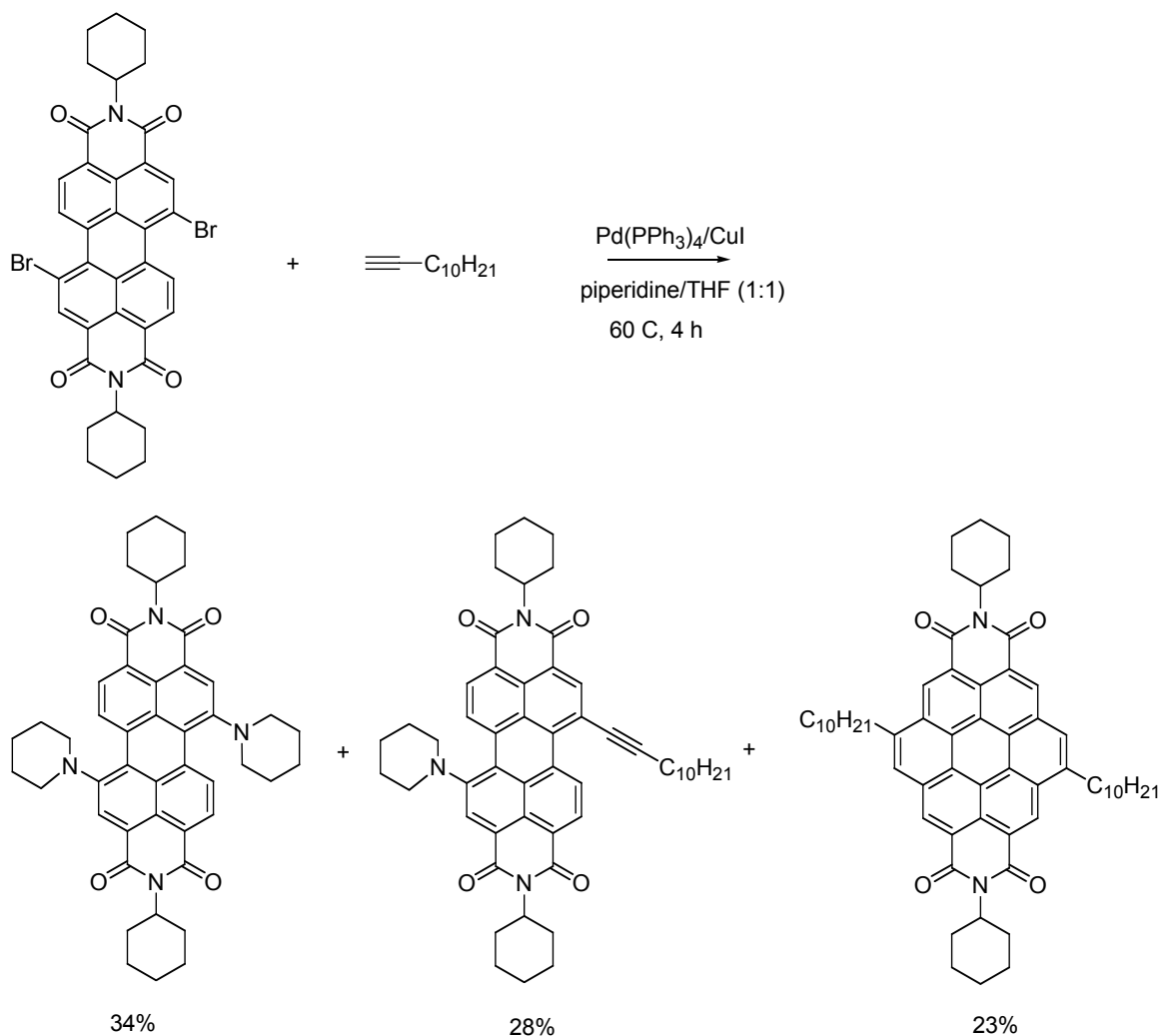


Figure 3.2 Isomeric ratio of coronene diimide based on 500 MHz ^1H NMR



Scheme 3.2 Reaction of dibromo-perylene diimide with acetylene in the presence of a secondary amine. (Ref. 9b)

3.3 Absorption and emission properties

The coronene diimides **6a** - **d** have similar absorption properties. Each exhibits three absorption bands from 300 - 550 nm in methylene chloride (Figure 3.3 and Table 3.1). The two lower energy bands show fine vibronic structures similar to that of perylene diimides and the lowest energy band is less intense. Although coronene diimides have

extended conjugation than perylene diimides, their lowest energy band is blue-shifted by more than 10 nm. Theoretical calculations suggest that coronene diimides can not be regarded as simple analogues of perylene diimides.¹³ The lowest energy transition of perylene diimides is associated with the polarization along the longer molecular axis; while the lowest energy transition of coronene diimides is related to the polarization along the shorter molecular axis and is a partially forbidden transition, resulting in the corresponding blue-shift and weakened absorption intensity.

The Stokes shift of the emission spectra of these coronene diimides is rather small, only 4 nm. They also have distinct vibronic modes as being nice mirror images of their absorption spectra. Compound **6d** has a much higher quantum yield (0.23) than the tri(dodecyloxy)benzyl-substituted compounds **6a - c** (0.01). The relatively low quantum yield of compound **6d** is consistent with the quantum calculation that the lowest energy transition is a partially forbidden transition,¹³ given that the coronene diimides have a very rigid structure (small Stokes shift). The much lower quantum yield of compounds **6a - c** may be attributed to both the forbidden transition and a possible weak charge transfer quenching from the more electron-rich tri(dodecyloxy)benzyl group.

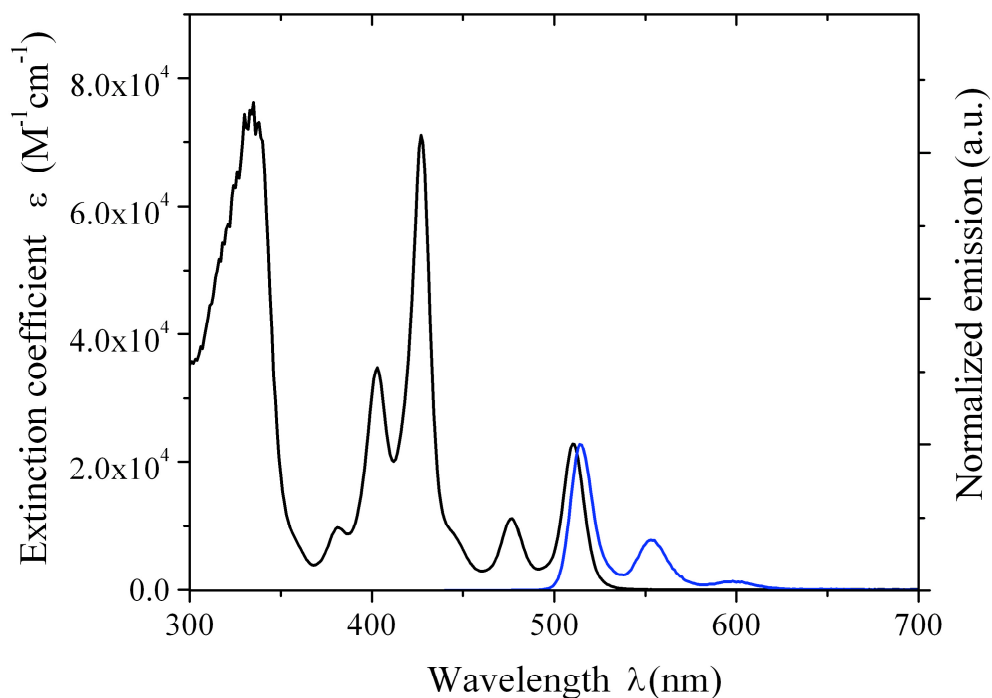


Figure 3.3 Absorption and emission spectra of compound **6d** in dichloromethane. Excitation wavelength is 427 nm.

Table 3.1 Summary of the absorption and emission data of the coronene diimides in dichloromethane.

	Absorption [nm] (extinction coefficient [$M^{-1}cm^{-1}$])	Emission [nm]	Quantum yield*
6a	333 (78600), 383 (9200), 404 (32200), 429 (67500), 478 (13100), 512 (20700)	516, 555	0.01
6b	332 (77800), 384 (8900), 404 (31800), 429 (66600), 478 (11100), 512 (20300)	516, 553	0.01
6c	333 (73200), 384 (8000), 405 (29000), 429 (61100), 478 (9700), 512 (18500)	516, 556	0.01
6d	335 (76200), 382 (9700), 403 (34800), 427 (71000), 477 (11200), 510(22800)	514, 553, 598	0.23

* Excitation wavelength 400 nm with perylene as standard.

3.4 Electrochemical properties

The four coronene diimides show similar electrochemical properties. The cyclic voltammograms (Figure 3.4) display two reversible reductions with the current of the second reduction being almost twice that of the first reduction. The first reduction potential of the coronene diimides is about -1.4 V (*vs.* ferrocenium/ferrocene), which is more negative than that for the perylene diimides by 0.4 V. The second reduction band appears to be a sum of two one-electron reductions occurring almost simultaneously on two positions separated at a reasonably large distance from each other within the molecules. Thus, most likely the first reduction may be somewhat localized on the coronene diimide core and the two one-electron reductions may take place at the two imide positions. However, oxidation of the coronene diimides was not observed within the solvent window (0.1 M Bu_4NPF_6 dichloromethane solution) when applying positive voltage.

Conjugation expansion along the short molecular axis from perylene diimides to coronene diimides can affect the frontier orbital energy levels of the compounds; the LUMO level is raised while the HOMO level is lowered in coronene diimides in comparison to that in perylene diimides.¹³ However, expansion of conjugation along the long molecular axis from perylene diimides to terrylene diimides and quaterrylene diimides raises the HOMO level significantly; while the LUMO level is not affected substantially. The effect of conjugation expansion along the long molecular axis on the frontier orbitals is also supported by similar first reduction potentials of perylene diimide, terrylene diimide and quaterrylene diimide.¹⁴

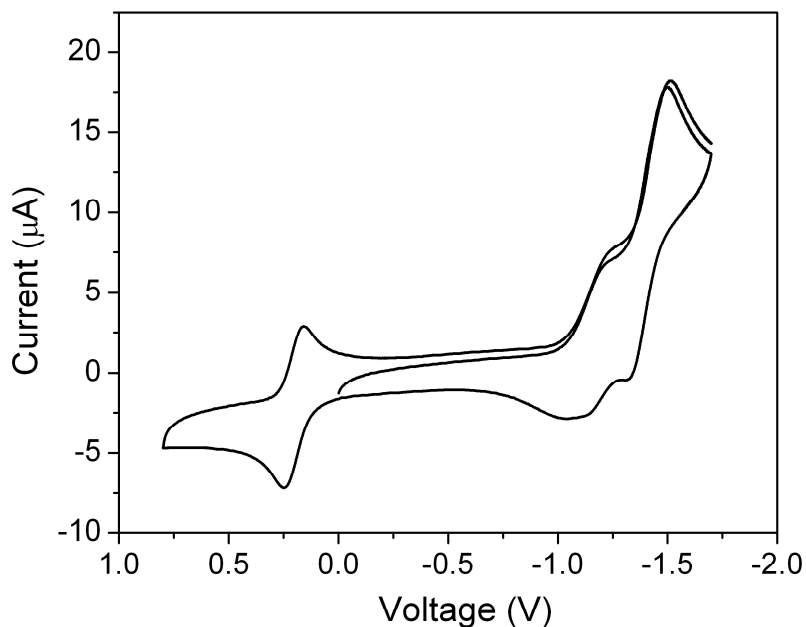


Figure 3.4 Cyclic voltammogram of compound **6a** in 0.1 M Bu₄NPF₆ dichloromethane solution with Fc⁺/Fc (0.5 - 0 V) as internal standard, scan rate = 50 mV/s.

Similarly to the perylene diimides in Chapter 2, here the energy levels of the materials are estimated based on the optical and electrochemical data. The optical energy gap is estimated from the intersection of the absorption and emission spectra, which is ca. 512 - 514 nm and gives an optical energy gap of 2.4 eV. The LUMO level is estimated to be 3.3 eV, similarly estimated as for the perylene diimides by comparing the reduction potential of the coronene diimides with that of Alq₃ with known EA value. Since no oxidation in CV was observed within the solvent window, the HOMO level can not be estimated by comparing the oxidation potential of the coronene diimides with that of TPD with known IP. Thus, the HOMO level is estimated using HOMO = exciton binding energy + (optical energy gap + LUMO) = exciton binding energy + 5.7 eV; therefore, the HOMO level should be lower than 5.7 eV by the amount of the exciton binding energy.

3.5 Aggregation behavior

Aggregation behavior of large aromatic molecules is of great interest in understanding intermolecular interactions, which can then be controlled to obtain desired electronic and optical properties of the materials.¹⁵ Aggregation studies of liquid crystalline materials can provide certain information on the molecular packing of the aromatic discs; furthermore, it can aid in solution processing of the materials for device fabrication as exemplified by the aggregation study of hexabenzocoronene derivatives, the molecular orientation of which can be controlled during solution casting process—zone casting for transistor fabrication.¹⁶

There are several models for studying self-association processes, among which the simplest one is the equal K (EK) model.¹⁷ In the EK model, it is assumed that the constant for each molecule adding to a growing stack is the same and that the molecules within the same stack have the same properties. The fraction of the free molecules at certain concentrations is determined by equation:

$$\alpha = \frac{2KC + 1 - \sqrt{4KC + 1}}{2K^2C^2} \quad (3.2)$$

where K is the formation constant and C is the total concentration of the molecules (free molecules and aggregated molecules).

For UV-Vis study, after combination with Beer's Law, the following can be derived:

$$\varepsilon(C) = \frac{2KC + 1 - \sqrt{4KC + 1}}{2K^2C^2} (\varepsilon_f - \varepsilon_a) + \varepsilon_a \quad (3.3)$$

where $\varepsilon(C)$ is the observed extinction coefficient at certain concentration, ε_f is the extinction coefficient of the free molecules and ε_a is the extinction coefficient of the

aggregated molecules in the stacks. This method has been used to study the solution aggregation behavior of perylene derivatives.¹⁸

The aggregation behavior of the coronene diimides was studied by absorption spectroscopy in low polarity solvent methylcyclohexane (MCH). Upon increasing the concentration, the absorption properties of the coronene diimides experience significant changes with some defined isosbestic points (Figure 3.5). Compared with their absorption spectrum in dichloromethane (Figure 3.3), which can be regarded as the behavior of the free molecules, the spectrum of compound **6b** in MCH shows less resolved vibronic features at low concentrations, and the vibronic features are almost completely lost at high concentrations. At low concentrations, the λ_{max} is at 502 nm, which is gradually shifted bathochromically to 517 nm at high concentrations. Moreover, the spectrum at high concentrations resembles that of the solid-state thin film (Figure 3.6), which displays a new peak at longer wavelength around 517 nm. These marked spectral changes strongly suggest formation of *J*-type aggregates^{15b, 15e, 18a, 19} in MCH at high concentrations as well as in solid state for coronene diimide **6b**.

All of the four coronene diimides show similar aggregation behaviors that are evaluated using equation 3.2 by nonlinear least square regression fitting²⁰ (Figure 3.7). The aggregating ability of the four compounds decreases in the order of **6b**, **6c**, **6a** and **6d**, with aggregation constants of 5.1×10^5 , 2.4×10^5 , 1.9×10^5 and $0.8 \times 10^5 \text{ M}^{-1}$, respectively. Dove-tailed alkyl side chains can lead to higher steric hindrance than other side chains,^{16b} which can be used to explain the lowest aggregation constant found in compound **6d**. For compounds **6a** - **c** with the same imide group, but with different length of the chains attached to the core, their different aggregation ability suggests that there may exist an optimal length for the side chains which may have a subtle balance between

the flexibility of the chain (which is unfavorable for aggregation) and the ability of phase segregation between the side chains and the core (which is favorable for aggregation); both the flexibility and the ability of phase segregation can be a function of the chain length.

The aggregation constant of **PDI2** with the same imide group — tri(dodecyloxy)benzyl group — as in coronene diimides **6a – c** was previously reported to be $1.3 \times 10^4 \text{ M}^{-1}$ in MCH estimated using the same method.^{18c} The aggregation constants for coronene diimides **6a – c** (5.1×10^5 , 2.4×10^5 and $1.9 \times 10^5 \text{ M}^{-1}$, respectively) are higher than that for **PDI2**. The higher aggregation constants for the coronene diimides when compared to the perylene diimide with the same imide group may possibly originate from the larger aromatic core in the coronene diimides, which may lead to stronger intermolecular interaction, though detailed information on the rotational and lateral displacements of the aromatic cores is not readily available. In addition, one should realize that the two additional side chains pending off the core in the coronene diimides also play a role in determining the aggregation constant, though the contribution from these two additional side chains to the larger aggregation constants for the coronene diimides is not understood.

The aggregation constant of **PDI1** with a different imide group — tri(dodecyloxy)phenyl group — was reported to be substantially larger: 10^7 M^{-1} in MCH estimated using the same method.^{18a} The aggregation constant of **PDI1** is about three orders of magnitude larger than that of **PDI2** and more than one order of magnitude larger than that of coronene diimides. The much larger aggregation constant of **PDI1** when compared to **PDI2** was explained by the significantly decreased rigidity of the **PDI2** molecule due to the presence of the flexible $-\text{CH}_2-$ linker between the

tri(dodecyloxy)phenyl side group and the imide nitrogen atom.^{18c} When comparing the aggregation constant of **PDI1** with that for coronene diimides **6a – c**, two variables (different imide groups and different aromatic cores) should be considered. The larger aggregation constant of **PDI1** than that for coronene diimides **6a – c** indicates that the flexibility of the imide group, rather than the size of the aromatic core, plays a predominant role in the aggregation process for these compounds. Since the flexibility of the molecules is expected to be greatly suppressed in solid state compared to that in solution, it is difficult to directly translate the solution behavior of the molecules into the solid-state properties. However, aggregation study is still a meaningful tool to gain certain information on the intermolecular interactions for molecules with the same type of side groups. For example, we can compare compounds with the same type side chains of different lengths.

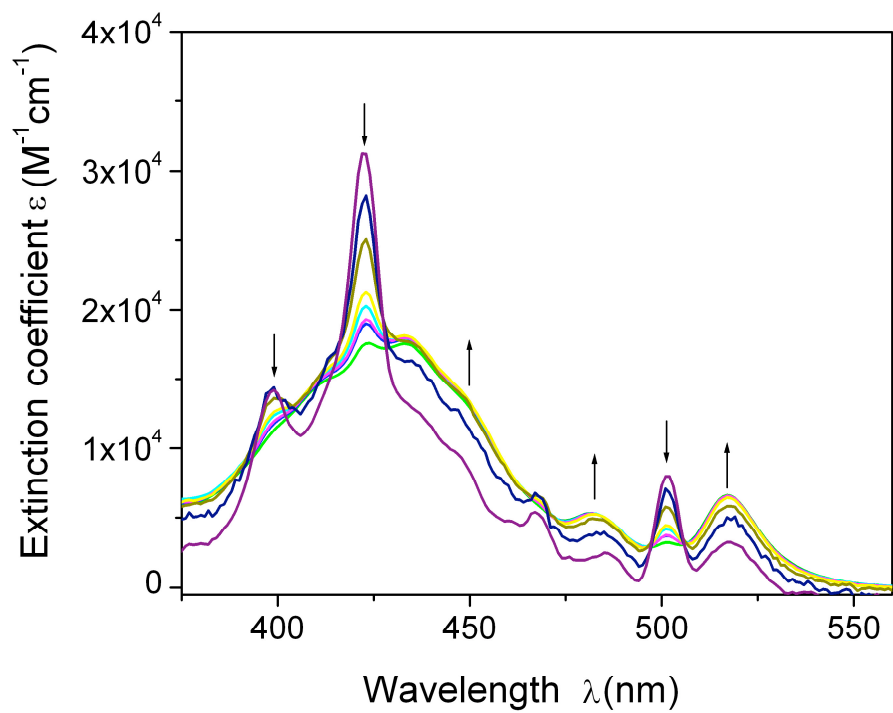


Figure 3.5 Absorption of compound **6b** as a function of the concentration in MCH (concentration range from 2.29×10^{-7} M to 3.57×10^{-5} M).

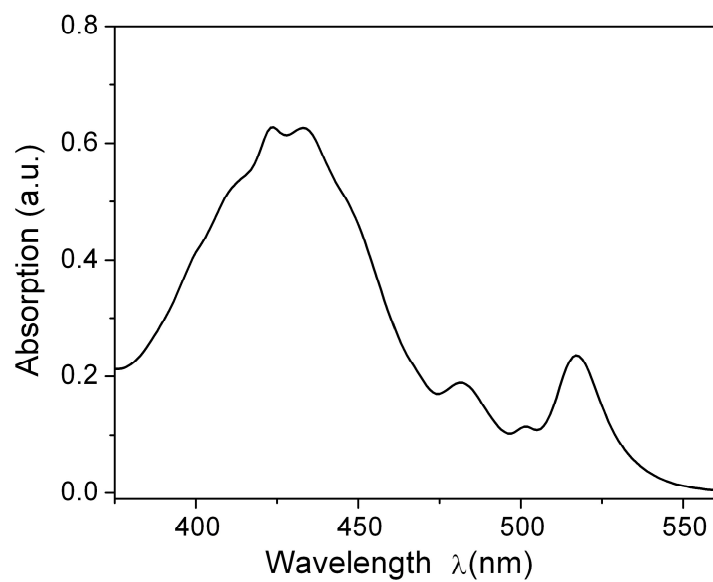


Figure 3.6 Absorption spectrum of a thin film of compound **6b** prepared by drop casting of dichloromethane solution on a quartz slide.

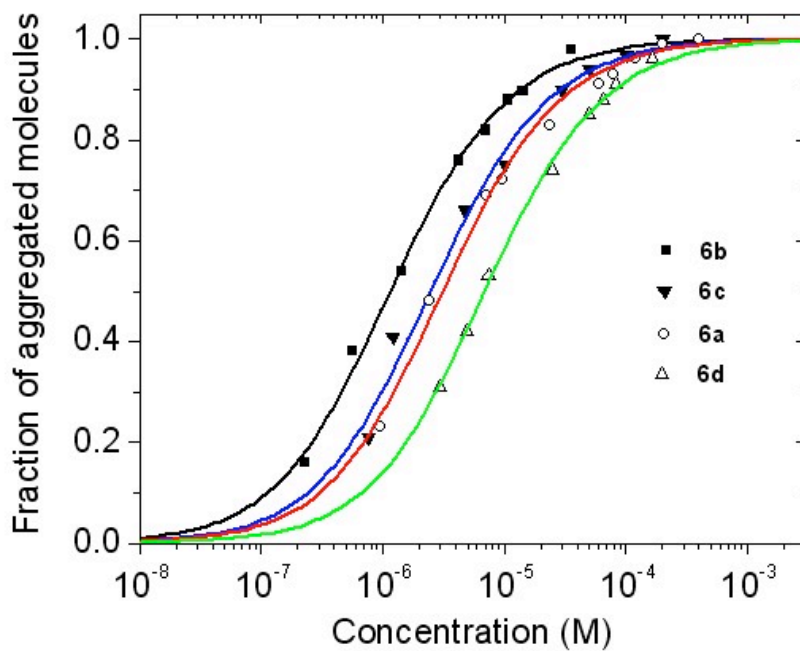


Figure 3.7 Fraction of aggregated molecules as a function of the concentration of coronene diimides in MCH (absorption at 420 nm is used for calculation).

3.6 Liquid crystalline properties

DSC (Figure 3.8) traces show that the coronene diimides form only one phase that exists over a wide temperature range between two thermal transitions. For compounds **6a** - **6c**, the phase transition temperatures are quite similar, and the phases are from ca. room temperature to 180 °C - 190 °C. Interestingly, compound **6d** with the dove-tailed group even displays a phase over a larger temperature range, which occurs approximately from -20 °C to 250 °C. Also noticeably, the phase transition enthalpy is different for these four compounds. The phase transition enthalpy (Table 3.2) associated with the higher temperature transition from the liquid crystalline phase to the isotropic phase decrease in the order of **6c**, **6b**, **6a**, **6d**; the enthalpies for **6c** and **6b** are very close, and the enthalpies for **6c**, **6b**, **6a** are much higher than that for **6d**. As shown in Figure 3.9, after cooling from their isotropic phase to room temperature, compounds **6a**, **6c** and **6d** exhibit focal conic fan textures between two crossed polarizers, typical of hexagonal columnar mesophase. However, the texture of compound **6b** is slightly different which is revealed to form a rectangular mesophase as is evidenced from the XRD as will be discussed next.

Table 3.2 Summary of the phase transition temperature T [°C] and the transition enthalpy ΔH [kJ/mol] of coronene diimides **6a** - **6d** (second heating-cooling cycle).

	Heating		Cooling	
	T [°C] (ΔH [kJ/mol])			
6a	27.4 (17.0)	187.6 (9.6)	179.4 (7.8)	-0.2 (50.8)
6b	15.6 (47.5)	181.8 (11.1)	175.1 (10.6)	8.6 (42.5)
6c	18.7 (62.1)	180.5 (12.0)	174.0 (11.5)	10.5 (69.2)
6d	-13.3 (3.6)	253.8 (5.9)	250.4 (5.9)	-26.1 (7.2)

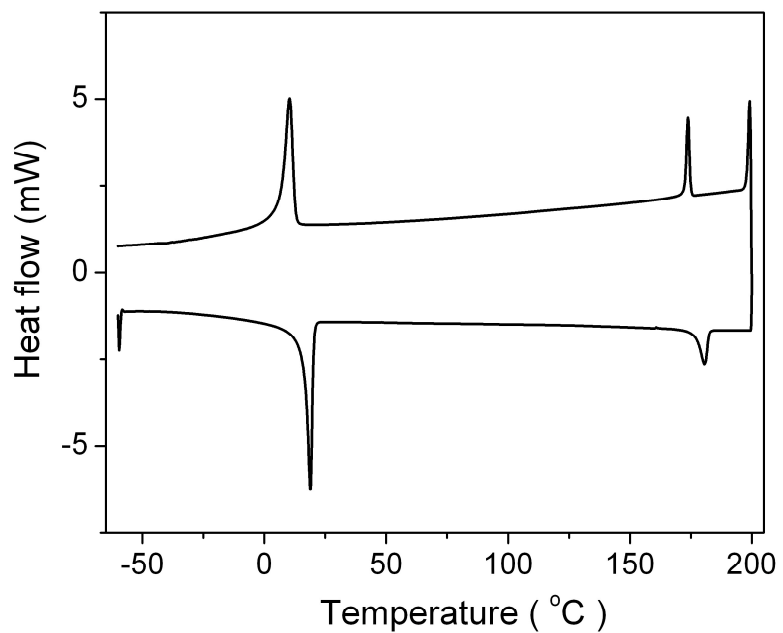


Figure 3.8 DSC (second heating - cooling cycle) of compound **6c**.

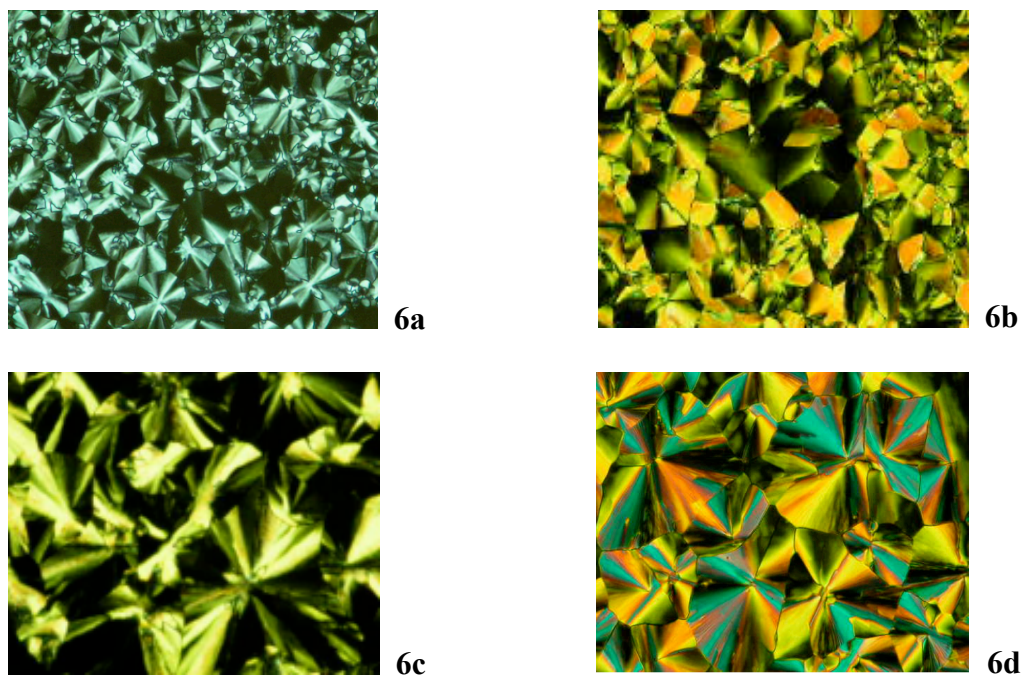


Figure 3.9 Optical textures of coronene diimides **6a - d** between crossed polarizers (magnification 20 ×).

The mesophase structures of the coronene diimides were investigated by XRD (Figure 3.10, Table 3.5). For compounds **6a** - **c** with the same tri(dodecyloxy)benzyl groups, but different alkyl chains with increasing length pending off the core, the number of the well-resolved peaks in the low angle region indicates that the degree of the order of their mesophases decreases from compound **6b** to **6c** to **6a**. Compound **6b** shows six well-resolved diffraction peaks compared to the four peaks for compound **6c** and the two peaks for compound **6a**. For compound **6b**, there are two close peaks at $2\theta \approx 3^\circ$, which may point to a rectangular phase.²¹ Due to the presence of the disc at the center of the rectangle, peaks with odd numbers of $(h+k)$ are systematically missing,²² thus the remaining sharp peaks are indexed to the (02), (40), (22) and (42) peaks with the (31) peak missing. The reciprocal d spacing of the two peaks (100) and (110) of compound **6a** is approximately $d_{100} : d_{110} = 1 : \sqrt{3}$, indicative of a hexagonal columnar mesophase. Similarly, the reciprocal d spacing for the four peaks of compound **6c** is approximately in the ratio of $d_{100} : d_{110} : d_{200} : d_{210} = 1 : \sqrt{3} : 2 : \sqrt{7}$ and the reciprocal d spacing of the three peaks of compound **6d** is in the ratio of $d_{100} : d_{110} : d_{200} = 1 : \sqrt{3} : 2$, consistent with being hexagonal arrangement of the columns. Furthermore, each of the four compounds shows a peak at $2\theta \approx 25^\circ$ following the diffuse peaks ascribed to the side chain halo in the wide-angle region, although this peak for **6d** is much broader. The peak at $2\theta \approx 25^\circ$ is indexed to the (001) peak and the d spacing is approximately 3.5 Å, corresponding to the distance between neighboring aromatic discs within the same column of the mesophases. This distance is comparable to or even smaller than that found in hexabenzocoronene derivatives (3.50 Å for HBC-PhC₁₂ and 3.55 Å for HBC-C₁₂)²³ and a helical triphenylene liquid crystal (3.64 Å)²⁴. Hence, for all of the coronene diimides, a relatively long-range

order can be expected along the columns; compounds **6a** and **6c - d** form ordered hexagonal columnar mesophase (Col_{h0}), while compound **6b** forms ordered rectangular columnar mesophase (Col_{r0}).

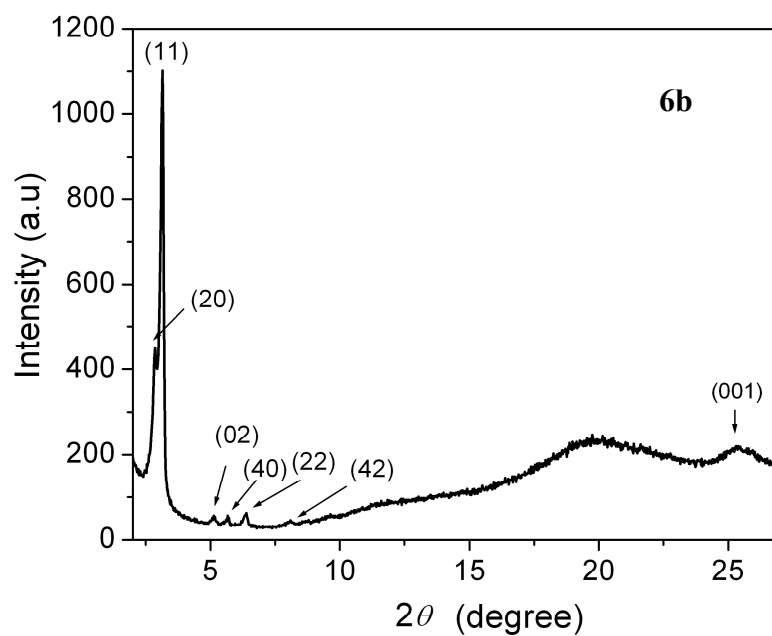
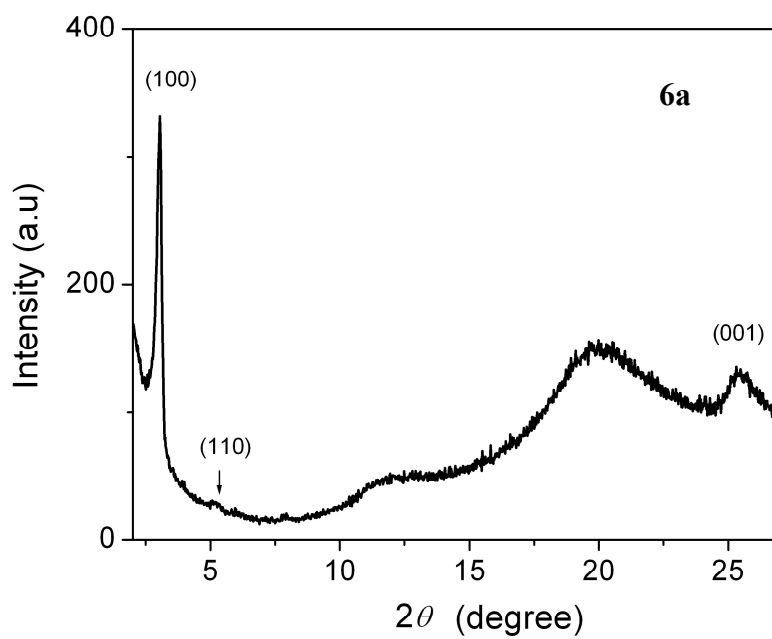


Figure 3.10 XRD of compounds **6a - d** at room temperature after cooling from the isotropic phase.

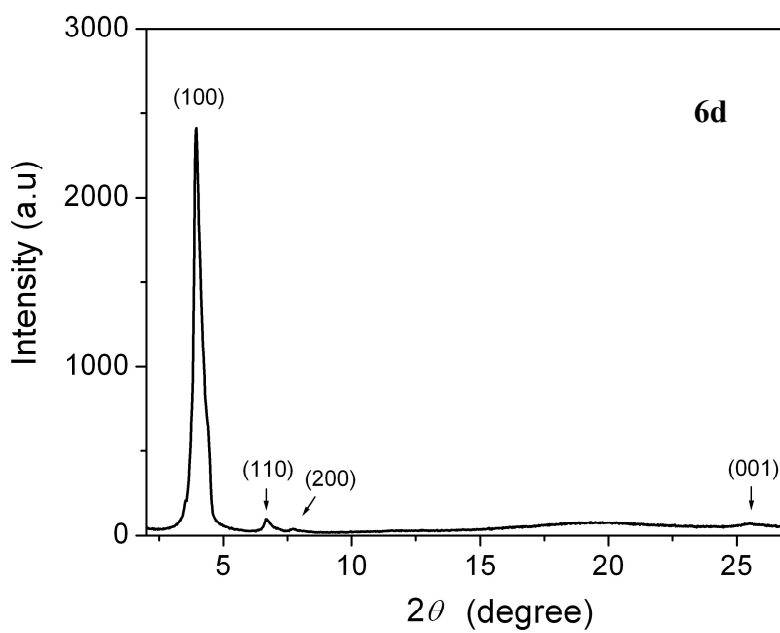
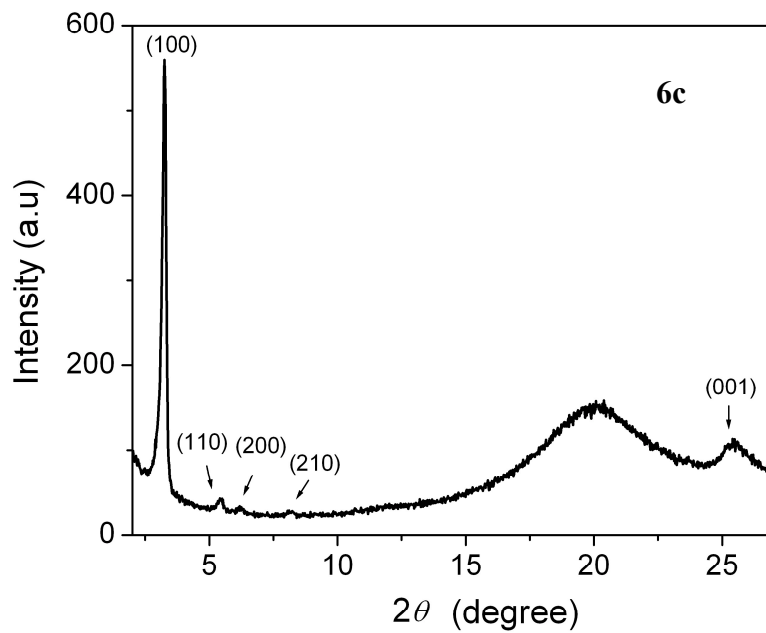


Figure 3.10 (CONT.)

Table 3.3 Summary of the XRD data of compounds **6a - d**.

	(<i>hkl</i>)	2 θ (degree)	<i>d</i> spacing (Å)	Lattice parameter (Å)	Mesophase
6a	(100)	3.05	28.95	$a_0 = 33.4$	Col _{ho}
	(110)	5.09	17.34		
	alkyl halo	20.10	4.41		
	(001)	25.33	3.51		
6b	(200)	2.87	30.78	$a_0 = 61.6$ $b_0 = 34.4$	Col _{ro}
	(110)	3.15	28.03		
	(020)	5.13	17.20		
	(400)	5.68	15.56		
	(220)	6.40	13.80		
	(420)	8.10	10.90		
	alkyl halo	20.16	4.40		
(001)	25.39	3.50			
6c	(100)	3.25	27.14	$a_0 = 31.3$	Col _{ho}
	(110)	5.41	16.31		
	(200)	6.19	14.27		
	(210)	8.23	10.73		
	alkyl halo	20.39	4.35		
(001)	25.41	3.50			
6d	(100)	3.95	22.35	$a_0 = 25.8$	Col _{ho}
	(110)	6.66	13.26		
	(200)	7.74	11.41		
	alkyl halo	19.35	4.58		
	(001)	25.53	3.49		

3.7 SCLC characterization

The J - V characteristics of the coronene diimide liquid crystals were studied under ambient conditions using SCLC technique as described in Chapter 1. For compounds **6a-c**, the J - V characteristics were measured with ITO as the anode and Ag as the cathode in a device structure: (+)ITO/coronene diimide (5 μ m)/Ag(-). A typical J - V curve (**6b**) of the coronene diimides is shown in Figure 3.11. At low voltage (0 - 0.5 V), the J - V is almost

linear in the form of $J \propto V^{1.04}$, thus in the ohmic region; at high voltage (5 – 7.5 V), J - V is almost quadratic in the form of $J \propto V^{2.2}$, thus in the SCLC region. The maximum charge carrier mobility derived from the SCLC region is $3.9 \text{ cm}^2/\text{Vs}$ at an average electric field of $1.5 \times 10^4 \text{ V/cm}$ (applied voltage 7.5 V).

Similarly, mobilities in the other three materials can be obtained (Table 3.6). Based on the estimated energy levels, electron injection from Ag (4.2 eV) into the LUMO level (3.3 eV) of the material is more favored than hole injection from ITO (4.5 eV) into the HOMO level ($> 5.7 \text{ eV}$), therefore, most likely, electron injection process may be the dominant process at the interface and the majority of the charge carriers passing through the material may be electrons. Thus the majority of the charge carrier mobility measured here may represent that for electron. Using lower work function cathodes that can further match the LUMO level may provide more accurate evaluation of the electron mobility of these materials.

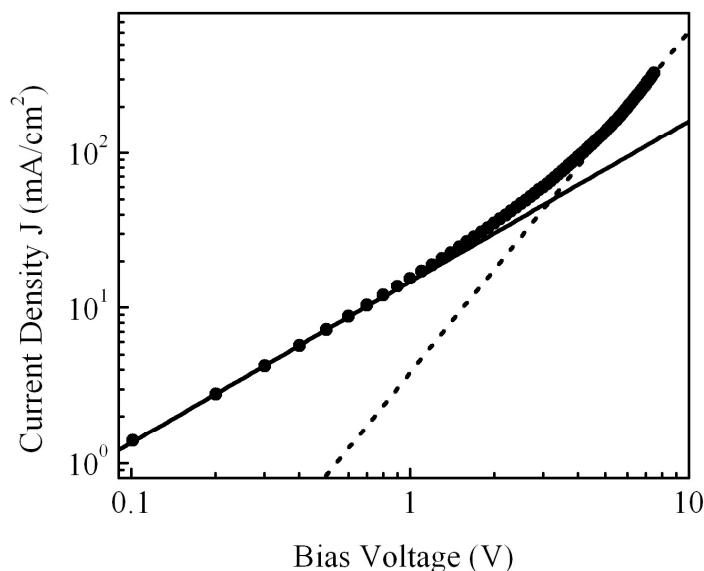


Figure 3.11 Double logarithmic plot of the current density (J) vs applied voltage (V) for compound **6b** in the device: (+)ITO/**6b** (5 μm)/Ag(-).

Table 3.4 Summary of the SCLC characteristics of coronene diimide liquid crystals.

	Device geometry	μ_0 (cm ² /Vs)	γ (cm/V) ^{0.5}	μ_{max} (cm ² /Vs)
6a	(+)ITO/ 6a (5 μ m)/Ag(-)	0.4	1.6×10^{-3}	0.5 at 8 V
6b	(+)ITO/ 6b (5 μ m)/Ag(-)	3.0	2.1×10^{-3}	3.9 at 7.5 V
6c	(+)ITO/ 6c (5 μ m)/Ag(-)	2.0	3.5×10^{-3}	3.1 at 7.5 V
6d	(+)ITO/ 6d (5 μ m)/ITO(-)	1.9×10^{-7}	9.0×10^{-3}	1.1×10^{-6} at 20 V

3.8 Concluding remarks

Charge carrier mobilities in coronene diimide liquid crystals (**6b** and **6c**) studied by SCLC technique have been found to be higher than 3 cm²/Vs, the charge carrier mobility in graphite along the direction perpendicular to the graphite layers.

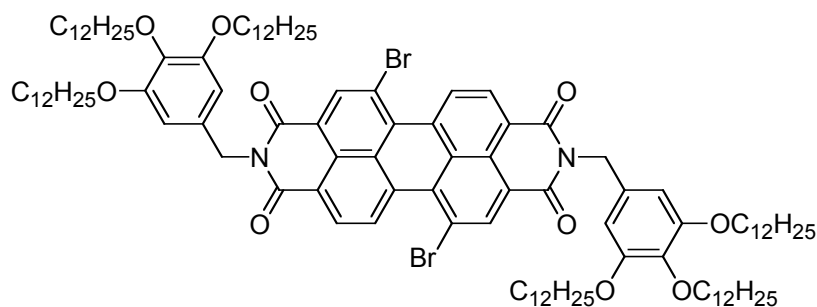
Upon increasing the core size from the perylene diimides to the coronene diimides, the estimated LUMO level is raised by 0.3 eV. The core-size displays a remarkable effect on the order of the mesophases of the two types of materials — ordered columnar mesophases in the coronene diimides vs. disordered columnar mesophases in the perylene diimides. The significant increase in the mesophase order should lead to a large increase in the charge carrier mobility in coronene diimides compared with that in perylene diimides. However, it remains unclear at the molecular level how the change of the aromatic core from perylene diimides to coronene diimides would affect the reorganization energy and the intermolecular transfer integral. Insightful information on

the reorganization energy and the intermolecular transfer integral of these compounds will lead to further understanding of the slightly increased charge carrier mobility observed from perylene diimides to coronene diimides.

In addition, the difference in the charge carrier mobilities of the coronene diimides may be understood in terms of the differences in the phase transition enthalpies, the ordering of the mesophases, and the aggregation constants. Compounds **6c** and **6b** have quite similar phase transition enthalpies associated with the thermal transition from the liquid crystalline phase to the isotropic phase, which are higher than that for compounds **6c** and **6d**. Also XRD of compound **6b** shows more and sharper peaks in the low angle region than the other compounds, indicating a more ordered mesophase in compound **6b** than that for the other three compounds. Moreover, the highest aggregation constant is found for compound **6b**, followed by the aggregation constants for **6c** and **6a** (compounds with the same imide group); the highest charge carrier mobility is also found in **6b**, followed by that in **6c** and **6a** (compounds with the same imide group). Since all four coronene diimides **6a - d** have similar energy levels and intracolumnar distances (ca. 3.5 Å), the extremely low charge carrier mobility found in compound **6d** may arise from the unfavorable molecular packing in **6d** due to the presence of the dove-tailed side chains. The bulky dove-tailed side chains may cause displacements of the discs within the columns, possibly leading to less molecular orbital overlap and thus possibly a lower intermolecular transfer integral. The difference in the charge carrier mobilities of the coronene diimides demonstrates that the side chains can have a significant effect on the charge carrier mobilities of discotic liquid crystals by mainly affecting the molecular packing and the ordering of the mesophase.

3.9 Experimental

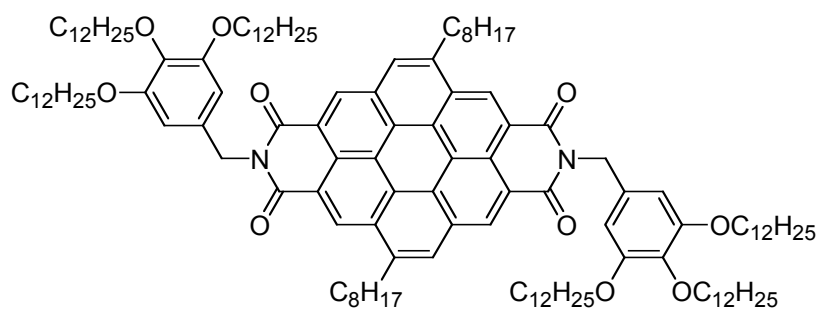
The general experimental information is similar to that described in Chapter 2, unless otherwise stated. Fluorescence spectra were collected on a Jobin Yvon Spex Fluorolog-III fluorimeter using 1 cm cells. Quantum yields were determined on three deoxygenated dichloromethane solutions with the absorbance controlled between 0.01 - 0.03, using perylene ($\Phi_f = 0.94$ in cyclohexane)²⁵ as the standard. For aggregation studies, absorption spectra were recorded using 2 mm cells on samples with concentrations higher than 1.0×10^{-5} M and 1 cm cells on samples with concentrations lower than 1.0×10^{-5} M.



Synthesis of *N,N'*-(3,4,5-tris(dodecyloxybenzyl))-1,7-dibromo-3,4,9,10-perylene diimide

1,7-Dibromoperylene dianhydride (1.07 g, 1.95 mmol) in BuOH/H₂O (160 mL 1:1 (v/v)) was sonicated for 10 min. Tri(dodecyloxy)benzyl amine (3.86 g, 5.85 mmol) was added and the reaction was stirred at 80 °C for 1 day. Concentrated HCl (15 mL) was added, the resultant precipitate was filtered and was purified by column chromatography eluting with 1:1 chloroform/hexane. 3.01 g (84%) of a red solid was obtained. ¹H NMR (500 MHz, CDCl₃): δ (ppm): 9.43 (d, $J = 8.0$ Hz, 2H), 8.90 (s, 2H), 8.67 (d, $J = 8.5$ Hz, 2H), 6.79 (s, 4H), 5.26 (s, 4H), 3.94 (t, $J = 7.0$ Hz, 8H), 3.87 (t, $J = 7.0$ Hz, 4H), 1.75 (m,

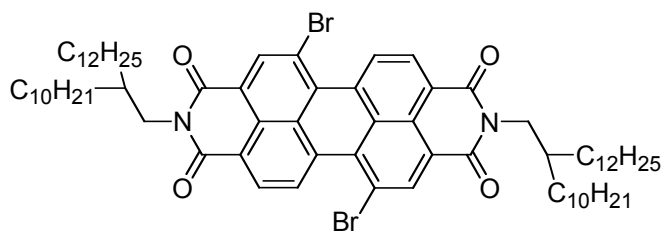
8H), 1.68 (m, 4H), 1.5-1.1 (m, 108H), 0.85 (t, $J = 7.0$ Hz, 18H). ^{13}C NMR (125 MHz, CDCl_3): δ (ppm): 162.8, 163.4, 153.0, 138.2, 137.9, 132.1, 131.7, 130.2, 129.2, 128.5, 126.9, 123.2, 122.7, 120.8, 108.2, 73.4, 69.2, 44.0, 31.9, 30.3, 29.7, 29.6, 29.5, 29.4, 29.36, 26.1, 22.7, 14.1. (10 carbon resonances were not observed presumably due to near equivalencies leading to overlap of resonances). HRMS (MALDI), m/z : calcd. for $\text{C}_{110}\text{H}_{164}\text{N}_2\text{O}_{10}\text{Br}_2$, 1831.0753; found (M+H) 1832.0824. Elemental analysis, calcd. for $\text{C}_{110}\text{H}_{164}\text{N}_2\text{O}_{10}\text{Br}_2$ C 72.03, H 9.01, N 1.53; found C 72.23, H 9.30, N 1.56.



Synthesis of coronene diimide 6a

N,N'-(3,4,5-Tri(dodecyloxy)benzyl)-1,7-dibromo-3,4,9,10-perylene diimide (1.47 g, 0.8 mmol) was suspended in toluene (50 mL) and triethylamine (5 mL) and the solution was deoxygenated with nitrogen for 10 min. Tetrakis(triphenylphosphine)palladium(0) (0.12 g, 0.1 mmol) and copper(I) iodide (0.02 g, 0.1 mmol) were added. After the mixture was further deoxygenated for 10 min, 1-decyne (0.6 mL, 3.3 mmol) was added. The reaction was heated at 65 °C under nitrogen for 1 day. DBU (0.5 mL) was added and the temperature was raised to 110 °C and the reaction was further stirred at this temperature under nitrogen for 21 h. After cooling to room temperature, the reaction was poured into 2 N HCl solution and was extracted with dichloromethane. The organic solution was dried over anhydrous MgSO_4 and was

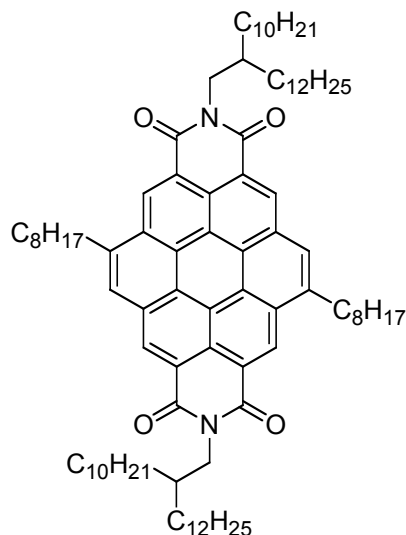
filtered. The solvent was removed and the residue was purified by column chromatography eluting with 2:1 chloroform/hexane. Then five more purifications were performed to obtain 0.75 g (48%) of a yellow solid. ^1H NMR (500 MHz, CD_2Cl_2): δ (ppm): 9.16 (s, 2H), 8.85 (s, 2H), 7.89 (s, 2H), 7.02 (s, 4H), 5.55 (s, 4H), 4.08 (broad s, 8H), 3.87 (t, $J = 6.5$ Hz, 4H), 3.36 (broad s, 4H), 2.0 - 1.0 (m, 144H), 0.93 (t, 6H), 0.81 (m, 18H). HRMS (MALDI), m/z : calcd. for $\text{C}_{130}\text{H}_{198}\text{N}_2\text{O}_{10}$, 1947.5046; found 1947.5047. Elemental analysis: calcd. for $\text{C}_{130}\text{H}_{198}\text{N}_2\text{O}_{10}$, C 80.11, H 10.24, N 1.44; found C 80.23, H 10.24, N 1.49.



Synthesis of *N,N'*-(2-decyl-tetradecyl)-1,7-dibromo-3,4,9,10-perylene diimide

1,7-Dibromo-3,4,9,10-perylene dianhydride (2.74g, 4.98 mmol) in BuOH/ H_2O (1:1, v:v) (200 mL) was sonicated for 10 min. 2-Decyl-1-tetradecylamine (6.2 g, 17.53 mmol) was added and the reaction mixture was heated at 80 °C for 17 h under nitrogen. Concentrated HCl (20 mL) was added and the mixture was stirred at room temperature for 30 min. The mixture was extracted with chloroform. The organic solution was dried over anhydrous MgSO_4 and was filtered. The solvent was removed and the residue was purified by column chromatography eluting with 1:1 CHCl_3 /Hexane, 4.9 g (81%) of a red solid was obtained. ^1H NMR (500 MHz, CDCl_3): δ (ppm): 9.43 (d, $J = 8.5$ Hz, 2H), 8.87 (s, 2H), 8.64 (d, $J = 8.0$ Hz, 2H), 4.11 (d, $J = 7.0$ Hz, 4H), 1.98 (m, 2H), 1.5 - 1.1 (m, 80H), 0.84 (m, 12H). ^{13}C NMR (125 MHz, CDCl_3): δ (ppm): 163.2, 162.7, 138.1, 132.9, 132.7, 130.0, 129.2, 128.4, 126.9, 123.1, 122.7, 120.8, 44.8, 36.6, 31.9, 31.7, 31.6, 30.0,

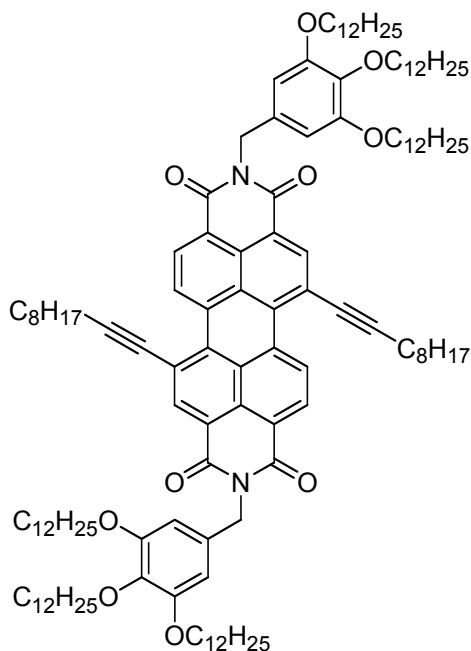
29.68, 29.65, 29.3, 26.5, 22.7, 14.1.(12 carbon resonances were not observed presumably due to near equivalencies leading to overlap of resonances). HRMS (MALDI), m/z : calcd. for $C_{72}H_{104}Br_2N_2O_4$, 1219.6536; found (M+H) 1220.6513. Elemental analysis: calcd. for $C_{72}H_{104}Br_2N_2O_4$, C 70.80, H 8.58, N 2.29; found C 70.98, H 8.59, N 2.34.



Synthesis of coronene diimide 6d

N,N'-(2-Decyl-tetradecyl)-1,7-dibromo-3,4,9,10-perylene diimide (2.2 g, 1.8 mmol) was dissolved in toluene (50 mL) and triethylamine (10 mL) and was deoxygenated with nitrogen for 10 min. Tetrakis(triphenylphosphine)palladium(0) (0.28 g, 0.24 mmol), copper(I) iodide (0.034 g, 0.18 mmol) and 1-decyne (1.3 mL, 7.20 mmol) were added successively. The reaction was heated at 65 °C under nitrogen for 1 day. DBU (0.5 mL) was added and the reaction temperature was raised to 100 °C and stirred for another 16 h. Then 0.5 mL more DBU was added and the reaction temperature was raised to 110 °C and the reaction was further stirred at this temperature for 1 day. The reaction mixture was cooled to room temperature and was poured into 2 N HCl solution, extracted with dichloromethane. The solvent was removed and the residue was purified by column chromatography eluting with 1:3 chloroform/hexane. 1.9 g (86%) of a yellow

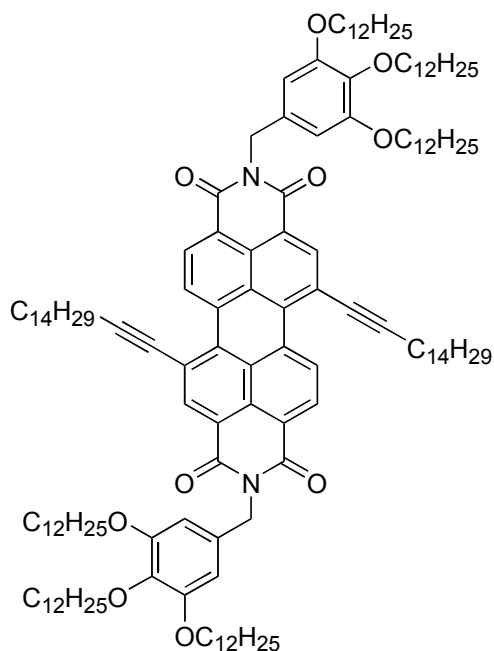
solid was obtained. ^1H NMR (500 MHz, CDCl_3): δ (ppm): 9.32 (s, 2H), 9.10 (s, 2H), 8.25 (s, 2H), 4.42 (d, $J = 7.0$ Hz, 4H), 3.52 (t, $J = 7.0$ Hz, 4H), 2.15 (m, 2H), 2.00 (m, 4H), 1.63 (m, 4H), 1.55 - 1.0 (m, 104H), 0.91 (t, $J = 7.0$ Hz, 6H), 0.80 (m, 12H). ^{13}C NMR (125 MHz, CDCl_3): δ (ppm): 164.9, 164.7, 141.1, 129.4, 128.7, 128.1, 127.5, 125.5, 122.1, 121.5, 121.0, 120.8, 120.7, 119.5, 45.5, 37.5, 34.0, 32.4, 32.3, 31.3, 30.64, 30.62, 30.4, 30.1, 30.07, 30.01, 29.9, 29.74, 29.70, 27.1, 23.2, 23.0, 14.6, 14.5. (11 carbon resonances were not observed presumably due to near equivalencies leading to overlap of resonances). HRMS (MALDI), m/z calcd. for $\text{C}_{92}\text{H}_{138}\text{N}_2\text{O}_4$, 1336.0808; found (M+H) 1337.0807. Elemental analysis: calcd. for $\text{C}_{92}\text{H}_{138}\text{N}_2\text{O}_4$, C 82.70, H 10.41, N 2.10; found C 82.82, H 10.55, N 2.21.



Synthesis of *N,N'*-(3,4,5-tri(dodecyloxy)benzyl)-1,7-di(octyl-ethynyl)-3,4,9,10-perylene diimide

N,N'-(3,4,5-Tri(dodecyloxy)benzyl)-1,7-dibromo-3,4,9,10-perylene diimide (1.02 g, 0.56 mmol) was suspended in toluene (35 mL) and triethylamine (3.5 mL) and the resulting mixture was deoxygenated with nitrogen for 10 min.

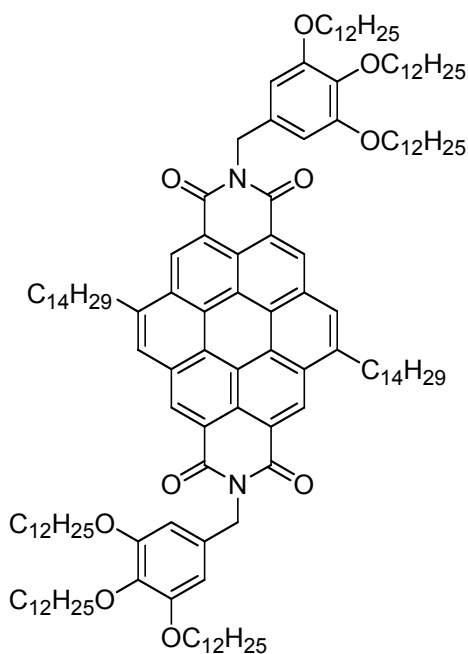
Tetrakis(triphenylphosphine)palladium(0) (0.064 g, 0.055 mmol), copper(I) iodide (0.012 g, 0.063 mmol) and 1-decyne (0.4 mL, 2.20 mmol) were added successively. After the reaction was heated at 65 °C under nitrogen for 22 h, it was poured into 2 N HCl solution. The solvent was removed and the residue was purified by column chromatography eluting with 2:1 chloroform/hexane, 0.94 g (87%) of a red solid was obtained. ¹H NMR (500 MHz, CDCl₃): δ (ppm): 10.05 (d, *J* = 8.5 Hz, 2H), 8.72 (s, 2H), 8.59 (d, *J* = 8.5 Hz, 2H), 6.79 (s, 4H), 5.27 (s, 4H), 3.95 (t, *J* = 6.5 Hz, 8H), 3.87 (t, *J* = 6.5 Hz, 4H), 2.62 (t, *J* = 7.0 Hz, 4H), 1.8-1.6 (m, 16H), 1.53 (m, 4H), 1.5 - 1.1 (m, 124H), 0.85 (m, 24H). ¹³C NMR (125 MHz, CDCl₃): δ (ppm): 163.3, 163.1, 153.0, 138.2, 137.8, 134.3, 133.9, 132.0, 130.4, 127.5, 127.2, 127.0, 122.8, 121.8, 121.0, 108.1, 101.5, 82.2, 73.4, 69.1, 43.9, 31.9, 31.8, 30.3, 29.73, 29.70, 29.65, 29.61, 29.46, 29.44, 29.36, 29.23, 29.21, 29.13, 28.3, 26.1, 22.7, 22.6, 20.3, 14.1. (11 carbon resonances were not observed presumably due to near equivalencies leading to overlap of resonances). HRMS (MALDI), *m/z*, calcd. for C₁₃₀H₁₉₈N₂O₁₀ 1947.5038; found 1947.5046. Elemental analysis: calcd. for C₁₃₀H₁₉₈N₂O₁₀, C 80.11, H 10.24, N 1.44; found C 80.25, H 10.26, N 1.46.



Synthesis of *N,N'*-(3,4,5-tri(dodecyloxy)benzyl)-1,7-di(tetradecyl-ethynyl)-3,4,9,10-perylene diimide

N,N'-(3,4,5-Tri(dodecyloxy)benzyl)-1,7-dibromo-3,4,9,10-perylene diimide (2.0 g, 1.1 mmol) was suspended in toluene (70 mL) and triethylamine (10 mL). The resulting solution was deoxygenated with nitrogen for 10 min. Tetrakis(triphenylphosphine)palladium(0) (0.12 g, 0.1 mmol), copper(I) iodide (0.02 g, 0.1 mmol) and 1-hexadecyne (1.2 mL, 4.3 mmol) were added successively. After the reaction was heated at 70 °C under nitrogen for 42 h, it was poured into 2 N HCl solution. The solvent was removed and the residue was purified by column chromatography eluting with 2:1 chloroform/hexane, 1.96 g (85%) of a red solid was obtained. ¹H NMR (500 MHz, CDCl₃): δ (ppm): 9.95 (d, *J* = 8.5 Hz, 2H), 8.57 (s, 2H), 8.49 (d, *J* = 8.0 Hz, 2H), 6.79 (s, 4H), 5.28 (s, 4H), 3.95 (t, *J* = 6.0 Hz, 8H), 3.86 (t, *J* = 6.5 Hz, 4H), 2.61 (t, *J* = 7.0 Hz, 4H), 1.8-1.6 (m, 16H), 1.6 - 1.1 (m, 152H), 0.85 (t, *J* = 7.0 Hz, 24H). ¹³C NMR (125 MHz, CDCl₃): δ (ppm): 163.1, 162.9, 153.0, 138.1, 137.8, 134.0, 133.6,

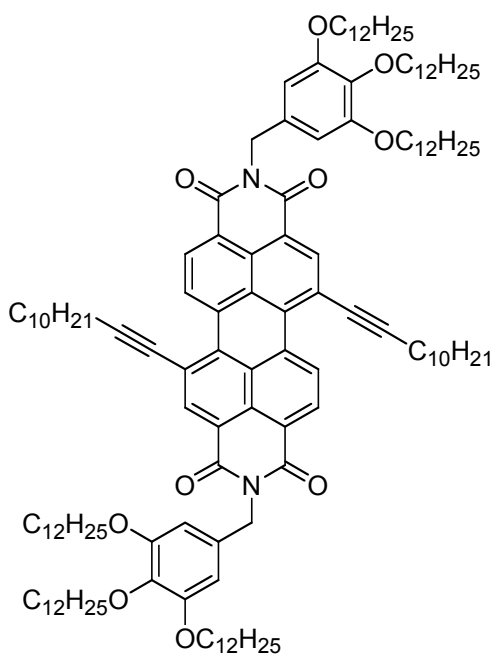
131.9, 130.2, 127.3, 127.1, 126.8, 122.7, 121.7, 120.9, 108.0, 101.8, 82.2, 73.3, 69.1, 43.9, 31.9, 30.3, 29.71, 29.65, 29.57, 29.47, 29.45, 29.36, 29.3, 29.2, 28.3, 26.1, 22.7, 20.3, 14.1. (21 carbon resonances were not observed presumably due to near equivalencies leading to overlap of resonances). HRMS (MALDI), m/z : calcd. for $C_{142}H_{222}N_2O_{10}$ 2115.6; found (M+H) 2116.8. Elemental analysis: calcd. for $C_{142}H_{222}N_2O_{10}$, C 80.55, H 10.57, N 1.32; found C 80.69, H 10.68, N 1.36.



Synthesis of coronene diimide 6c

N,N'-(3,4,5-tri(dodecyloxy)benzyl)-1,7-di(tetradecyl-ethynyl)-3,4,9,10-perylene diimide (1.78 g, 0.84 mmol) was dissolved in toluene (50 mL), DBU (1 mL) was combined and the mixture was heated at 110 °C under argon for 42 h. After cooling to room temperature, the reaction mixture was poured into 2 N HCl and extracted with hexane. After removal of solvent, the material was purified by column chromatography eluting with 1:1 chloroform/hexane. 0.65 g (37%) of a yellow solid was obtained. 1H NMR (500 MHz, $CDCl_3$): δ (ppm): 9.55 (s, 2H), 9.27 (s, 2H), 8.26 (s, 2H), 7.05 (s, 4H), 5.62 (s, 4H), 4.08 (br. s, 8H), 3.89 (t, $J = 6.5$ Hz, 4H), 3.57 (br. s, 4H), 1.97 (br. m, 4H),

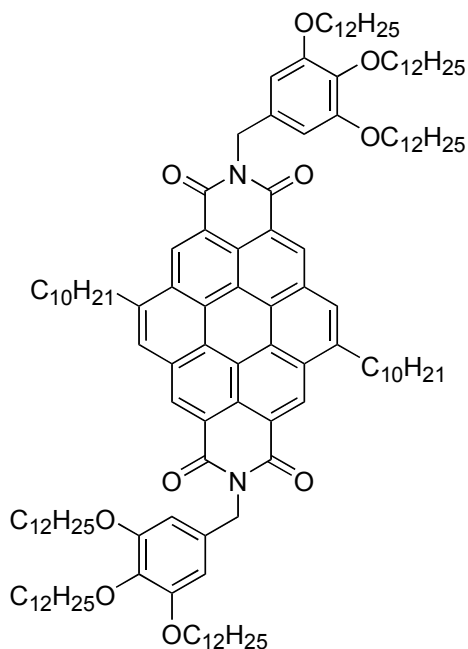
1.78 (m, 8H), 1.69 (m, 4H), 1.65 (m, 4H), 1.5 - 1.1 (m, 148H), 0.84 (m, 24H). ^{13}C NMR (125 MHz, CDCl_3): δ (ppm): 164.1, 163.9, 153.2, 140.7, 138.0, 132.4, 129.1, 128.1, 127.5, 127.1, 125.2, 121.4, 120.9, 120.7, 120.4, 120.2, 118.8, 108.4, 73.4, 69.3, 44.4, 33.6, 31.93, 31.88, 31.1, 30.4, 29.96, 29.79, 29.78, 29.76, 29.70, 29.68, 29.64, 29.63, 29.57, 29.53, 29.4, 29.3, 26.2, 26.1, 22.7, 22.6, 14.09, 14.06. (13 carbon resonances were not observed presumably due to near equivalencies leading to overlap of resonances). HRMS (MALDI), m/z calcd. for $\text{C}_{142}\text{H}_{222}\text{N}_2\text{O}_{10}$ 2115.6924; found 2115.6920. Elemental analysis: calcd. for $\text{C}_{142}\text{H}_{222}\text{N}_2\text{O}_{10}$, C 80.55, H 10.57, N 1.32; found C 80.32, H 10.50, N 1.35.



Synthesis of *N,N'*-(3,4,5-tri(dodecyloxy)benzyl)-1,7-di(decyl-ethynyl)-3,4,9,10-perylene diimide

N,N'-(3,4,5-Tri(dodecyloxy)benzyl)-1,7-dibromo-3,4,9,10-perylene diimide (1.60 g, 0.87 mmol) was suspended in Et_3N (8 mL) and toluene (60 mL) and the resulting solution was deoxygenated with argon for 10 min.

Tetrakis(triphenylphosphine)palladium(0) (0.12 g, 0.10 mmol), copper(I) iodide (0.02 g, 0.10 mmol) and 1-dodecyne (0.76 mL, 3.48 mmol) were added successively. After the reaction was heated at 70 °C under argon for 24 h, it was cooled to room temperature and washed with 2 N HCl solution twice. The solvent was removed and the residue was purified by column chromatography eluting with 2:1 chloroform/hexane. 1.16 g (73%) of a dark red solid was obtained. ¹H NMR (500 MHz, CDCl₃): δ (ppm): 9.98 (d, *J* = 8.0 Hz, 2H), 8.67 (s, 2H), 8.53 (d, *J* = 8.0 Hz, 2H), 6.79 (s, 4H), 5.25 (s, 4H), 3.95 (t, *J* = 6.5 Hz, 8H), 3.86 (t, *J* = 6.5 Hz, 4H), 2.61 (t, *J* = 2.61, 4H), 1.8 - 1.6 (m, 16H), 1.6 - 1.1 (m, 136H), 0.86 (m, 24H). ¹³C NMR (125 MHz, CDCl₃): δ (ppm): 163.2, 163.0, 153.0, 138.2, 137.8, 134.1, 133.7, 132.0, 130.3, 127.4, 127.2, 126.8, 122.7, 121.7, 120.9, 108.0, 101.7, 82.2, 73.4, 69.1, 43.9, 31.9, 30.3, 29.73, 29.72, 29.71, 29.67, 29.65, 29.61, 29.56, 29.47, 29.45, 29.4, 29.3, 29.26, 29.19, 28.3, 26.1, 22.7, 20.3, 14.1. (12 carbon resonances were not observed presumably due to near equivalencies leading to overlap of resonances). Elemental analysis: calcd. for C₁₃₄H₂₀₆N₂O₁₀, C 80.27, H 10.36, N 1.40; found C 80.28, H 10.39, N 1.45.



Synthesis of coronene diimide 6b

N,N'-(3,4,5-tri(dodecyloxy)benzyl)-1,7-di(decyl-ethynyl)-3,4,9,10-perylene diimide (1.09 g, 0.54 mmol) was dissolved in toluene (100 mL) and was heated to 100 °C under argon. Then DBU (0.32 mL) was added. After the reaction was heated at 100 °C under argon for 20 h, it was cooled to room temperature and washed with 2 N HCl twice. The solvent was removed and the residue was purified by column chromatography eluting with dichloromethane, 0.90 g (83%) of a yellow solid was obtained. ¹H NMR (500 MHz, CDCl₃): δ (ppm): 9.56 (s, 2H), 9.29 (s, 2H), 8.28 (s, 2H), 7.05 (s, 4H), 5.62 (s, 4H), 4.08 (br. s, 8H), 3.88 (t, *J* = 7.0 Hz, 4H), 3.58 (br. s, 4H), 1.98 (m, 4H), 1.78 (m, 8H), 1.68 (m, 4H), 1.59 (m, 4H), 1.5 - 1.1 (m, 136H), 0.85 (m, 24H). ¹³C NMR (125 MHz, CDCl₃): δ (ppm): 163.8, 163.6, 153.2, 140.2, 138.0, 132.3, 128.7, 127.6, 127.0, 126.6, 124.8, 120.8, 120.4, 120.1, 119.8, 119.5, 118.1, 108.5, 73.3, 69.2, 44.26, 33.4, 32.0, 31.9, 30.8, 30.4, 30.0, 29.8, 29.71, 29.68, 29.64, 29.61, 29.53, 29.45, 29.4, 29.3, 26.2, 26.1, 22.7, 22.6, 14.1, 14.0. (11 carbon resonances were not observed presumably due to near equivalencies leading to overlap of resonances). HRMS (MALDI), *m/z* calcl.

for $C_{134}H_{206}N_2O_{10}$, 2003.5672; found (M+H) 2004.5746. Elemental analysis: calcd. for $C_{134}H_{206}N_2O_{10}$, C 80.27, H 10.36, N 1.40; found C 80.26, H 10.35, N 1.45.

3.10 References

1. Katz, H. E. *Chem. Mater.* 2004, 16, 4748-4756.
2. Lemaur, V.; da Silva Filho, D. A.; Coropceanu, V.; Lehmann, M. Geerts, Y.; Piris, J.; Debije, M. G.; van de Craats, A. M.; Senthilkumar, K.; Siebbeles, L. D. A.; Warman, J. M.; Brédas, J.-L.; Cornil, J. *J. Am. Chem. Soc.* **2004**, 126, 3271-3279.
3. van de Craats, A. M.; Warman, J. M. *Adv. Mater.* **2001**, 13, 130-133.
4. Dresselhaus, M. S.; Dresselhaus, G. *Adv. Phys.* **1981**, 31, 139.
5. Debije, M. G.; Piris, J.; de Haas, M. P.; Warman, J. M.; Tomović, Ž.; Simpson, C. D.; Watson, M. D.; Müllen, K. *J. Am. Chem. Soc.* **2004**, 126, 4641-4645.
6. van de Craats, A. M.; Warman, J. M.; Fechtenkötter, A.; Brand, J. D.; Harbison, M. A.; Müllen, K. *Adv. Mater.* **1999**, 11, 1469-1472.
7. van de Craats, A. M.; Warman, J. M.; Hasebe, H.; Naito, R.; Ohta, K. *J. Phys. Chem. B* **1997**, 101, 9224-9232.
8. Donovan, K. J.; Kreouzis, T.; Scott, K.; Bunning, J. C.; Bushby, R. J.; Boden, N.; Lozman, O. R.; Movaghar, B. *Mol. Cryst. Liq. Cryst.* **2003**, 396, 91-112.
9. (a) Rohr, U.; Schlichting, P.; Böhm, A.; Gross, M.; Meerholz, K.; Bräuchle, C.; Müllen, K. *Angew. Chem. Int. Ed.* **1998**, 37, 1434-1437. (b) Rohr, U.; Kohl, C.; Müllen, K.; van de Craats, A.; Warman, J. *J. Mater. Chem.* **2001**, 11, 1789-1799.
10. Katz, H. E.; Johnson, J.; Lovinger, A. J.; Li, W. *J. Am. Chem. Soc.* **2000**, 122, 7787-7792.
11. Böhm, A.; Arms, H.; Henning, G.; Blaschka, P. DE19547209 A1, 1997
12. Würthner, F.; Stepanenko, V.; Chen, Z.; Saha-Möller, C. R.; Kocher, N.; Stalke, D. *J. Org. Chem.* **2004**, 69, 7933-7939.
13. Adachi, M.; Nagao, Y. *Chem. Mater.* **2001**, 13, 662-669.
14. Lee, S. K.; Zu, Y.; Herrmann, A.; Geerts, Y.; Müllen, K.; Bard, A. *J. Am. Chem. Soc.* 1999, 121, 3513-3520.

15. (a) Czikkely, V.; Försterling, H. D.; Kuhn, H. *Chem. Phys. Lett.* **1970**, *6*, 11-14. (b) Harrison, W. J.; Mateer, D.; Tiddy, G. J. T. *J. Phys. Chem.* **1996**, *100*, 2310-2321. (c) Tobe, Y.; Utsumi, N.; Kawabata, K.; Nagano, A.; Adachi, K.; Araki, S.; Sonoda, M.; Hirose, K.; Naemura, K. J. *J. Am. Chem. Soc.* **2002**, *124*, 5350-5364. (d) Höger, S.; Bonrad, K.; Mourran, A.; Beginn, U.; Möller, M. *J. Am. Chem. Soc.* **2001**, *123*, 5651-5659. (e) Kano, K.; Fukuda, K.; Wakami, H.; Nishiyabu, R.; Pasternack, R. F. *J. Am. Chem. Soc.* **2000**, *122*, 7494-7502.
16. (a) Wu, J.; Fechtenkötter, A.; Gauss, J.; Watson, M. D.; Kastler, M.; Fechtenkötter, C.; Wagner, M.; Müllen, K. *J. Am. Chem. Soc.* **2004**, *126*, 11311-11321. (b) Kastler, Pisula, W.; Wasserfallen, D.; Pakula, T.; Müllen, K.; *J. Am. Chem. Soc.* **2005**, *127*, 4286-4296. (c) Tracz, A.; Jeszka, J. K.; Watson, M. D.; Pisula, W., Müllen, K.; Pakula, T. *J. Am. Chem. Soc.* **2003**, *123*, 125, 1682-1683. (d) Pisula, W.; Menon, A.; Stepputat, M.; Lieberwirth, I.; Kolb, U.; Tracz, A.; Sirringhaus, H.; Pakula, T.; Müllen, K. *Adv. Mater.* **2005**, *17*, 684-689.
17. Martin, R. B. *Chem. Rev.* **1996**, *96*, 3043-3064.
18. (a) Würthner, F.; Thalacker, C.; Diele, S.; Tschierske, C. *Chem. Eur. J.* **2001**, *7*, 2245-2253. (b) Würthner, F.; Chen, Z.; Hoeben, F. J. M.; Osswald, P.; You, C.-C.; Jonkheijm, P.; van Herrikhuyzen, J.; Schenning, A. P. H. J.; van der Schoot, P. P. A. M.; Meijer, E. W.; Beckers, E. H. A.; Meskers, S. C. J.; Janssen, R. A. J. *J. Am. Chem. Soc.* **2004**, *126*, 10611-10618. (c) van Herrikhuyzen, J.; Syamakumari, A.; Schenning, A. P. H. J.; Meijer, E. W. *J. Am. Chem. Soc.* **2004**, *126*, 10021-10027.
19. Langhals, H.; Ismael, R. *J. Org. Chem.* **1998**, *63*, 1915-1917.
20. Origin 7.0
21. (a) Zheng, H.; Lai, C. K.; Swager, T. M. *Chem. Mater.* **1995**, *7*, 2067-2077. (b) Wen, C.-R.; Wang, Y.-J.; Wang, H.-C.; Sheu, H.-S.; Lee, G.-H.; Lai, C. K. *Chem. Mater.* **2005**, *17*, 1646-1654.
22. Demus, D.; Goodby, J.; Gray, G. W.; Spiess, H. W.; Vill, V. *Handbook of Liquid Crystals* Wiley-VCH, Weinheim, New York, 1998.
23. Fechtenkötter, A.; Saalwächter, K.; Harbison, M. A.; Müllen, K.; Spiess, H. W. *Angew. Chem. Int. Ed.* **1999**, *38*, 3099-3042.
24. Adam, D.; Schuhmacher, P.; Simmerer, J.; Häussling, L.; Siemensmeyer, K.; Etzbach, K. H.; Ringsdorf, H.; Haarer, D. *Nature*, **1994**, *371*, 141-143.
25. Berlman, I. B. *Handbook of Fluorescence Spectra of Aromatic Molecules*, Academic Press, 1965.

CHAPTER 4
ENHANCEMENT OF CHARGE CARRIER MOBILITIES IN CORONENE
DIIMIDES WITH BINARY SIDE CHAINS

4.1 Introduction

Incorporation of amphiphilic groups into liquid crystals is a widely used strategy of controlling the self-assembly behavior of liquid crystalline materials.¹ A recent report on perfluoroalkylated triphenylenes (Figure 4.1) demonstrated that spontaneous homeotropic alignment was realized on several different substrates including ITO glass without any surface modification.² Moreover, improvement of the air stability of electron-transport materials (Figure 4.2) by incorporation of perfluoroalkyl groups has been well documented. When measured in air, naphthalene diimides with perfluoroalkyl group have been shown to have electron mobility about several orders of magnitude higher than their analogues with alkyl groups, although the alkyl-substituted naphthalene diimides show superior performance under vacuum.³ 1,7-Biscyanoperylene diimide with perfluoroalkyl group displays a lower reduction potential by 0.11 V than the alkyl-substituted analogue, and shows electron mobility as high as 0.64 cm²/Vs in air.⁴ Even more remarkably, traditionally hole-transport thiophene-based materials can be converted into electron-transport materials after substitution with perfluoroalkyl groups.⁵ It is generally suggested that the electron-withdrawing perfluoroalkyl groups, when close to the functional motifs, may increase the electron-deficiency of the aromatics,⁴ and thus electrochemically stabilize the radical anion; the compact packing of the perfluoroalkyl

groups due to the larger van der Waals radius of F (1.50 Å) than H (1.20 Å), may present kinetic barriers to the diffusion of moisture and oxygen into the electrochemically active sites.^{3c,5d} In all the above instances, the effect of the perfluoroalkyl groups on the performance of the electron-transport materials has only been demonstrated on crystalline materials; their effect on the charge-transport properties of discotic liquid crystals has remained unexplored.

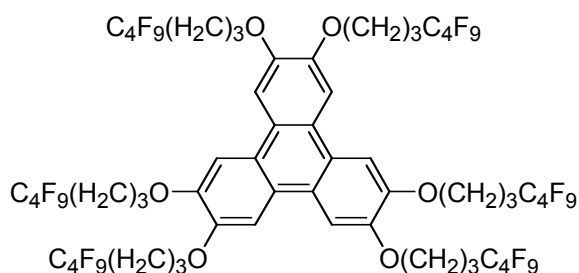


Figure 4.1 Triphenylene with perfluoroalkyl groups that can realize homeotropic alignment on various substrates.

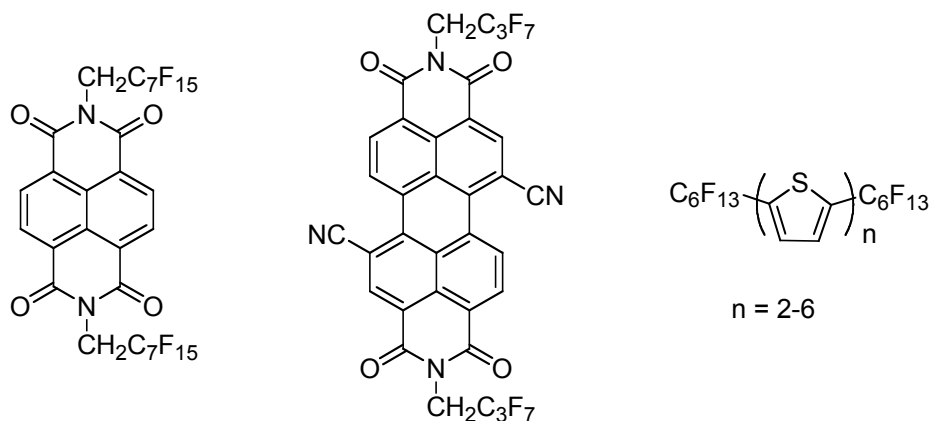


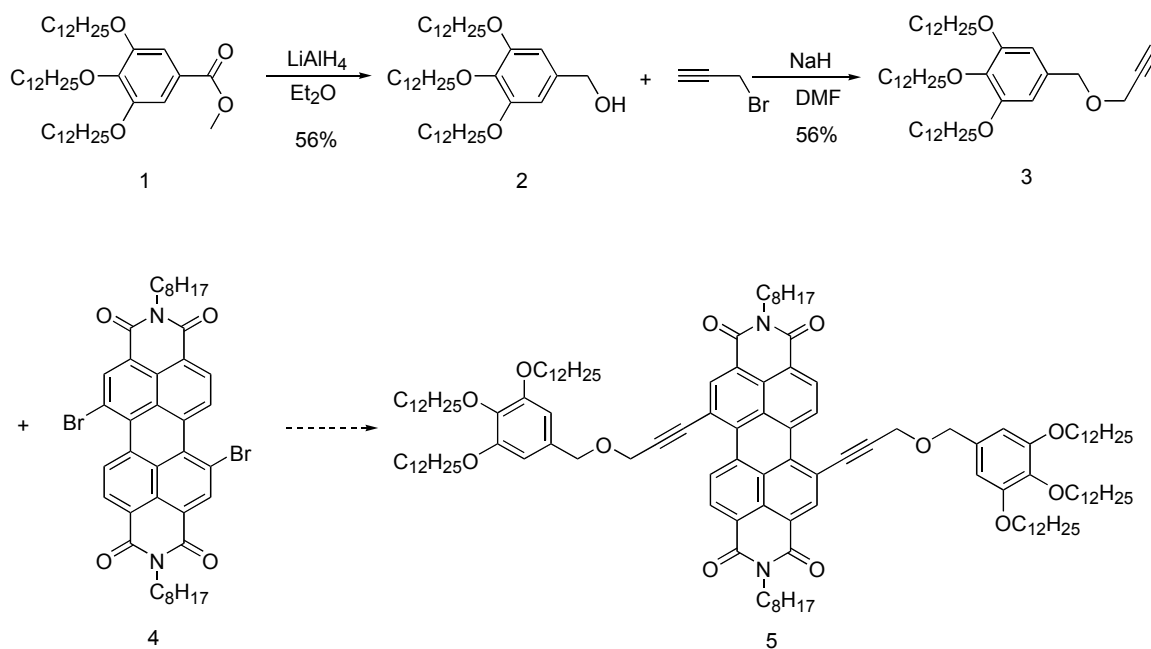
Figure 4.2 Organic semiconducting materials with perfluoroalkyl groups showing improved electron-transport properties.

In the previous chapter, we demonstrated that the side chains can modulate the order of the mesophase of coronene diimides, which in turn can affect the charge carrier mobility. As part of our continuous efforts to further improve the charge-transport properties of coronene diimide derivatives, a segment of perfluoroalkyl group is attached to the imide positions, to constitute the binary side chains in the coronene diimide. We believe that in addition to the possible reduction of the LUMO level, the presence of the binary side chains may lead to a more ordered mesophase in which the alignment of the molecules can be improved due to fluorophobic interaction of the side chains.

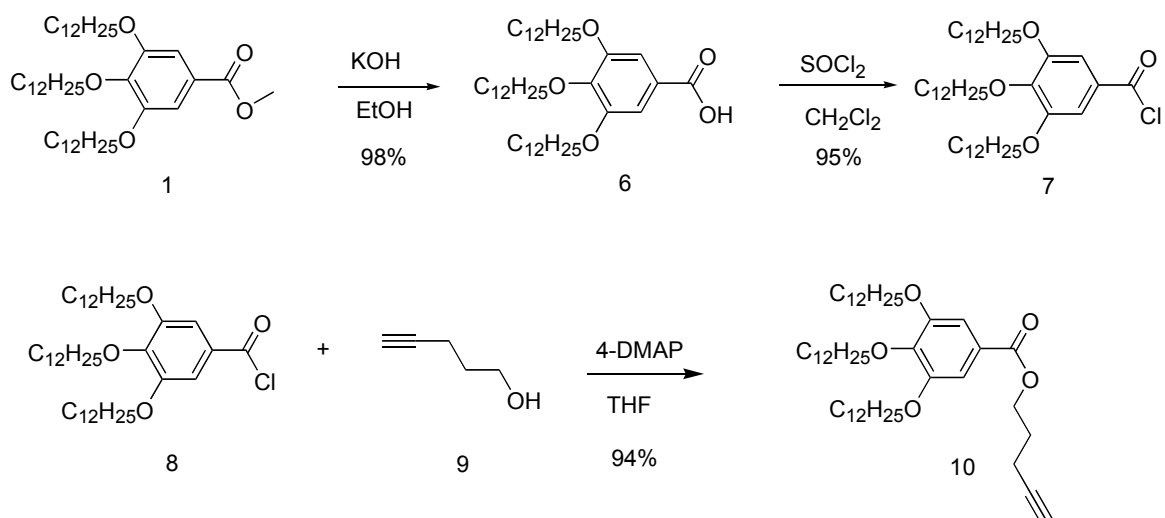
This chapter describes the design, synthesis, liquid crystalline properties and effect of the binary side chains on the SCLC characteristics (by Junsheng Yu, Kippelen group) of the coronene diimides.

4.2 Synthesis

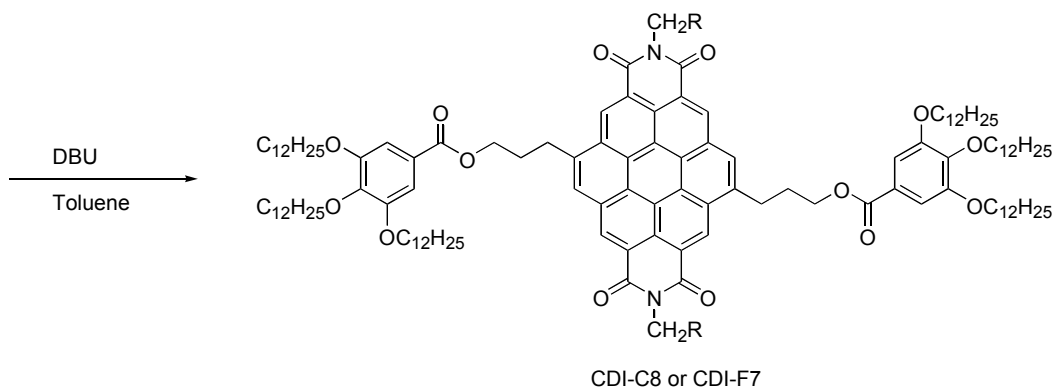
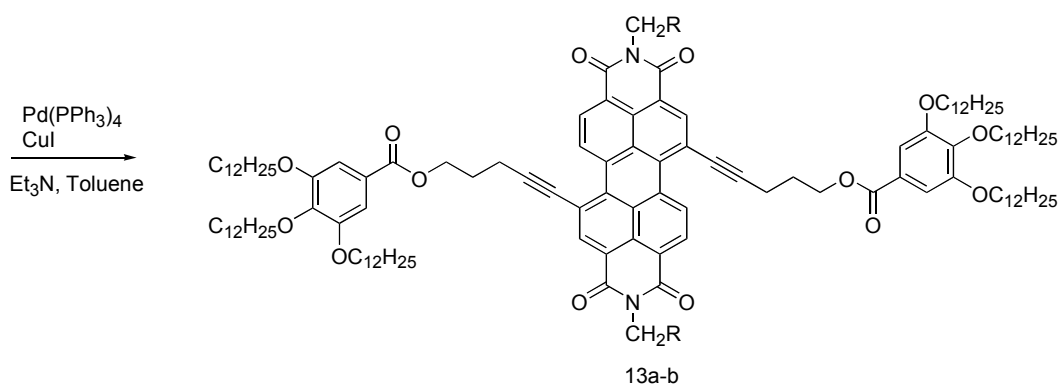
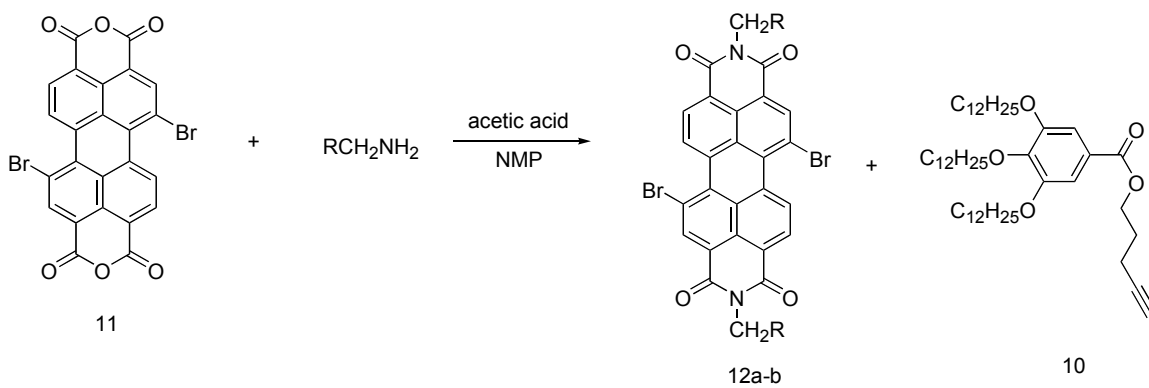
Compared to the coronene diimides previously synthesized, the tri(dodecyloxy)benzyl group is moved from the imide positions to the coronene diimide core via a linker. First, compound **3** with an ether-linker was synthesized (Scheme 4.1). When coupling with the bis-bromoperylene diimide **4**, the desired product compound **5** was not obtained, possibly due to the poor stability of **3** under basic conditions. Then compound **10** with an ester-linker (Scheme 4.2) was synthesized and coupled to the bisbromoperylene diimides successfully (Scheme 4.3). In the coupling reaction of **10** with **12b**, not only **13b** was formed, but also the coronene diimide **CDI-F7**. Then the mixture of **13b** and **CDI-F7** was treated with DBU to convert the remaining alkynyl-substituted compound **13b** coronene diimide **CDI-F7**.



Scheme 4.1 Attempted synthesis of coronene diimide with compound **3** bearing an ether-linker.



Scheme 4.2 Synthesis of compound **10** with an ester linker.



R
 a /CDI-C8: C₇H₁₅
 b/CDI-F7: C₇F₁₅

Scheme 4.3 Synthesis of coronene diimides **CDI-C8** and **CDI-F7**.

4.3 Absorption and emission properties

The absorption and emission spectra of **CDI-C8** and **CDI-F7** in dichloromethane display typical features of coronene diimides (Figure 4.3). The absorption and emission maximum of **CDI-C8** are 508 nm and 511 nm respectively; both the absorption and emission maximum of **CDI-F7** are slightly red-shifted, at 512 nm and 514 nm respectively. The fluorescence quantum yields of these two compounds differ significantly with 0.16 for **CDI-C8** and 0.06 for **CDI-F7**. Additionally, compared with other coronene diimides with tri(dodecyloxy)benzyl groups, the quantum yield of **CDI-C8** is higher than that for **6a - c** in Chapter 3. The difference in the quantum yield may be explained by a possible weak charge transfer process from the relatively electron-rich tri(dodecyloxy)phenyl group to the coronene diimide moiety — the longer spacer and the presence of the carbonyl group that makes the donor less electron-rich in **CDI-C8**, result in a less favorable charge transfer process in **CDI-C8** than in the coronene diimides in Chapter 3, and thus a higher quantum yield; the presence of the perfluoroalkyl segment in **CDI-F7** lowers the LOMO level (see electrochemical data below) of the coronene diimide, making it a stronger electron acceptor for the charge transfer process from the donor and consequently further quenching the fluorescence.

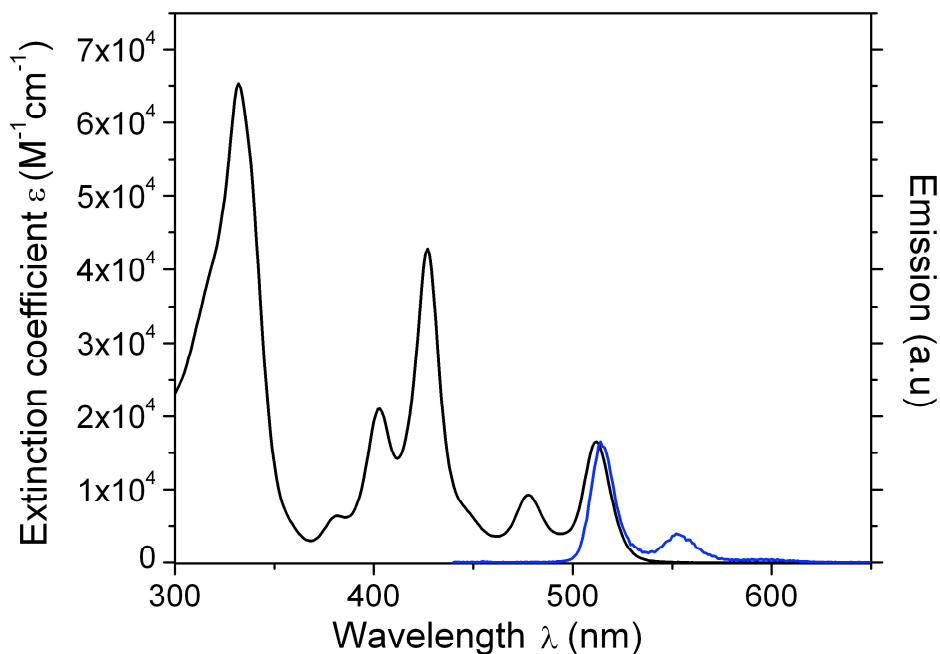


Figure 4.3 Absorption and emission spectra of **CDI-F7** in dichloromethane (excitation wavelength is 400 nm).

4.4 Electrochemical properties

As shown by the cyclic voltammograms in Figure 4.4, **CDI-C8** and **CDI-F7** have different electrochemical behavior. **CDI-C8** shows two successive reversible reductions with the first reduction potential being -1.4 V *vs.* ferrocenium/ferrocene, whereas **CDI-F7** reveals three reversible reductions with a less negative reduction potential for the first reduction wave, being -1.1 V *vs.* ferrocenium/ferrocene. Therefore, **CDI-F7** is more electron-deficient and electron injection into the lower LUMO level of the molecules from the cathode is expected to be more efficient. Lowering the LUMO level by the introduction of a segment of perfluoroalkyl group has also been seen in previous work on 1,7-biscyano-perylene diimide.⁴ In addition, oxidation of these two compounds was not

observed in CV within the solvent window (0.1 M Bu₄NPF₆ dichloromethane solution) when applying positive voltage.

Similarly as in Chapter 2 for the perylene diimides and in Chapter 3 for other coronene diimides, the energy levels of these two coronene diimides **CDI-C8** and **CDI-F7** are estimated using the optical and electrochemical data (Table 4.1). The optical energy gap is estimated from the intersection of the absorption and emission spectra, which is ca. 512-514 nm, providing an optical energy gap of 2.4 eV. The LUMO level for **CDI-C8** is approximately 3.3 eV and the LUMO level for **CDI-F7** is approximately 3.6 eV as estimated from their first reduction potentials. Since no oxidation was observed within the solvent window, the HOMO level is estimated as being HOMO = exciton binding energy + (optical energy gap + LUMO). Thus, a HOMO level lower than 5.7 eV for **CDI-C8** and lower than 6.0 eV for **CDI-F7** can be assumed, when taking the exciton binding energy into account.

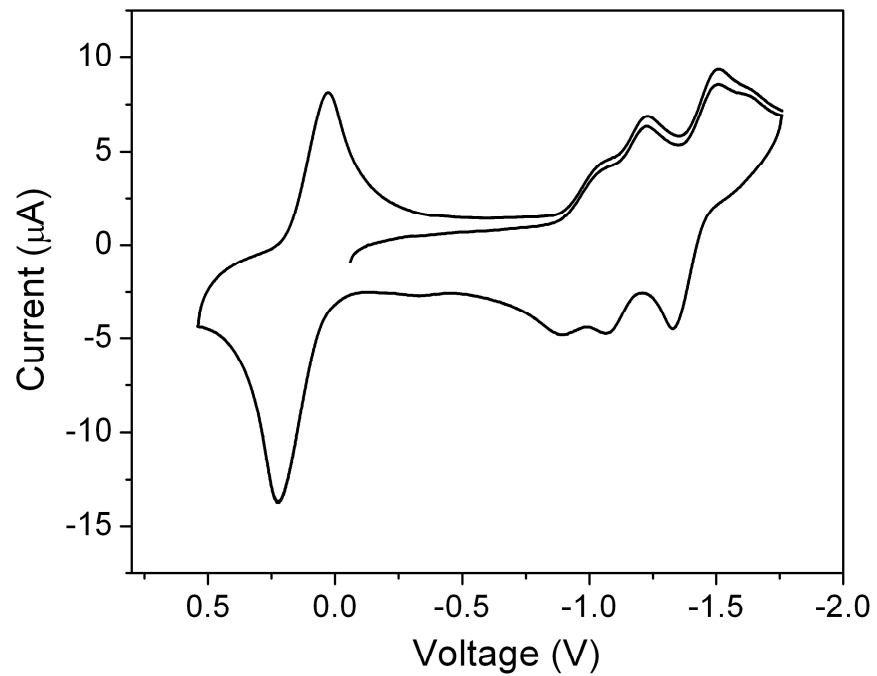
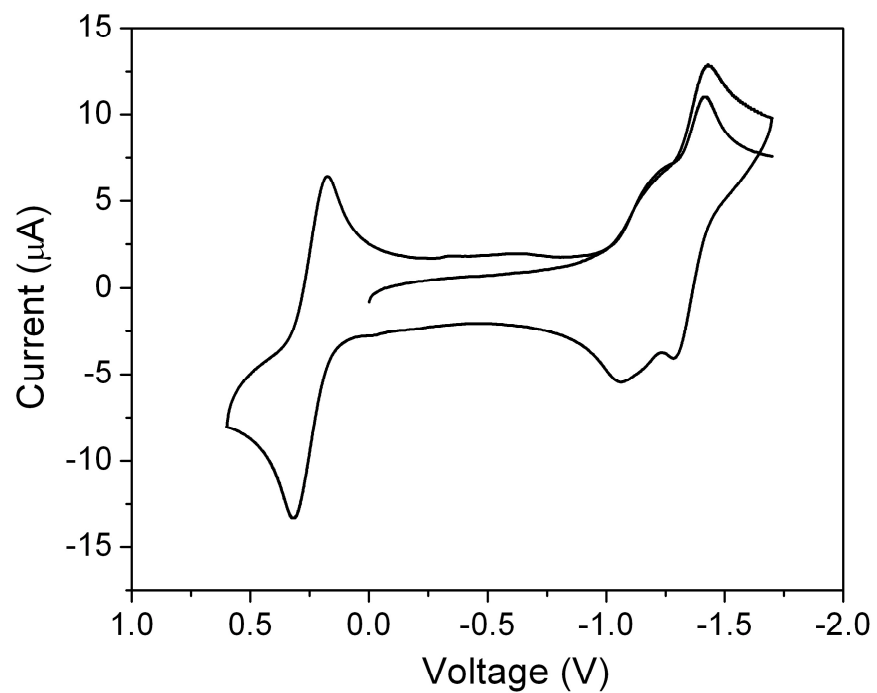


Figure 4.4 Cyclic voltammograms of **CDI-C8** (top) and **CDI-F7** (bottom) in 0.1 M Bu_4NPF_6 dichloromethane solution with Fc^+/Fc (0.5 – 0 V) as internal standard, scan rate = 50 mV/s.

Table 4.1 Summary of the optical and electrochemical (vs. Fc^+/Fc) data of **CDI-C8** and **CDI-F7**.

	$\lambda_{\text{max}}^{\text{ab}}$ (nm)	$\lambda_{\text{max}}^{\text{em}}$ (nm)	ϕ_{f}	X/X' (V)	LUMO (eV)	HOMO (eV)
CDI-C8	508	511	0.16	-1.4	3.3	> 5.7
CDI-F7	512	514	0.06	-1.1	3.6	> 6.0

4.5 Liquid crystalline properties

DSC (Figure 4.5) and POM (Figure 4.6) suggest a hexagonal columnar mesophase for both materials between two thermal transitions, which is further confirmed by XRD study. DSC traces of these two compounds show a wide range phase between two thermal transitions, one transition being slightly above room temperature and the other around 200 °C. The phase transition temperature of **CDI-F7** is higher for the low-temperature transition and lower for the high-temperature transition than that for **CDI-C8**, resulting in a narrower temperature range of the liquid crystalline phase of **CDI-F7** in comparison to **CDI-C8**. Interestingly, the second phase transition enthalpy for **CDI-F7** (12.7 kJ/mol) is significantly higher than that for **CDI-C8** (6.8 kJ/mol), suggesting a higher ordering of the mesophase for **CDI-F7**, possibly arising from the improved alignment of the molecules in the mesophase. Both materials show focal conic fan textures when observed between crossed polarizers after cooling from their isotropic liquid to room temperature.

The X-ray diffraction patterns (Figure 4.7) of the two coronene diimides provide further evidence that both compounds form ordered hexagonal columnar mesophases. Three peaks can be seen in the low angle region of the XRD of **CDI-C8** with the second and the third peaks barely above the noise level. These peaks are indexed to the (100), (110) and (200) peaks with the featured reciprocal d spacing ratio ($1 : \sqrt{3} : 2$) for a hexagonal mesophase. At $2\theta \approx 21^\circ$, a typical region for alkyl halo, there appears a relatively sharp peak. However, as will be discussed later, this unknown peak does not correspond to the broad alkyl diffuse peak and may be a higher order diffraction peak. Additionally, the (001) peak for **CDI-C8**, although being broad, can still be recognized at the wide-angle region, giving an intracolumnar distance of 3.54 Å. The XRD of **CDI-F7** is studied as a function of the thermal history of the material. Obviously a larger number of sharper peaks can be seen, suggesting a more ordered mesophase, consistent with the higher transition enthalpy associated with the phase transitions of **CDI-F7**. In the low angle region, six peaks from (100) up to (220) are well above the noise level at room temperature and their reciprocal d spacing features approximately the typical ratio for a hexagonal mesophase, being $1 : \sqrt{3} : 2 : \sqrt{7} : 3 : \sqrt{12}$. At 100°C, the material still maintains a high order, although the intensity of the (210) peak is too low to be appropriately assigned. All the diffraction peaks at 100 °C are at similar positions compared with that at room temperature. In addition, the peak that appears at ca. 21° at room temperature disappears at 100 °C, indicating a lower order at higher temperature where the molecules are expected to be more mobile. Clearly from the XRD at 100 °C, the alkyl halo centers around 17° rather than 21°. Therefore, the sharp peak around 21° at room temperature is likely from a higher order diffraction peak. Assignment to this peak becomes difficult due to the discontinuity of the progression of the diffraction

peaks. Again, the peak around 25° provides the intermolecular separation of ca. 3.5 Å (Table 4.2), indicative of an ordered mesophase.

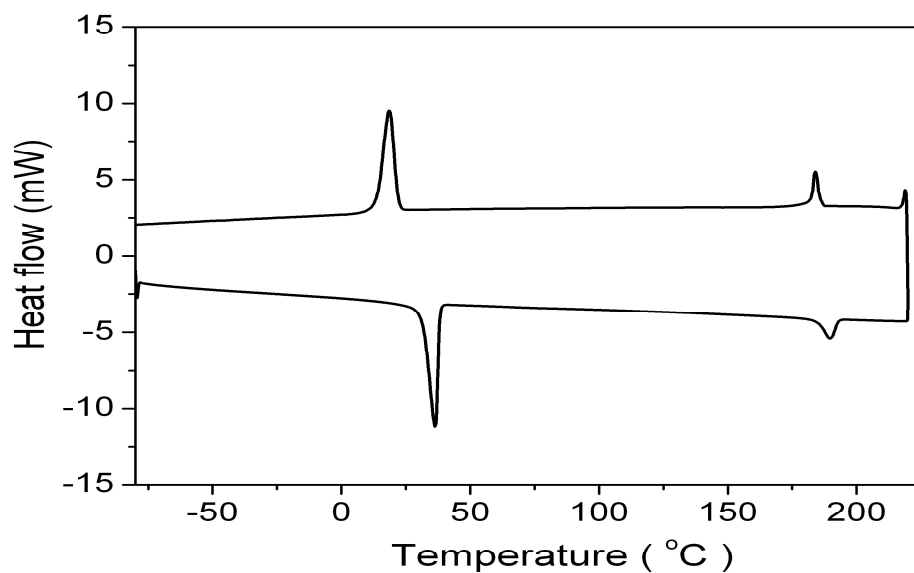
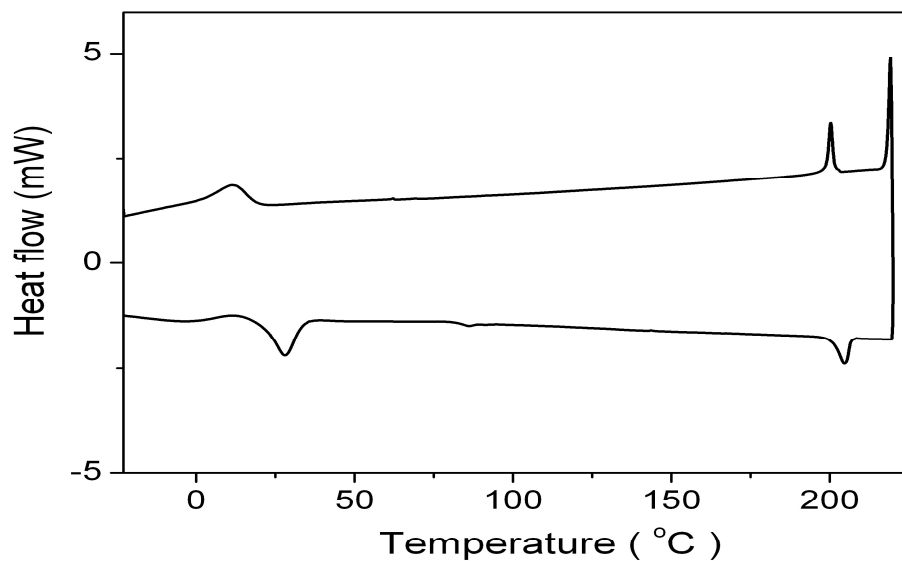


Figure 4.5 DSC traces (second heating - cooling cycle) of **CDI-C8** (top) and **CDI-F7** (bottom).

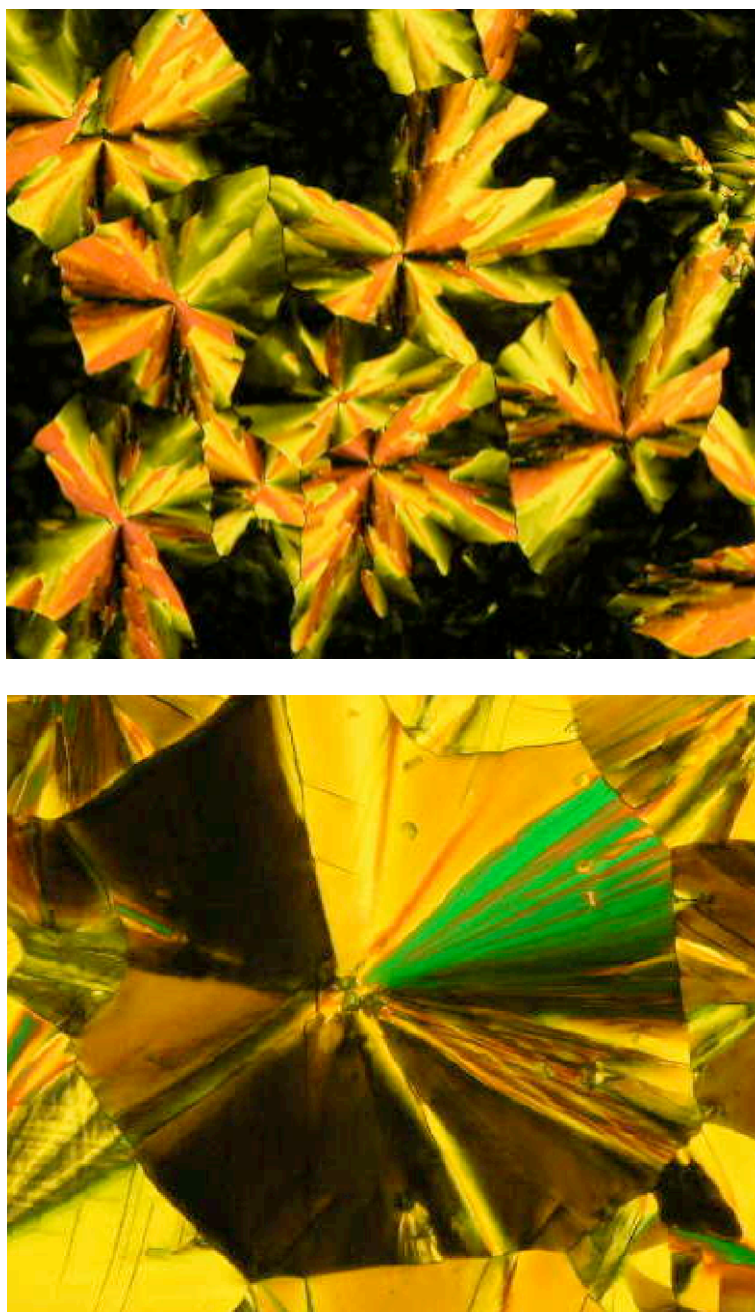


Figure 4.6 Optical textures of **CDI-C8** (top) and **CDI-F7** (bottom) between crossed polarizers (magnification 20 \times) at room temperature after cooling from the isotropic liquid.

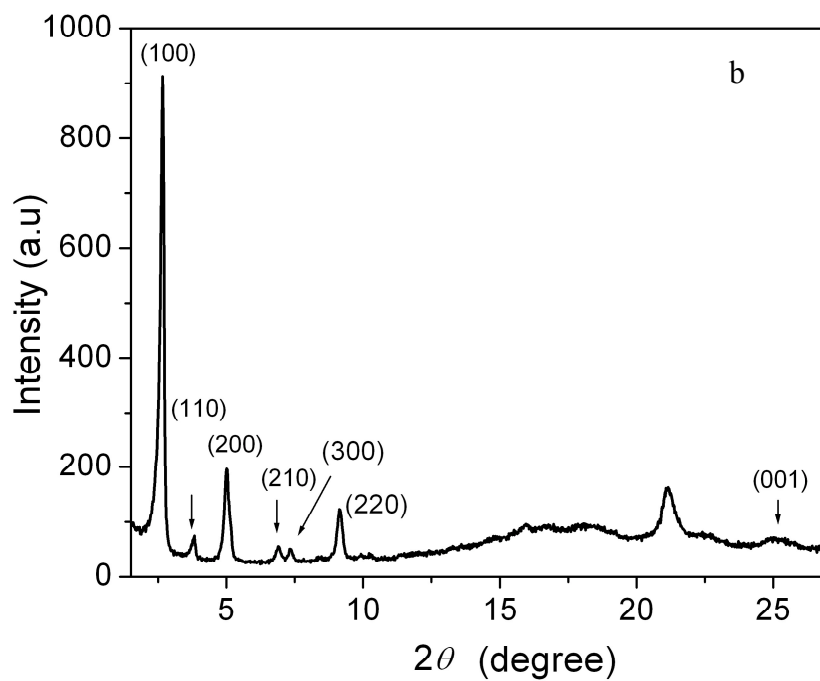
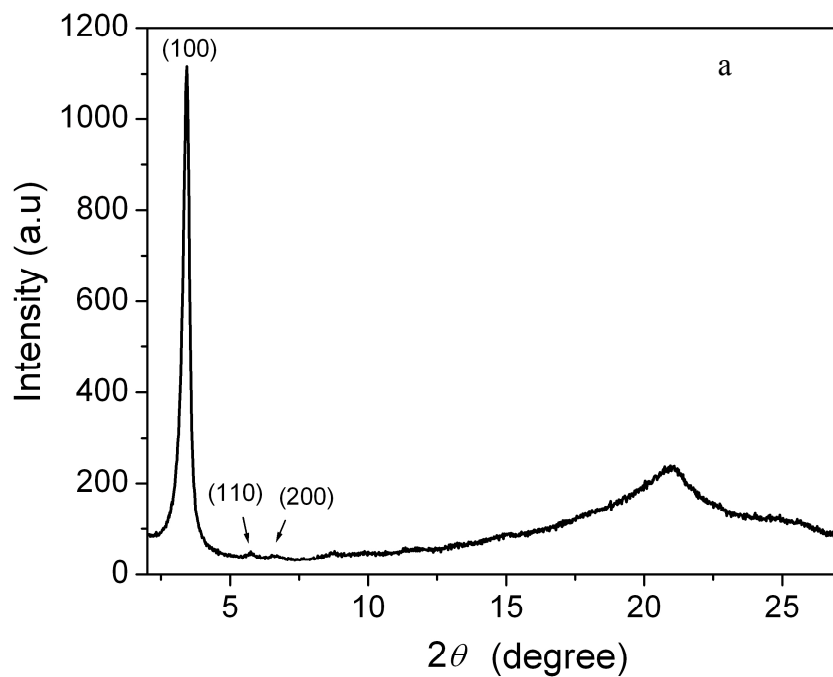


Figure 4.7 XRD of (a) **CDI-C8** at room temperature after cooling from the isotropic phase, (b) **CDI-F7** at room temperature after cooling from the isotropic phase, (c) **CDI-F7** at 100 °C during the second cooling process.

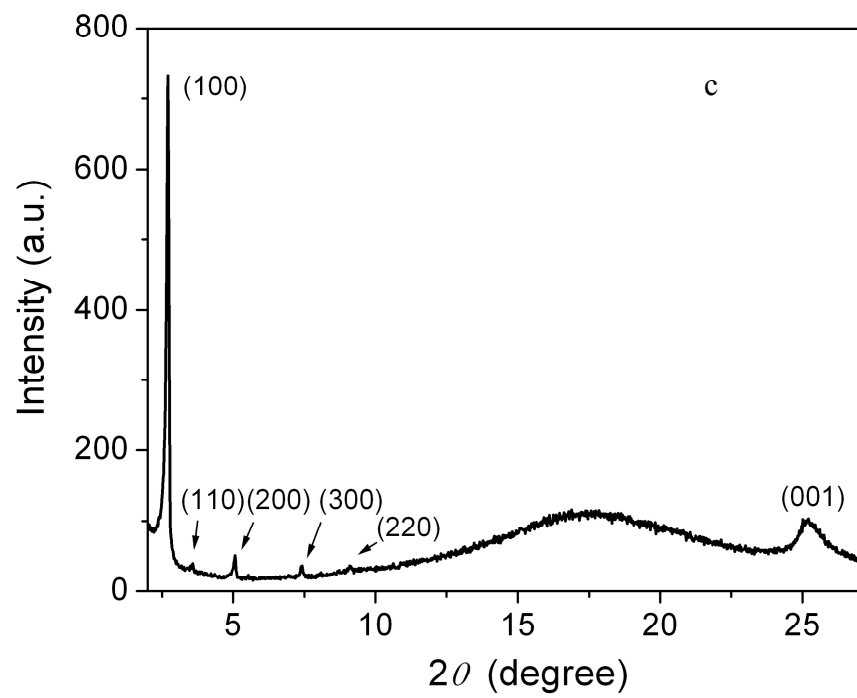


Figure 4.7 (CONT.)

Table 4.2 Summary of the XRD data of **CDI-C8** and **CDI-F7**.

	(<i>hkl</i>)	2θ (degree)	<i>d</i> spacing (Å)	Lattice parameter (Å)	Mesophase
CDI-C8	(100)	3.43	25.73	$a_0 = 29.7$	Col _{ho}
	(110)	5.75	15.35		
	(200)	6.60	13.37		
	(001)	25.15	3.54		
CDI-F7 (at room temperature after the first heating- cooling cycle)	(100)	2.65	33.26	$a_0 = 38.4$	Col _{ho}
	(110)	3.82	23.09		
	(200)	5.01	17.62		
	(210)	6.91	12.78		
	(300)	7.35	12.02		
	(220)	9.13	9.68		
	(001)	24.92	3.57		
CDI-F7 (at 100°C during the second cooling)	(100)	2.71	32.56	$a_0 = 37.60$	Col _{ho}
	(110)	3.58	24.65		
	(200)	5.07	17.43		
	(300)	7.42	12.72		
	(220)	9.10	9.71		
	alkyl	17.37	5.10		
	(001)	25.21	3.53		

4.6 SCLC characterization

SCLC measurements were performed in the device geometry of (+) ITO/CDI (5 μm)/Ag (-) under ambient conditions. As shown in Figure 4.8, from 0 to 0.6 V, the current density is almost linearly dependent on the applied voltage in the form of $J \propto V^{1.04}$ for **CDI-C8**; from 0 to 0.7 V, $J \propto V^{1.07}$ for **CDI-F7**, thus in the ohmic region. From 4.6 to 6.6 V, the current density increases with applied voltage in the form of $J \propto V^{2.03}$ for **CDI-C8**; from 1.5 to 6.0 V, $J \propto V^{2.18}$ for **CDI-F7**, thus in the SCLC region. The charge carrier mobility derived from the SCLC region is 4.7 cm^2/Vs (at applied voltage 6.6 V) for **CDI-C8** and 6.6 cm^2/Vs (at applied voltage 6.0 V) for **CDI-F7**.

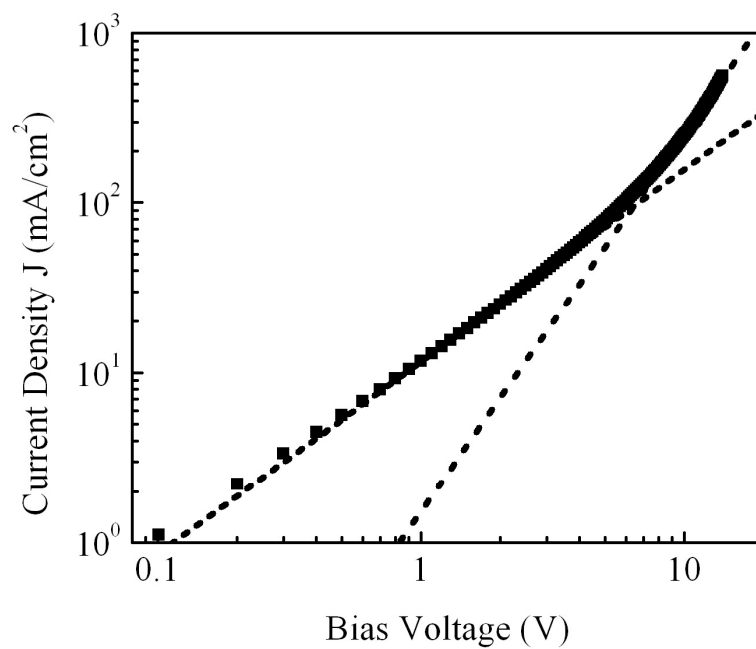
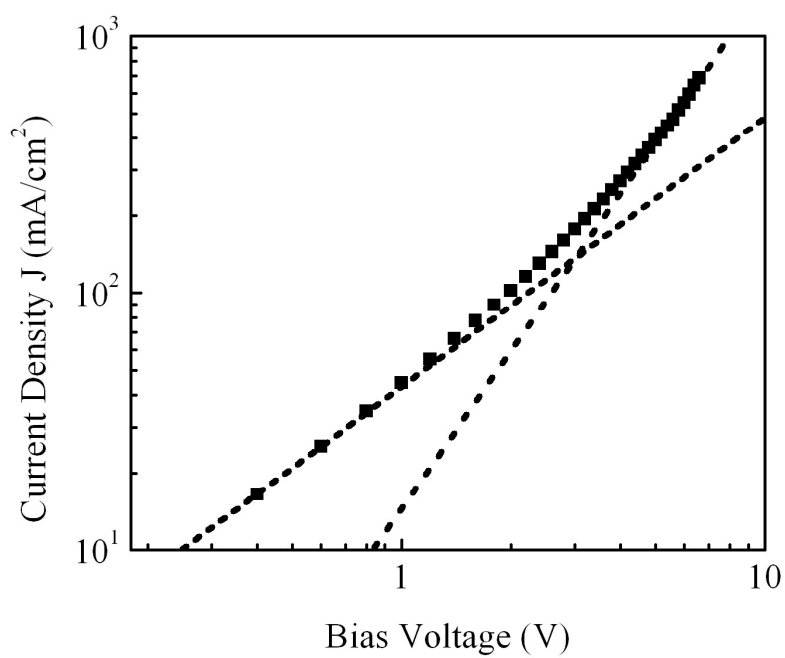


Figure 4.8 Double logarithmic plot of the current density (J) vs. applied voltage (V) for **CDI-C8** (top) and **CDI-F7** (bottom) in the device geometry: (+)ITO/CDI (5 μm)/Ag(-).

4.7 Concluding remarks

Binary side chains (perfluoroalkyl and alkyl groups) were incorporated into a coronene diimide liquid crystal (**CDI-F7**) to improve the mesophase ordering of the columnar discotic liquid crystal. Compared to the coronene diimide (**CDI-C8**) with alkyl groups only, **CDI-F7** has been demonstrated to have different electrical and mesophase properties. Firstly, the presence of the perfluoroalkyl groups close to the coronene diimide core makes compound **CDI-F7** more electron-deficient and consequently lowers the estimated LUMO energy level by 0.3 eV, compared to that for compound **CDI-C8**. This lower LUMO level can further stabilize the formed radical anion during the charge transport process. Moreover, due to this lower LUMO level, the energy barrier for electron injection from the cathode (Ag) into the material is lower for **CDI-F7** (ca. 0.6 eV) than that for **CDI-C8** (ca. 0.9 eV). Thus, charge injection process for **CDI-F7** is expected to be more efficient than that for **CDI-C8**; the effective mobility for **CDI-F7** should be larger than that for **CDI-C8**. Secondly, the amphiphilic nature of the binary side chains can, through fluorophobic interaction, enhance the ordering of the mesophase, as evidenced from: 1) the higher phase transition enthalpy associated with the thermal transition from the liquid crystalline phase to the isotropic phase for **CDI-F7** (12.7 kJ/mol) than that for **CDI-C8** (6.8 kJ/mol); 2) the more and sharper diffraction peaks in the low angle region of XRD for **CDI-F7** (six well resolved peaks) than that for **CDI-C8** (three peaks). As we have demonstrated in the previous chapters, higher mesophase order should lead to a higher charge carrier mobility for similar compounds with different side chains.

However, it is worth noting that the lattice parameter for **CDI-F7** ($a_0 = 38.4 \text{ \AA}$) is larger than that for **CDI-C8** ($a_0 = 29.7 \text{ \AA}$), possibly due to the longer length of the

perfluoroalkyl group.^{5d} The column density is 7.83×10^{12} columns/cm² and 13.09×10^{12} columns/cm² for **CDI-F7** and **CDI-C8**, respectively, assuming homeotropic arrangement of the columns. The reduction in the column density should, on the other hand, lead to a decrease in the effective mobility for **CDI-F7**.

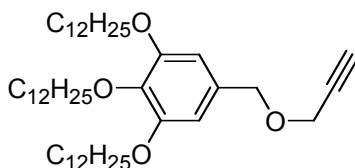
The SCLC measurements on these two compounds show higher charge carrier mobility in **CDI-F7** than that in **CDI-C8**. In terms of their structures, the only difference between these two compounds is that the imide groups in these two compounds are different: a segment of perfluoroalkyl group in **CDI-F7** vs. alkyl group in **CDI-C8**. Thus, it is reasonable to deduce that the difference in their charge carrier mobilities is mainly due to this structural difference which can give rise to different material properties as discussed above. However, one should be aware that how this structural difference could influence the reorganization energy and the intermolecular transfer integral is still unknown. Therefore, the higher effective charge carrier mobilities for **CDI-F7** (6.6 cm²/Vs) than for **CDI-C8** (4.7 cm²/Vs) may be the result of the interplay of several factors, including mesophase order, energy level, column density, reorganization energy and intermolecular transfer integral.

In addition, DSC measurements indicate that both materials form liquid crystalline phases slightly above room temperature during the heating process. After cooling the isotropic liquid to room temperature, XRD and POM show features of columnar discotic liquid crystals, suggesting that the liquid crystalline phases can be readily “supercooled” to room temperature, consistent with the phase transition temperatures from the cooling traces of the DSC measurements for both materials. Therefore, the SCLC characteristics of the materials measured at room temperature

represent that for the columnar discotic liquid crystalline phase, rather than that for the crystalline phase of the materials.

4.8 Experimental

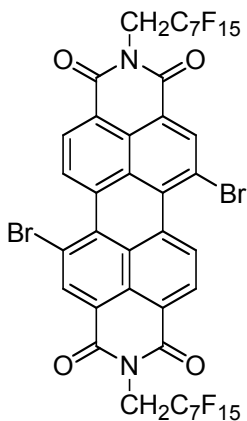
The general experimental information is similar to that described in Chapter 2, unless otherwise stated.



Synthesis of 3,4,5-Trisdodecyloxybenzyl propargyl ester

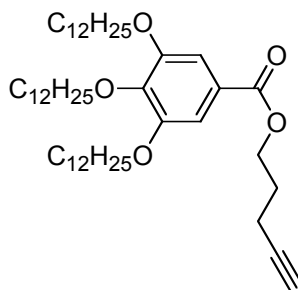
3,4,5-Tris-dodecylbenzyl alcohol⁶ (5.64 g, 8.53 mmol) was dissolved in dry DMF (60 mL). After 60% NaH (1.18 g, 29.5 mmol) was added under argon at room temperature, a white precipitate was formed and the mixture was stirred for 10 min. 80% Propargyl bromide toluene solution (14 mL, 125.7 mmol) was added and the reaction was further stirred at room temperature for 30 min. Additional 0.33 g NaH was added and the reaction was further stirred for 14 h. The reaction was quenched with water and was extracted with dichloromethane. After removal of solvent, the residue was purified by column chromatography eluting with 2:1 dichloromethane/hexane, 3.36 g (56%) of a yellow solid was obtained. ¹H NMR (500 MHz, CDCl₃): δ (ppm): 6.53 (s, 2H), 4.49 (s, 2H), 4.14 (d, *J* = 2.0 Hz, 2H), 3.95 (t, *J* = 6.5 Hz, 4H), 3.93 (t, *J* = 6.5 Hz, 2H), 2.44 (t, *J* = 2.0 Hz, 1H), 1.74 (m, 6H), 1.44 (m, 6H), 1.38 - 1.16 (m, 48H), 0.86 (t, *J* = 7.5 Hz, 9H). ¹³C NMR (125 MHz, CDCl₃): δ (ppm): 153.2, 137.9, 132.2, 106.6, 79.7, 74.6, 73.4, 71.9,

69.1, 56.9, 31.93, 31.92, 30.3, 29.75, 29.73, 29.69, 29.65, 29.61, 29.41, 29.39, 29.36, 26.13, 26.09, 22.7, 14.1 (7 carbon resonances were not observed presumably due to near equivalencies leading to overlap of resonances).



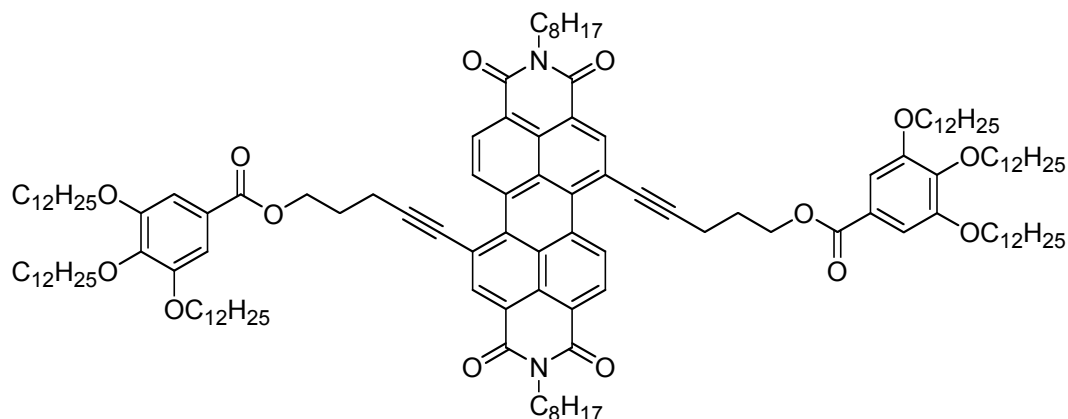
Synthesis of compound 12b

1,7-Bisbromoperylene dianhydride (0.93 g, 1.68 mmol) in NMP (20 mL) was sonicated for 30 min and acetic acid (0.645 g, 11.80 mmol) was added. And then 2,2,3,3,4,4,5,5,6,6,7,7,8,8,8-pentadecafluoro-octylamine (2.0 g, 4.86 mmol) in NMP (15 mL) was added. After the reaction mixture was heated at 85 °C under nitrogen for 8 h, it was cooled to room temperature. Methanol (150 mL) was added and a red precipitate was collected by filtration, which was then purified by column chromatography with chloroform, yielding 1.25 g (57%) of a red solid. ¹HNMR (500 MHz, CDCl₃): δ (ppm): 9.51 (d, *J* = 8.0 Hz, 2H), 8.97 (s, 2H), 8.75 (d, *J* = 8.0 Hz, 2H), 5.03 (m, 4H). HRMS (MALDI), *m/z*, calcd. for C₄₀H₁₀N₂O₄F₃₀Br₂ 1309.8528; found 1309.8528. Elemental analysis, calcd. for C₄₀H₁₀Br₂F₃₀N₂O₄, C 36.61, H 0.77, N 2.13; found C 36.68, H 0.66, N 2.07.



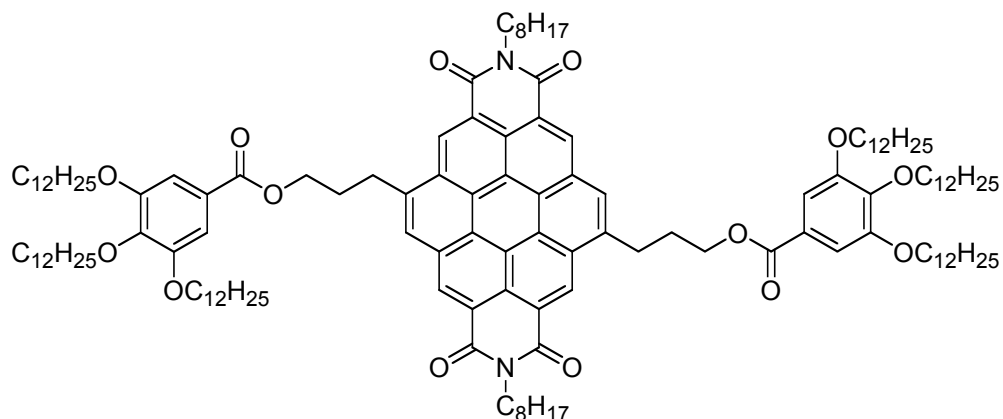
Synthesis of 3,4,5-Trisdodecyloxy benzoic acid pent-4-ynyl ester

3,4,5-Trisdodecyloxy-benzoyl chloride⁷ (1.56 g, 2.25 mmol) was dissolved in dry CH₂Cl₂ (20 mL), and then 4-dimethylpyridine (0.44 g, 3.59 mmol) was added. Pent-4-yn-1-ol (0.26 g, 3.10 mmol) was added via a syringe under nitrogen. The reaction was stirred for 80 min at room temperature. The solvent was removed and the residue was dissolved in hexane and was purified by column chromatography eluting with 5% ethyl acetate in hexane. 1.37 g (82%) of a white solid was obtained. ¹H NMR (300 MHz, CDCl₃): δ (ppm): 7.23 (s, 2H), 4.38 (t, *J* = 6.3 Hz, 2H), 3.98 (m, 6H), 2.34 (dt, *J*₁ = 7.2 Hz, *J*₂ = 2.4 Hz, 2H), 1.97 (m, 3H), 1.86 - 1.68 (m, 6H), 1.54 - 1.16 (m, 59H), 0.86 (m, 9H). ¹³C NMR (75 MHz, CDCl₃): δ (ppm): 166.2, 152.7, 142.3, 124.6, 108.0, 83.0, 73.5, 69.2, 69.0, 63.5, 32.0, 30.4, 29.8, 29.73, 29.70, 29.6, 29.5, 29.4, 27.8, 26.2, 26.1, 22.8, 15.5, 14.2. (10 carbon resonances were not observed presumably due to near equivalencies leading to overlap of resonances). HRMS (MALDI), *m/z* calcd. for C₄₈H₈₄O₅, 740.6319; found (M+H) 741.6392. Elemental analysis, calcd. for C₄₈H₈₄O₅, C 77.78, H 11.42; found C 77.54, H 11.47.



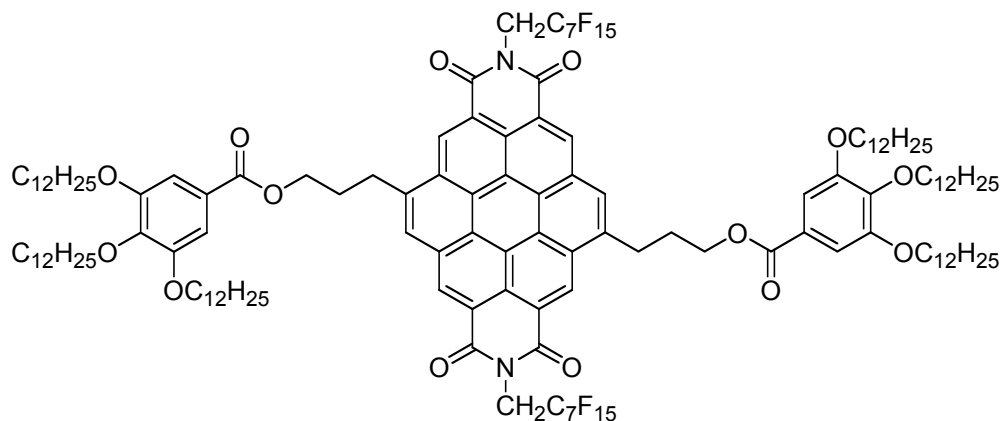
Synthesis of compound 13a

N,N'-Dioctyl-1,7-bisbromoperylene diimide⁸ (0.42 g, 0.54 mmol) was dissolved in toluene (30 mL) and triethyl amine (6 mL), and the resulting solution was deoxygenated for 10 min with nitrogen. Tetrakis(triphenylphosphino) palladium(0) (0.06 g, 0.05 mmol) and copper(I) iodide (0.015 g, 0.17 mmol) were added and the mixture was further deoxygenated for 10 min. 3,4,5-Trisdodecyloxy benzoic acid pent-4-ynyl ester (1.20 g, 1.62 mmol) dissolved in toluene (10 mL) deoxygenated with nitrogen was added. The reaction was heated at 60 °C under nitrogen for 14 h. After cooling to room temperature, the reaction was poured into 2 N HCl solution. The organic phase was separated and was washed over water. The solvent was removed and the residue was purified by column chromatography eluting with CH₂Cl₂. 1.01 g (89%) of a red solid was obtained. ¹H NMR (500 MHz, CDCl₃): δ (ppm): 10.07 (d, *J* = 8.5 Hz, 2H), 8.65 (s, 2H), 8.61 (d, *J* = 8.0 Hz, 2H), 7.21 (s, 4H), 4.55 (t, *J* = 6.0 Hz, 4H), 4.16 (t, *J* = 8.0 Hz, 4H), 3.88 (t, *J* = 6.5 Hz, 8H), 3.82 (t, *J* = 6.5 Hz, 4H), 2.86 (t, *J* = 6.5 Hz, 4H), 2.25 (m, 4H), 1.8 - 1.6 (m, 16H), 1.5 - 1.1 (m, 128H), 0.87 (m, 24H). HRMS (MALDI), *m/z* calcd. for C₁₃₆H₂₀₆N₂O₁₄, 2003.5672; found (*M*+*H*), 2004.5701. Elemental analysis, calcd. for C₁₃₆H₂₀₆N₂O₁₄, C 78.04, H 9.92, N 1.34; found C 77.82, H 9.97, N 1.50.



Synthesis of CDI-C8

Compound 13a (0.72 g, 0.34 mmol) was dissolved in toluene (50 mL), and the resulting solution was heated to 80 °C under nitrogen. DBU (0.2 mL) was added via a syringe. The reaction was then heated to 100 °C under nitrogen for 20 h. After cooling to room temperature, the reaction mixture was poured into 2 N HCl solution. The organic layer was separated, and the solvent was removed. The residue was purified by column chromatography eluting first with CH₂Cl₂, then with 5% ethyl acetate in CH₂Cl₂. 0.58 g (80%) of a yellow solid was obtained. ¹H NMR (500 MHz, CD₂Cl₂): δ (ppm): 9.61 (s, 2H), 9.34 (s, 2H), 8.60 (s, 2H), 6.89 (s, 4H), 4.60 (t, *J* = 6.0 Hz, 4H), 4.44 (t, *J* = 8.0 Hz, 4H), 3.87 (t, *J* = 6.0 Hz, 4H), 3.64 (m, 12H), 2.62 (m, 4H), 1.94 (m, 4H), 1.7 - 1.1 (m, 140H), 1.0 - 0.7 (m, 24H). HRMS (MALDI), *m/z* calcd. for C₁₃₆H₂₀₆N₂O₁₄, 2091.5469; found (M+H) 2092.5543. Elemental analysis, calcd. for C₁₃₆H₂₀₆N₂O₁₄, C 78.04, H 9.92, N 1.34; found C 77.85, H 9.88, N 1.47.



Synthesis of CDI-F7

Compound 12b (0.77 g, 0.59 mmol) was suspended in toluene (40 mL) and triethyl amine (10 mL), and the resulting solution was deoxygenated with nitrogen for 15 min. Tetrakis(triphenylphosphino)palladium(0) (0.075 g, 0.065 mmol), copper(I) iodide (0.023 g, 0.12 mmol) and then 3,4,5-trisdodecyloxy benzoic acid pent-4-ynyl ester (1.31 g, 1.77 mmol) were added successively. The reaction was heated at 65 °C for 18 h. TLC indicated complete consumption of starting material and gave two major spots; one is red and the other is yellow green, suggesting that the formed acetylene compound was partially transformed into the corresponding coronene compound. After cooling to room temperature, the reaction mixture was poured into 2 N HCl solution. The organic layer was separated and the solvent was removed. The residue was purified by column chromatography to get a mixture of the acetylene-substituted intermediate and the coronene diimide.

The above-obtained material was dissolved in toluene (90 mL) and was heated to 100 °C under nitrogen. DBU (0.35 mL) was added and the reaction was heated at 100 °C for 19 h under nitrogen. After cooling to room temperature, the reaction mixture was poured into 2 N HCl solution. The organic layer was separated and the solvent was removed. The residue was purified by column chromatography eluting with chloroform,

0.62 g (37%) of a red solid was obtained. ^1H NMR (500 MHz, CDCl_3): δ (ppm): 9.89 (s, 2H), 9.64 (s, 2H), 8.84 (s, 2H), 6.89 (s, 4H), 5.31 (t, $J = 15.7$ Hz, 4H), 4.60 (t, $J = 6.0$ Hz, 4H), 3.94 (m, 4H), 3.75 (t, $J = 6.5$ Hz, 4H), 3.69 (t, $J = 6.5$ Hz, 8H), 2.66 (m, 4H), 1.8 - 1.55 (m, 12H), 1.5 - 1.1 (m, 108H), 0.83 (m, 18H). Elemental analysis, calcd. for $\text{C}_{136}\text{H}_{176}\text{F}_{30}\text{N}_2\text{O}_{14}$, C 62.04, H 6.74, N 1.06; found C 61.98, H 6.69, N 1.10.

4.9 References

1. (a) Schwaebisch, D.; Wille, S.; Hein, M.; Miethchen, R. *Liquid Cryst.* **2004**, *31*, 1143-1150. (b) Nishikawa, E.; Yamamoto, J.; Yokoyama, H. *Chem. Lett.* **2001**, *2*, 94-95. (c) Percec, V.; Glodde, M.; Bera, T. K.; Miura, Y.; Shiyanoskaya, I.; Singer, K. D.; Balagurusamy, V. S. K.; Heiney, P. A.; Schnell, I.; Rapp, A.; Spiess, H.-W.; Hudson, S. D.; Duan, H. *Nature*, **2002**, *419*, 384-387. (d) Percec, V.; Johansson, G.; Ungar, G.; Zhou, J. *J. Am. Chem. Soc.* **1996**, *118*, 9855-9866. (e) Li, Z.; Kesselman, E.; Talmon, Y.; Hillmyer, M. A.; Lodge, T. P. *Science*, **2004**, *306*, 98-101.
2. Terasawa, N.; Monobe, H.; Kiyohara, K.; Shimizu, Y. *Chem. Comm.* **2003**, *14*, 1678-1679.
3. (a) Katz, H. E.; Lovinger, A. J.; Johnson, J.; Kloc, C.; Siegrist, T.; Li, W.; Lin, Y.-Y.; Dodabalapur, A. *Nature* **2000**, *404*, 478-480. (b) Katz, H. E.; Johnson, J.; Lovinger, A. J.; Li, W. *J. Am. Chem. Soc.* **2000**, *122*, 7787-7792. (c) Katz, H. E.; Siegrist, T.; Schön, J. H.; Kloc, C.; Batlogg, B.; Lovinger, A. J.; Johnson, J. *Chem. Phys. Chem.* **2001**, *3*, 167-172.
4. Jones, B. A.; Ahrens, M.; Yoon, M.-H.; Facchetti, A.; Marks, T. J.; Wasielewski, M. R. *Angew. Chem. Int. Ed.* **2004**, *43*, 6363-6366.
5. (a) Facchetti, A.; Mushrush, M.; Katz, H. E.; Marks, T. J. *Adv. Mater.* **2003**, *15*, 33-38. (b) Facchetti, A.; Yoon, M.-H.; Stern, C. L.; Katz, H. E.; Marks, T. J. *Angew. Chem. Int. Ed.* **2003**, *42*, 3900. (c) Yoon, M.-H.; Dibeneditto, S. A.; Facchetti, A.; Marks, T. J. *J. Am. Chem. Soc.* **2005**, *127*, 1348-1349. (d) Facchetti, A.; Mushrush, M.; Yoon, M.-H.; Hutchison, G. R.; Ratner, M. A.; Marks, T. J. *J. Am. Chem. Soc.* **2004**, *126*, 13859-13874. (e) Facchetti, A.; Yoon, M.-H.; Stern, C. L.; Hutchison, G. R.; Ratner, G. R.; Marks, T. J. *J. Am. Chem. Soc.* **2004**, *126*, 13480-13501.
6. Poon, K.-W.; Liu, W.; Chan, P.-K.; Yang, Q.; Chan, T.-W. D.; Mak, T. C. W.; Ng, D. K. P. *J. Org. Chem.* **2001**, *66*, 1553-1559.
7. (a) Percec, V.; Schlueter, D.; Ronda, J. C.; Johansson, G.; Ungar, G.; Zhou, J. P. *Macromolecules* **1996**, *29*, 1464-1472. (b) Yeardley, D. J. P.; Ungar, G.; Percec, V.; Holerca, M. N.; Johansson, G.; *J. Am. Chem. Soc.* **2000**, *122*, 1684-1689.
8. Rohr, U.; Kohl, C.; Müllen, K.; van de Craats, A.; Warman, J. *J. Mater. Chem.* **2001**, *11*, 1789-1799.

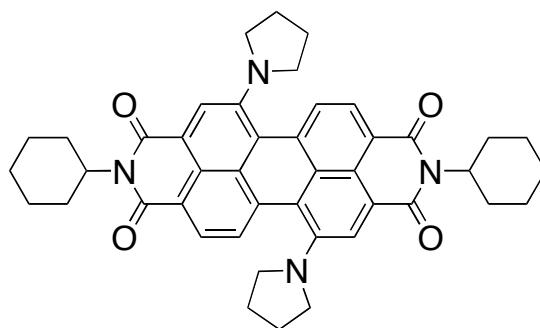
CHAPTER 5

DONOR-SUBSTITUTED PERYLENE DIIMIDES

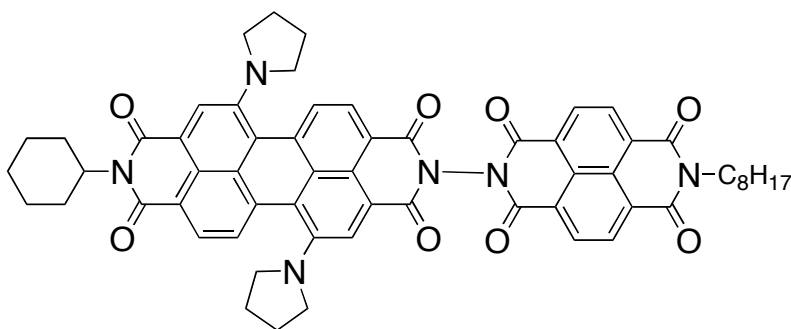
5.1 Introduction

Perylene diimides and their derivatives have been widely used in multifunctional supramolecular arrays that employ photo-induced charge transfer¹ or energy transfer² processes, owing to their relatively low reduction potentials; outstanding thermal, chemical and optical stabilities; and tunable absorption and emission properties.³ These supramolecular arrays, often having elaborately constructed functional motifs and well controlled self-assembly properties, are used to mimic photosynthetic processes for potential applications in molecular electronics, such as switches, wires, and solar cells.⁴

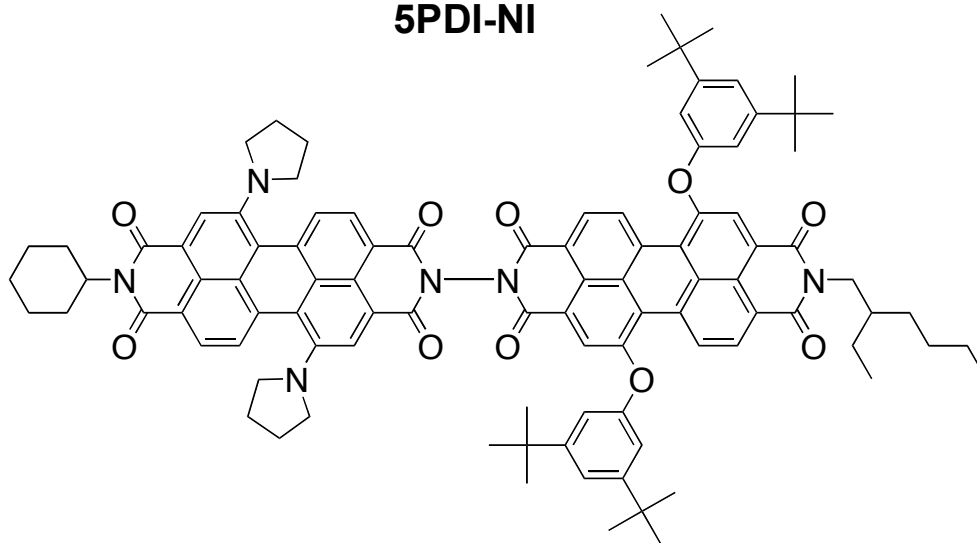
The Wasielewski group has developed green perylene diimide chromophores (Figure 5.1a) with cycloalkylamino groups attached to the 1 and 7 positions of perylene diimides.^{5,6} These chromophores have similar photophysical and redox properties to that of chlorophyll *a*, but are more photochemically robust and can be easily functionalized.⁶ The green chromophore **SPDI** has been incorporated into a variety of biomimetic electron donor - acceptor systems (Figure 5.1).



5PDI



5PDI-NI



5PDI-PDI

Figure 5.1 Molecular structures of green chromophore **5PDI** and the D-A biomimetic systems **5PDI-NI** and **5PDI-PDI**. (From ref. 6)

One of the remarkable findings with the green chromophore is that in its cofacial and linear dimers (Figure 5.2), the green chromophore functions as both the electron donor and the electron acceptor.⁷ Quantitative charge separation occurs in toluene with $\tau = 0.52$ ps followed by charge recombination to the ground state with $\tau = 220$ ps for the cofacial dimer; charge separation and charge recombination occur with $\tau = 55$ ps and with $\tau = 99$ ps respectively for the linear dimer in 2-methyltetrahydrofuran (MTHF).

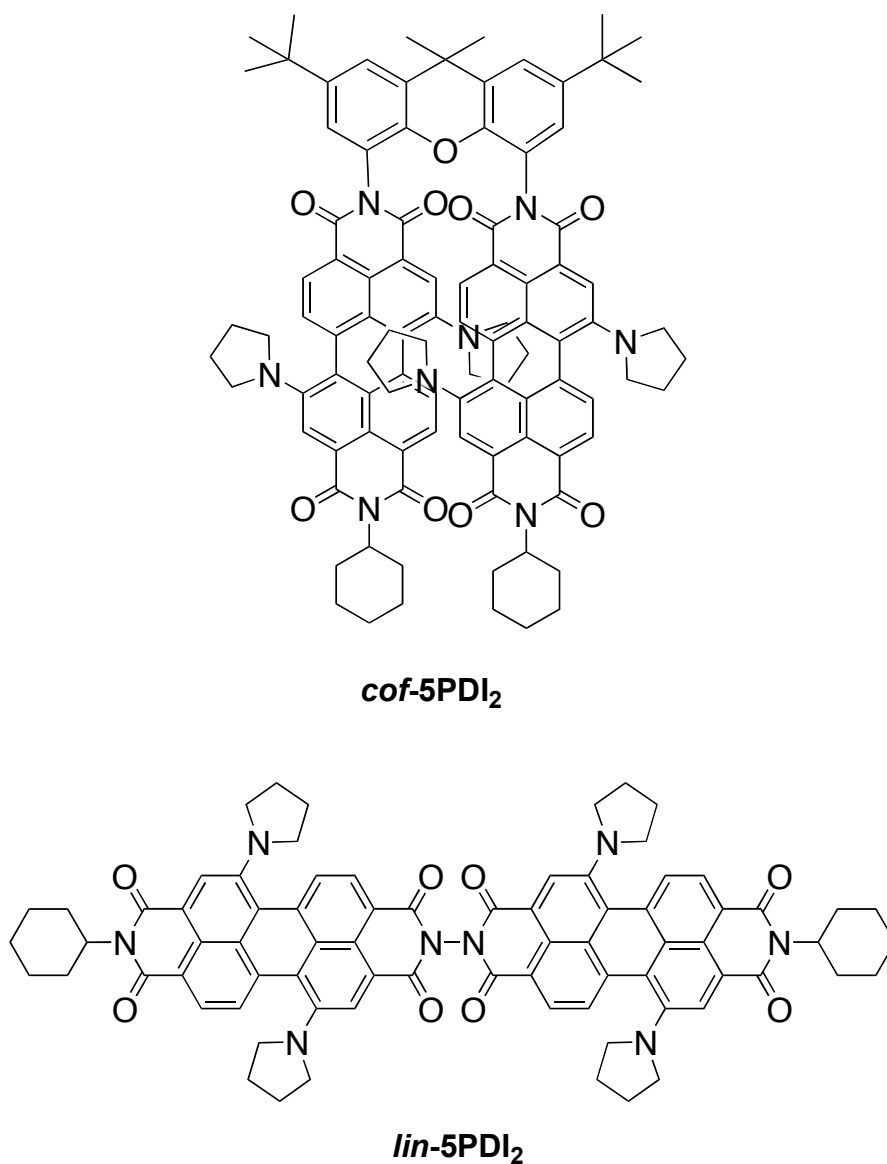


Figure 5.2 Cofacial and linear dimers of **5PDI**. (From ref. 7)

Based on the cofacial dimer model, the Wasielewski group recently reported ultrafast charge separation within non-covalent self-assembled aggregates of tridodecyloxyphenyl-substituted green chromophore **5PDI-TAP** (Figure 5.3).⁸ Femtosecond transient absorption spectroscopy study on the **5PDI-TAP** *H*-aggregates self-assembled in low polarity solvent methylcyclohexane revealed a charge-transfer process occurring with $\tau \leq 150$ fs between adjacent stacked molecules followed by charge recombination with $\tau = 860$ ps.

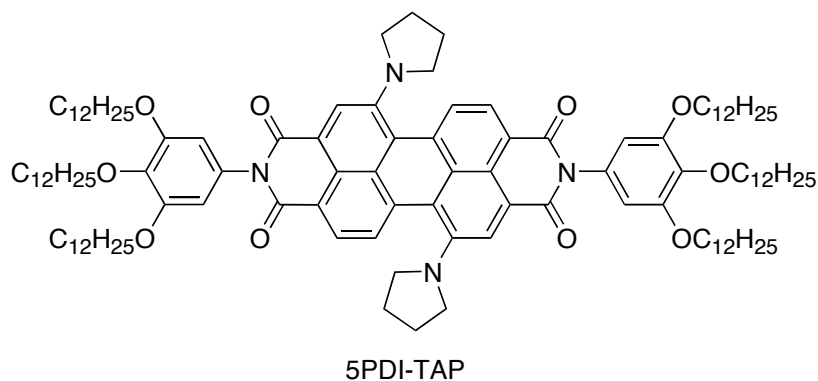


Figure 5.3 **5PDI-TAP** used for charge-transfer studies in aggregates. (From ref. 8)

Recently an interesting artificial photosynthetic array **5PDI-PDI₄** (Figure 5.4) that combines energy and electron transfer was reported.⁹ **5PDI-PDI₄** with four **PDI** chromophores covalently attached to the **5PDI** core, has been shown to self-assemble into dimers in toluene and THF. First, energy transfer takes place within 21 ps from the surrounding **PDI**s to the **5PDI** core, which is followed by electron transfer between the

stacked non-covalent **5PDI** dimers to produce charge separation within 7 ps and charge recombination within 420 ps.⁹

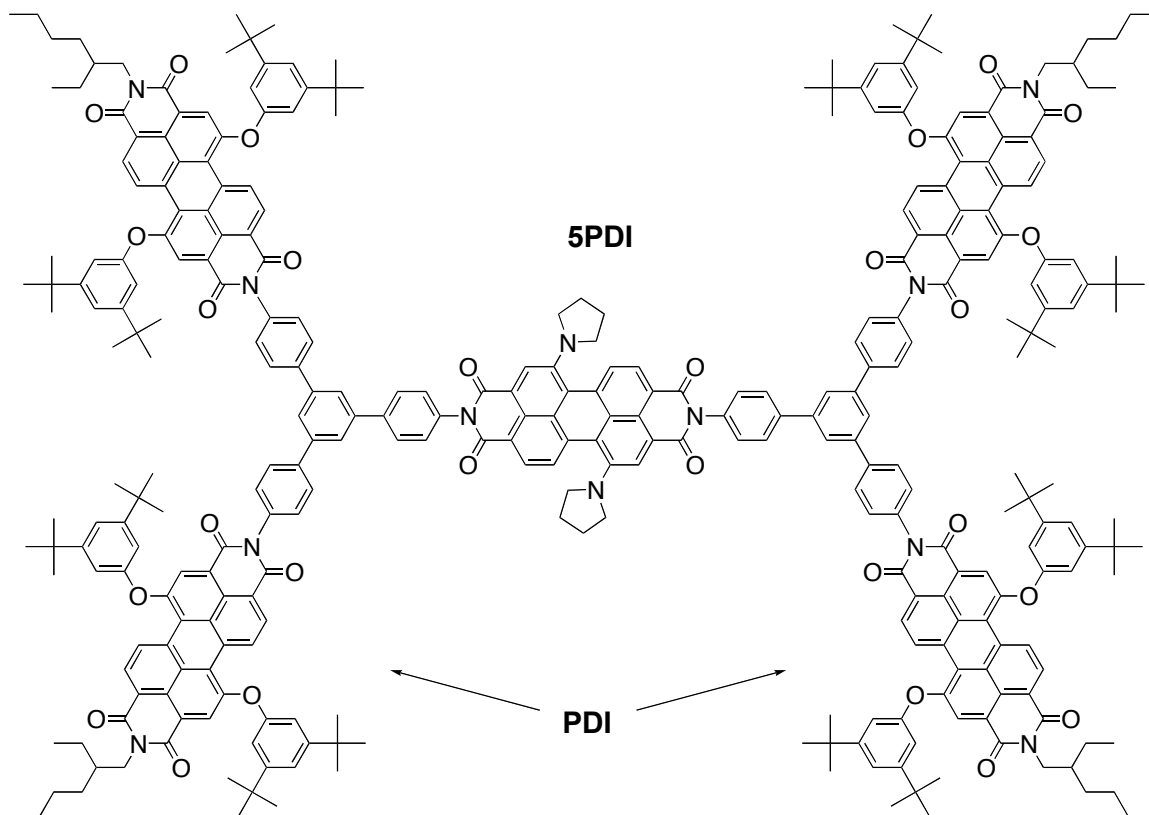


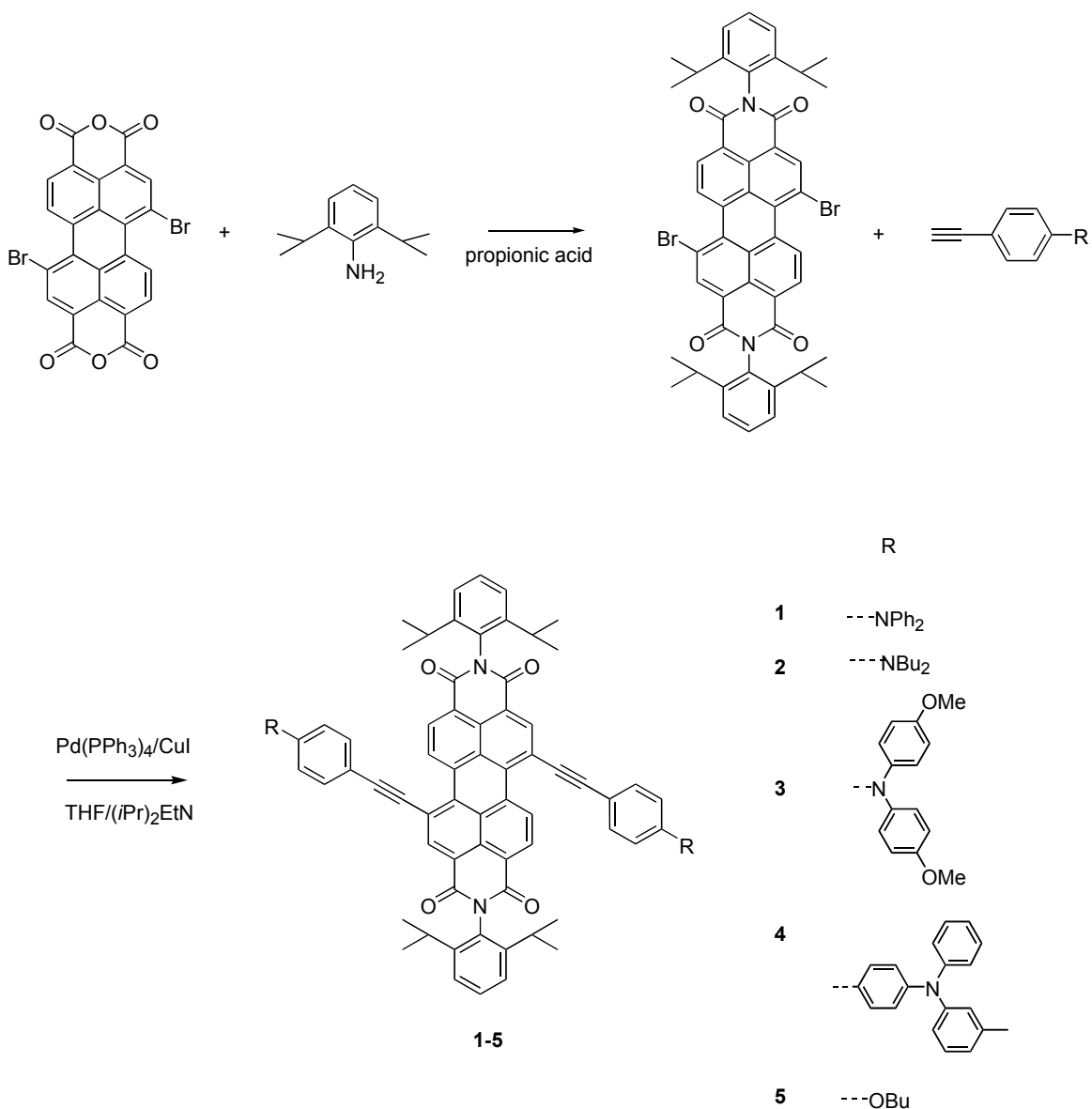
Figure 5.4 An artificial photosynthetic array combining energy and charge transfer. (From ref. 9)

5PDI has been demonstrated to have high extinction coefficients over a wide spectral range and has been employed in various charge-transfer and/or energy transfer systems. We were interested in investigating similar chromophores for their potential applications in solar cells. For solar cells using organic semiconductors or dyes, one of the limitations is that many organic semiconductors or dyes can have strong absorption

only in the visible region of the solar spectrum.¹⁰ While a large fraction of solar energy is in the near-infrared (NIR) region of the solar spectrum. Expansion of absorption into the NIR region to cover 350-900 nm can potentially cover 46% of the solar energy.^{10,11} However, such organic semiconductors or dyes with a wide absorption spectrum are usually difficult to achieve. By modifying **5PDI** through conjugation extension between the donor groups and the perylene core at the 1 and 7 positions, we attempted to synthesize perylene diimide chromophores with the absorption further shifted into the NIR region of the solar spectrum and to modulate the electron-transfer and charge-recombination processes. This chapter focuses on the synthesis, characterization of the donor-substituted chromophores for their possible applications in photovoltaic cells.

5.2 Synthesis

Various 1,7-bis-substituted perylene diimide derivatives **1 - 5** were synthesized by the palladium-catalyzed Sonogashira¹² coupling reaction between the 1,7-dibromoperylene diimide with the corresponding terminal acetylenes giving good to excellent yields (Scheme 5.1). 1,7-Dibromoperylene dianhydride was obtained from bromination of perylene tetracarboxylic dianhydride in concentrated sulfuric acid according to a reported synthetic procedure.¹³ Condensation of the dianhydride with 2,6-diisopropylaniline in refluxing propionic acid provided the 1,7-dibromo-perylene diimides.¹⁴ The terminal acetylenes were generally synthesized by cross-coupling reactions between the corresponding halides with trimethylsilylacetylene followed by deprotection of the silyl group.



Scheme 5.1 Synthesis of donor-substituted perylene diimides **1 - 5**.

5.3 UV-Vis absorption properties

Compounds **1 - 3** each display three strong absorption bands covering a wide spectral range of UV, visible and NIR (Figure 5.5). The tail of lowest energy absorption band of compound **3** extends to 1.0 μm . The peak position of the lowest energy band gradually shifts to the longer wavelength as the electron donating ability of the donors

increases from compound **1** to compound **3**. Compared to their parent perylene diimides,^{3d} these three derivatives have a similar absorption maximum around 510 nm with less vibronic features of the perylene skeleton. It has been found that when perylene diimides are substituted at the 1,7 bay positions, the two naphthalene units of the perylene core are no longer coplanar, but are twisted at various degrees depending upon the size of the substituents.^{15,16} For example, the loss of planarity is true even with the cyano group that causes a twist of approximately 5 degree for the perylene core.¹⁶ This twist may account for the loss of some fine vibronic structures in the 1,7-disubstituted perylene diimides. It is also noticeable that these compounds have high extinction coefficients, comparable to that of the ruthenium complex dyes used in Grätzel solar cells.¹⁷ Compared with **5PDI** ($\lambda_{\text{max}} = 686 \text{ nm}$),⁶ the λ_{max} of **2** (706 nm) is red-shifted by 20 nm in toluene; a similar red shift is also observed for the second lowest energy band.

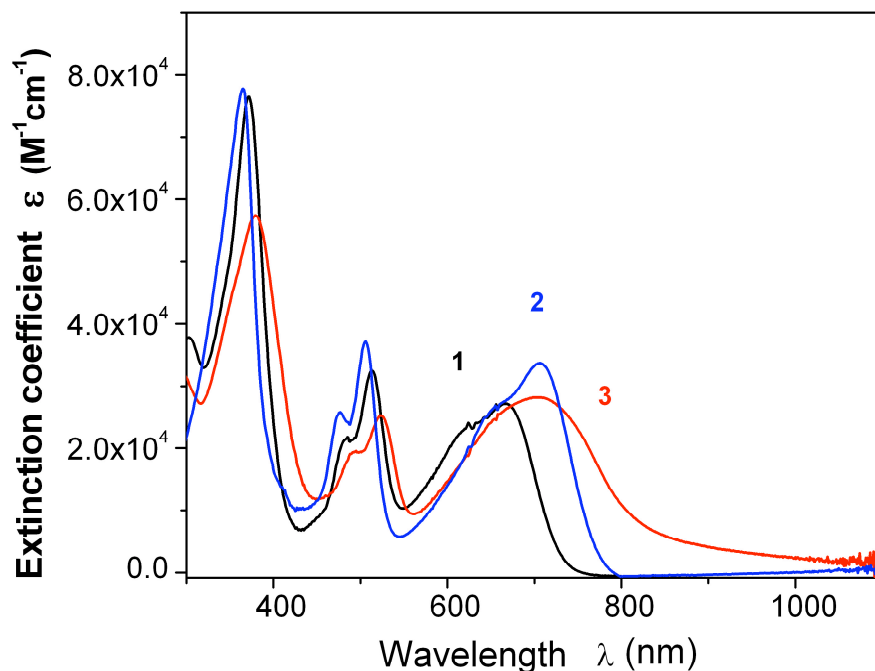


Figure 5.5 Absorption spectra of compounds **1** - **3** in toluene (concentration 10^{-6} to 10^{-5} M).

In order to further understand the nature of the lowest energy band, compound **4** with longer side arms and compound **5** with weaker donor moieties were synthesized. The lowest energy band of compound **4** is surprisingly shifted to the shorter wavelength by more than 50 nm (Figure 5.6) when compared to that of compound **1**. Similar blue-shift with increasing conjugation length has also been previously observed in D-A substituted oligo(phenylenevinylene)s.¹⁸ This blue-shift may be caused by the longer distance between the donor and the acceptor, making the charge-transfer process weaker and at the same time the twist between the two phenylene units may further decouple the electronic communication between the donor and the acceptor. When the amino donor group in compound **2** is replaced by a weaker donor group, such as the butoxy group in

compound **4**, a large blue shift of more than 100 nm is observed (Figure 5.7). This substantial spectral change may suggest that the lowest energy band of compound **2** at least has some charge-transfer character, which partially leads to the formation of the long wavelength absorption in compound **2**.

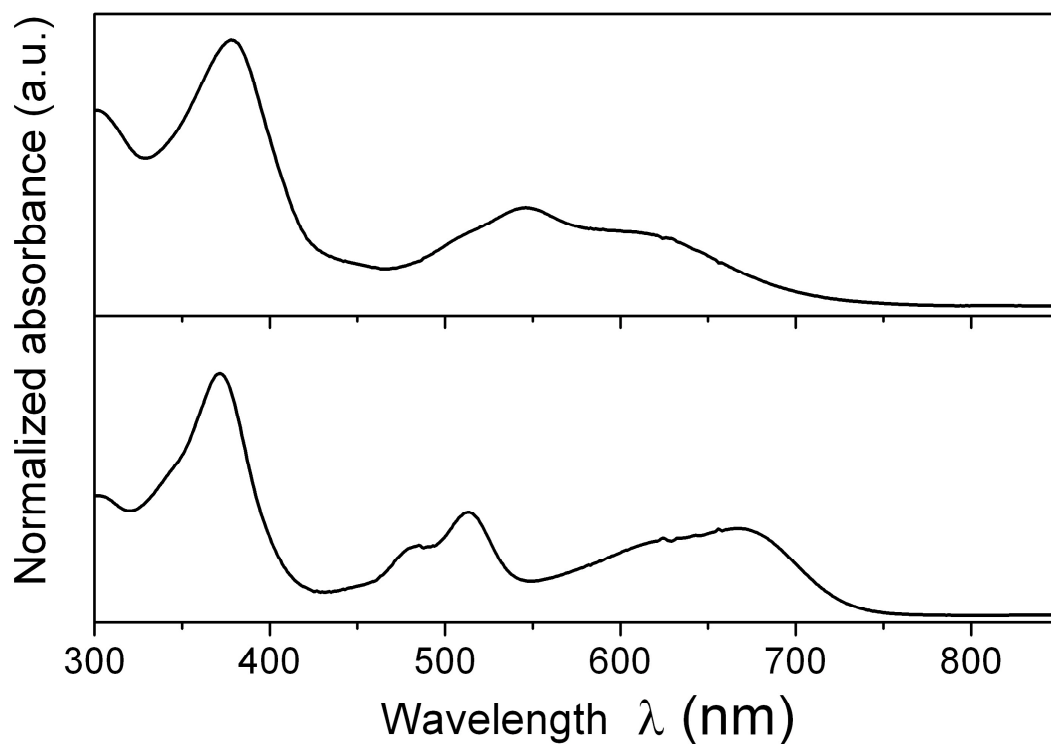


Figure 5.6 Normalized absorption spectra of compound **4** (top) and compound **1** (bottom) in toluene.

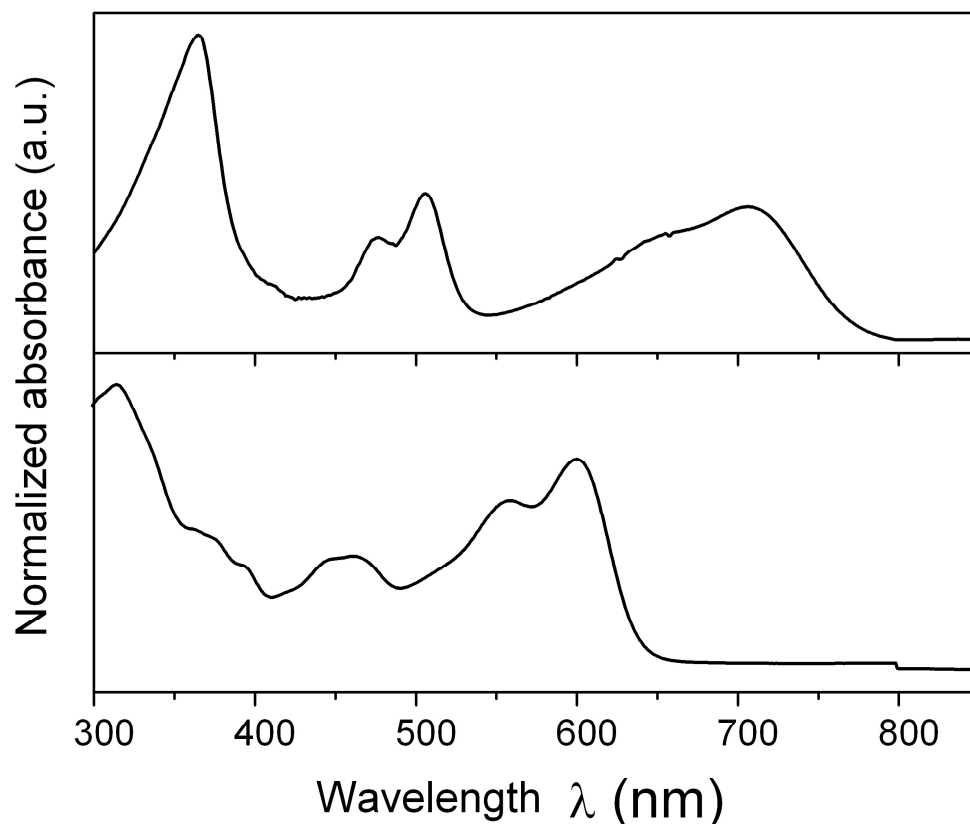


Figure 5.7 Normalized absorption spectra of compound **2** (top) and compound **5** (bottom) in toluene.

5.4 Transient absorption properties

Transient absorption spectra (by David McCamant, Wasielewski group) provide further information on the nature of the electronic transitions of these donor-substituted compounds. The transient absorption spectra of compound **2** after excitation at 400 nm (Figure 5.8), show bleaching of two ground-state bands corresponding to the ground state absorption of the second lowest energy band and the lowest energy band. The bleaching centered at 508 nm decays within 824 ± 19 ps. For the second bleaching, the major feature centered at 715 nm and the minor feature centered at 657 nm have different decay times, 1000 ± 47 ps and 878 ± 19 ps respectively (Figure 5.9). The different decay times

for these two wavelengths within the apparently “same” absorption band clearly indicates that the “lowest energy band” actually has two different features, in contrast to the same decay time (4.5 ns) of the two bleaching peaks (major 700 nm and minor 625 nm) in **5PDI**. The formation of the band centered at 778 nm appears within 8.9 ± 0.3 ps at the familiar position for PDI^- ,^{7,8} with a decay time of 870 ± 11 ps. In addition, there is another positive feature around 550 nm. It remains unclear whether or not this is another transient absorption band from PDI^- or the transient absorption band from the radical cation of the amine. Compound **1** shows similar transient absorption features with charge separation within 12.6 ± 0.8 ps and charge recombination of 2121 ± 41 ps. The substantially longer decay time of the PDI^- may be possibly related to the more stable radical cations formed on the triarylamine motifs, which may live longer than in compound **2** before the charges recombine. Compound **4** shows faster charge separation (9.6 ± 0.3 ps) and recombination (752 ± 10 ps) than for compound **1**, although the donors are further away from the perylene diimide core. The poor solubility of **3** prevents its measurement in toluene; much faster charge separation (0.8 ± 0.2 ps) and recombination (1.4 ± 0.2 ps) are observed in THF solution compared to the other compounds in toluene, due to the higher dielectric constant of THF compared to toluene.

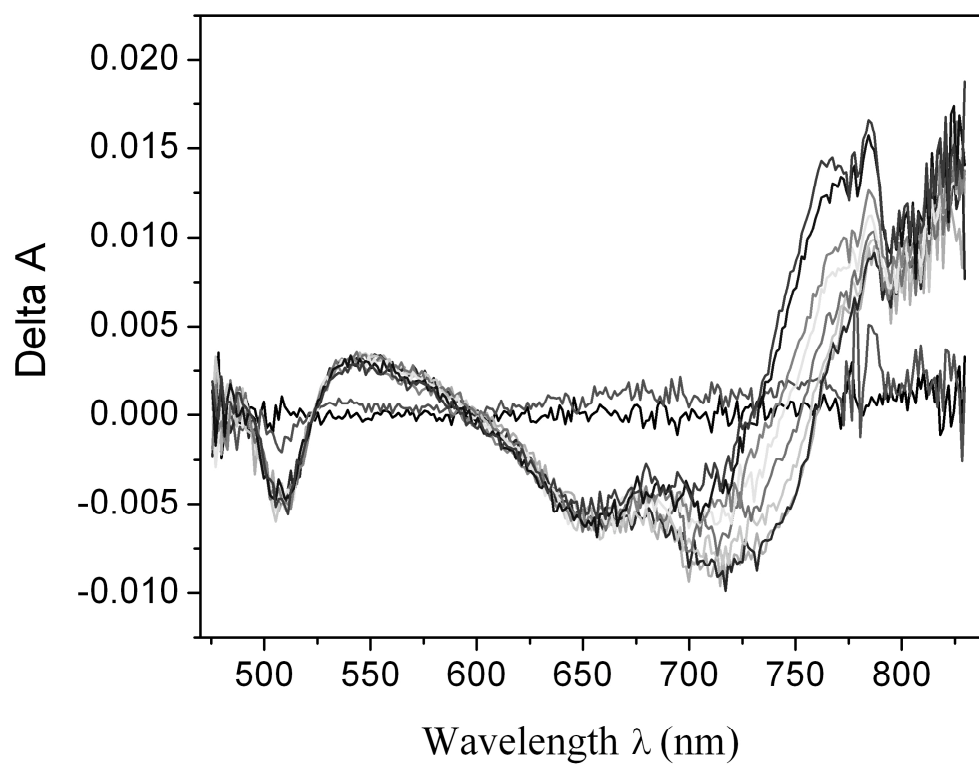


Figure 5.8 Transient absorption spectra of compound **2** in toluene after excitation at 400 nm.

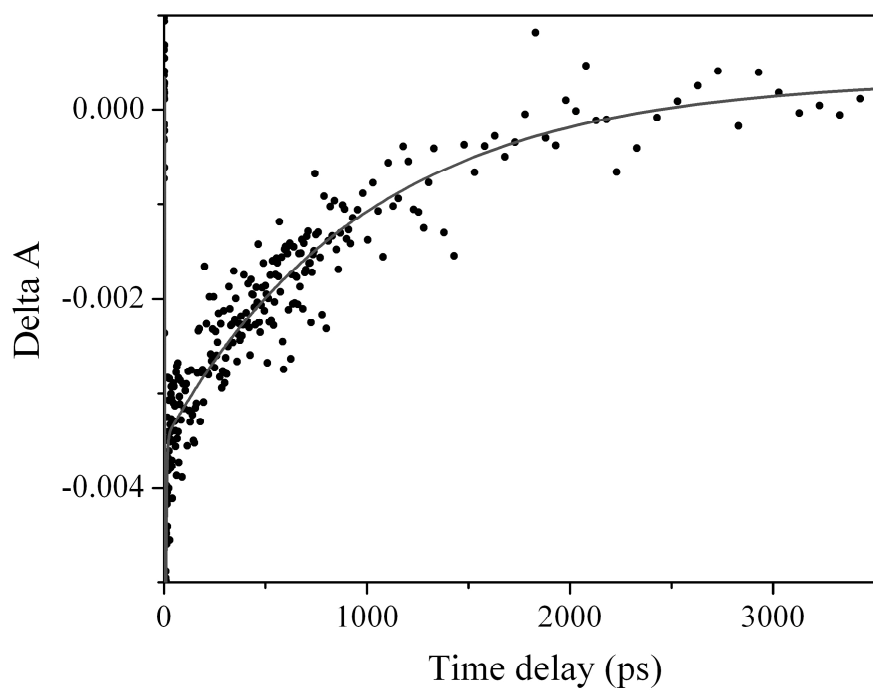
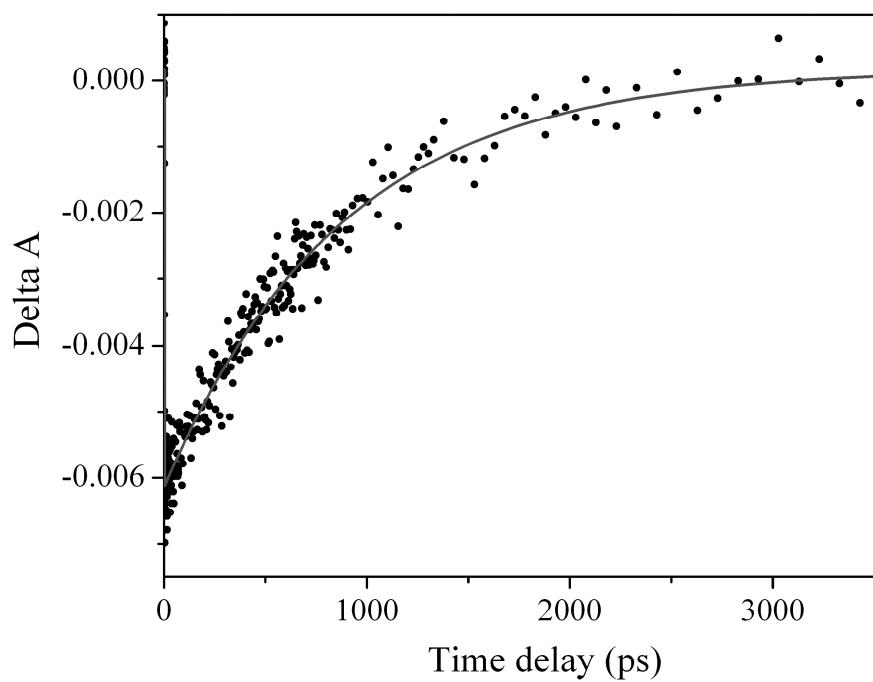


Figure 5.9 Decay of the excited states of compound **2** at 657 nm (top) and 715 nm (bottom) in toluene.

5.5 Electrochemical properties

The cyclic voltammogram of **2** (Figure 5.10) consists of two successive reversible one-electron reduction waves and one reversible oxidation wave with the current almost twice of that for the reduction. The two reductions most likely occur on the two electron-deficient imide groups and the repulsion between the formed radical anions makes the second reduction more negative.¹⁹ The oxidation may occur almost simultaneously on the two amino positions separated by a sufficiently long distance such that the resulting radical cations do not interact each other appreciably. Other compounds show similar electrochemical behavior and their reduction potentials are similar to that of the unsubstituted perylene diimides, indicating that substitution at the 1 and 7 positions of the perylene core does not affect the LUMO level significantly in these compounds; the ease with which the oxidation occurs corresponds to the electron donating ability of the donors (Table 5.1)

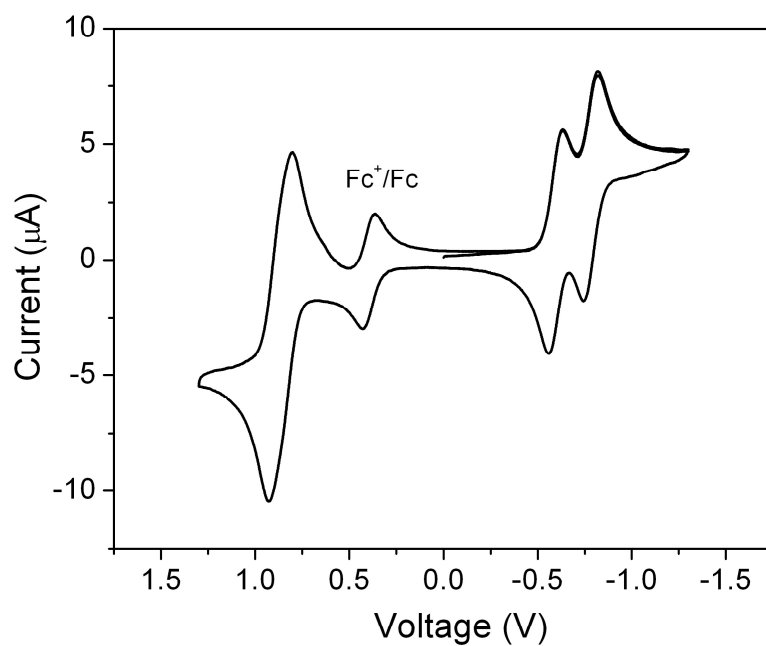


Figure 5.10 Cyclic voltammogram of compound **2** with Fc^+/Fc as the internal standard, scan rate = 25 mV/s.

Table 5.1 Electrochemical data of donor-substituted compounds **1** – **4** vs Fc^+/Fc .

	X^+/X (V)	X/X^- (V)	X^-/X^{2-} (V)
1	0.60	-0.97	-1.17
2	0.47	-0.99	-1.18
3	0.37	-0.99	-1.19
4	0.49	-0.92	-1.12

5.6 Concluding remarks

We have shown that by extending the conjugation between the donors and the perylene core, both the absorption spectrum and the charge-transfer process can be finely tuned in the donor-substituted compounds **1 - 4**.

Compared to **5PDI**, the absorption of compounds **1 - 3** can further extend into the NIR region with high extinction coefficients. Chromophores that can have strong absorption in the NIR region have attracted much attention, because a significant fraction of solar energy is in the NIR region of the solar spectrum. Currently used efficient photosensitizers in Grätzel solar cells are mainly ruthenium complexes.¹¹ The highly absorbing perylene-based chromophores **1 - 3** will enrich the library of the chromophores used in Grätzel solar cells. Moreover, the method used here for the design of these chromophores combines both electron-transfer and conjugation extension. This may be a useful method for the design of new chromophores that can have strong absorption in the NIR. In addition, perylene-based materials provide further functionalizations at the imide positions. Carboxylic or phosphonic acid groups can be incorporated into these chromophores such that the chromophores can be attached tightly to the surface of porous oxides.

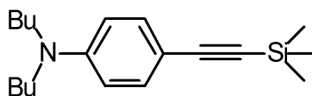
Another interesting finding about these chromophores is that compared to the ultrafast charge-transfer process, the charge-recombination process is significantly slower. For example, the charge-transfer process for compound **1** finishes within 12.6 ± 0.8 ps, while the charge recombination occurs within 2121 ± 41 ps. One of the limitations for organic solar cells, especially for heterojunction solar cells, is that the excitons can recombine in the bulk before they reach the heterojunction for dissociation. Thereby, it is desirable to have a long exciton lifetime such that the excitons can have a large diffusion

length and consequently this may allow for thicker thin films to be used to harness more solar energy.

In summary, the high extinction coefficients, wide absorption spectra and the long-lived charge-separation states make these chromophores promising candidates for photovoltaic applications.

5.7 Experimental

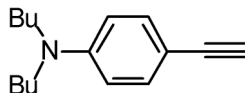
General experimental information is similar as in Chapter 2 unless otherwise stated.



Synthesis of dibutyl-[4-(trimethyl-silanylethynyl)-phenyl]-amine

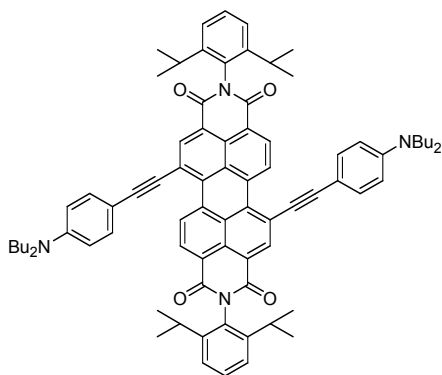
To a solution of (4-iodo-phenyl)-dibutyl-amine (2.53 g, 7.6 mmol) in triethylamine (30 mL) deoxygenated with nitrogen, were added copper(I) iodide (84 mg, 0.44 mmol) and tetrakis(triphenylphosphine) palladium(0) (0.2 g, 0.17 mmol) successively. The mixture was further deoxygenated for 10 min and trimethylsilylacetylene (1.2 mL, 8.3 mmol) was added. The reaction was heated at 40 °C under nitrogen for 16 h. After cooling the reaction mixture to room temperature, a precipitate was filtered off and was washed thoroughly with hexane. The solvent was removed and the residue was purified by column chromatography eluting with hexane, then 5:95 ethyl acetate/hexane. After removal of solvent, 2.06 g (90%) of a brown oil was obtained. ^1H NMR (300 MHz, CDCl_3), δ (ppm): 7.29 (d, $J = 9$ Hz, 2H), 6.50 (d, $J = 9$

Hz, 2H), 3.25 (t, 4H), 1.54 (m, 4H), 1.33 (m, 4H), 0.95 (t, 6H), 0.23 (s, 9H). ^{13}C NMR (75 MHz, CDCl_3), δ (ppm): 148.0, 133.2, 110.9, 108.5, 106.8, 90.7, 50.6, 29.3, 20.3, 14.0, 0.23. HRMS (FAB): m/z calcd. for $\text{C}_{19}\text{H}_{31}\text{NSi}$, 301.2226; found 301.2228. Elemental analysis: calcd. for $\text{C}_{19}\text{H}_{31}\text{NSi}$, C 75.68, H 10.36, N 4.65; found C 75.93, H 10.48, N 4.66.



Synthesis of (4-ethynyl-phenyl)-dibutyl-amine

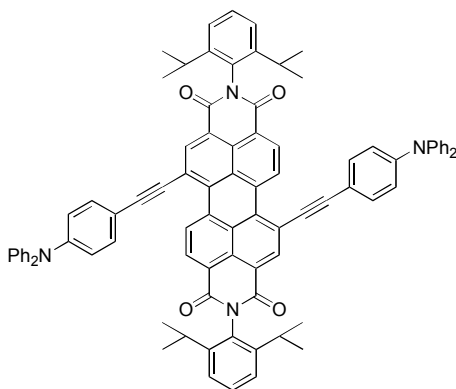
To a solution of dibutyl-[4-(trimethyl-silanylethynyl)-phenyl]-amine (6.9 g, 23 mmol) in a solution of methanol and THF (1:1, v:v) (150 mL) was added an aqueous solution (40 mL) of sodium hydroxide (4.7 g, 118 mmol). The reaction mixture was stirred at room temperature for 21 h. Water was added and the resulting mixture was extracted with ether. The combined organic solution was dried over anhydrous magnesium sulfate and was filtered. The solvent was removed and the residue was purified by column chromatography eluting with 5:95 ethyl acetate/hexane. After removal of solvent, 5.0 g (96%) of a yellow oil was obtained. ^1H NMR (300 MHz, CDCl_3), δ (ppm): 7.32 (d, $J = 9$ Hz, 2H), 6.53 (d, $J = 8.7$ Hz, 2H), 3.26 (t, 4H), 2.95 (s, 1H), 1.55 (quintet, 4H), 1.34 (sextet, 4H), 0.95 (t, 6H). ^{13}C NMR (75 MHz, CDCl_3), δ (ppm): 148.1, 133.3, 110.9, 107.3, 85.0, 74.4, 50.6, 29.3, 20.3, 14.0. HRMS (FAB): m/z calcd. for $\text{C}_{16}\text{H}_{23}\text{N}$ 229.1830; found (M+H) 230.1909. Elemental analysis: calcd. for $\text{C}_{16}\text{H}_{23}\text{N}$ C 83.79, H 10.11, N 6.11; found C 83.52, H 10.36, N 5.85.



Synthesis of compound 2

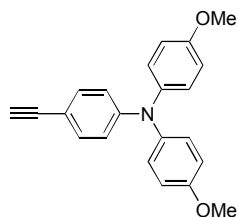
To a solution of *N,N'*-Bis(2,6-diisopropylphenyl)-1,7-dibromoperylene-3,4:9,10-tetracarboxydiimide (0.5 g, 0.57 mmol) in a solution (40 mL) of THF and ethyldiisopropylamine (1:1, v:v) deoxygenated with argon, were added copper(I) iodide (54 mg, 280 μ mol) and tetrakis(triphenylphosphino) palladium(0) (74 mg, 63 μ mol). The mixture was further deoxygenated for 10 min, after which (4-ethynyl-phenyl)-dibutylamine (0.34 g, 1.48 mmol) was added. The reaction was heated at 80 °C under argon for 15 h. After cooling to room temperature, the reaction mixture was poured into 150 mL 2 N HCl solution and was extracted with dichloromethane. The organic phase was dried over anhydrous magnesium sulfate and was filtered. After the solvent was removed, the residue was purified by column chromatography eluting with 1:1 dichloromethane/hexane. After removal of solvent, 0.6 g (89%) of a dark green solid was obtained. ^1H NMR (300 MHz, CDCl_3), δ (ppm): 10.28 (d, $J = 8.1$ Hz, 2H), 8.96 (s, 2H), 8.79 (d, $J = 8.4$ Hz, 2H), 7.51 (triplet, $J = 8.4$ Hz, 6H), 7.36 (d, $J = 7.8$ Hz, 4H), 6.68 (d, $J = 8.7$ Hz, 4H), 3.33 (t, $J = 7.2$ Hz, 8H), 2.79 (m, $J = 6.9$ Hz, 4H), 1.60 (m, $J = 6.3$ Hz, 8H), 1.35 (m, $J = 7.2$ Hz, 8H), 1.19 (dd, $J_1 = 6.75$ Hz, $J_2 = 1.65$ Hz, 24H), 0.97 (t, $J = 7.2$ Hz, 12H). HRMS (FAB): m/z calcd. for $\text{C}_{80}\text{H}_{84}\text{N}_4\text{O}_4$ 1164.6493; found 1164.6481.

Elemental Analysis: calcd. for C₈₀H₈₄N₄O₄ C 82.44, H 7.26, N 4.81; found C 82.25, H 7.16, N 4.75.



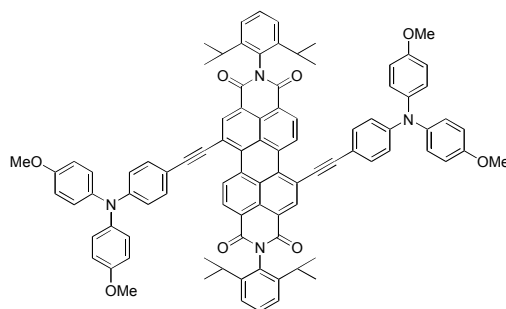
Synthesis of compound 1

To a solution of 1,7-dibromo- *N, N'*-di((2,5-diisopropyl)phenyl)-3,4:9,10-perylenebis(dicarboximide) (0.61 g, 0.70 mmol) in a mixture (1:1, v/v) of THF and ethyldiisopropylamine (50 mL) deoxygenated with nitrogen, were added tetrakis(triphenylphosphino)palladium(0) (73 mg, 63 μ mol), copper(I) iodide (0.182 g, 0.96 mmol) and (4-diphenylaminophenyl) acetylene (0.45 g, 1.67 mmol). The reaction mixture was heated at 80 °C under nitrogen for 24 h. After cooling to room temperature, the mixture was extracted with dichloromethane over 100 mL 2 M HCl solution. The organic solution was dried over anhydrous magnesium sulfate and was filtered. The solution was concentrated. The residue was taken up with silica gel and was purified by column chromatography eluting with 1:1 dichloromethane/hexane. 0.78 g (89%) of a dark solid was obtained. ¹H NMR (300 MHz, CDCl₃), δ (ppm): 10.21 (d, *J* = 8.4 Hz, 2H), 8.97 (s, 2H), 8.77 (d, *J* = 8.4 Hz, 2H), 7.49 (d, *J* = 9.0 Hz, 6H), 7.32 (m, 12H), 7.11 (m, 14H), 2.76 (m, *J* = 6.7 Hz, 4H), 1.18 (d, *J* = 6.6 Hz, 24H). HRMS (FAB): *m/z* calcd. for C₈₉H₆₈N₄O₄ 1244.5241; found 1244.5276. Elemental analysis: calcd. for C₈₉H₆₈N₄O₄, C 84.86, H 5.50, N 4.50; found C 85.21, H 5.52, N 4.46.



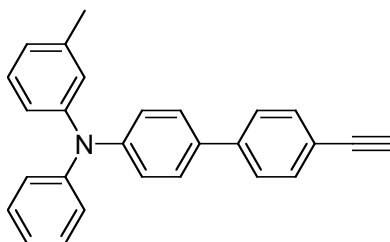
Synthesis of 4-(di(4-methoxyphenyl)amino)-phenyl-acetylene²⁰

To a solution of di(4-methoxyphenyl)amine (0.57 g, 2.5 mmol) and 1-bromo-4-trimethylsilylbenzene (0.61g, 2.4 mmol) in toluene (50 mL) deoxygenated with argon, were added tris(dibenzylideneacetone)dipalladium(0) (43 mg, 47 μ mol), diphenylphosphinoferrocene (57 mg, 0.1 mmol) and sodium *tert*butoxide (0.67 g, 6.8 mmol). The reaction mixture was deoxygenated with nitrogen for 10 min and was heated at 125 °C under argon for 14 h. After cooling to room temperature, the reaction mixture was filtered and was washed with dichloromethane. The solvent was removed and the residue was purified by column chromatography eluting with 1:3 dichloromethane/hexane. After removal of solvent, the compound was dissolved in THF (5 mL) and 1 M tetrabutylammonium fluoride THF solution (10 mL) was added. After the reaction mixture was stirred at room temperature for 3 h, 2N HCl solution (10 mL) was added. The resultant mixture was extracted with dichloromethane. The combined organic solution was dried over anhydrous magnesium sulfate and was filtered. The solvent was removed and the residue was purified by column chromatography eluting with 1:3 dichloromethane/hexane. After removal of solvent, 0.36 g (42%) of a greenish sticky liquid was obtained. ¹H NMR (300 MHz, CDCl₃): δ (ppm), 7.27 (m, $J = 8.7$ Hz, 2H), 7.06 (m, $J = 8.7$ Hz, 4H), 6.82 (m, 6H), 3.80 (s, 6H), 2.99 (s, 1H). ¹³C NMR (75 MHz, CDCl₃): δ (ppm), 156.3, 149.2, 140.1, 132.9, 127.1, 118.9, 114.8, 112.5, 84.3, 75.5, 55.5.



Synthesis of compound 3

To a mixture of 1,7-dibromo-*N,N'*-di((2,5-diisopropyl)phenyl)-3,4:9,10-perylenebis(dicarboximide) (0.256 g, 29 μmol), 4-(di(4-methoxyphenyl)amino)-phenylacetylene (0.34 g, 1.0 mmol) in a mixture (1:1, v/v) of THF and diethyl-*isopropyl*amine (40 mL) deoxygenated with argon, were added tetrakis(triphenylphosphino)palladium(0) (34 mg, 29 μmol) and copper (I) iodide (81 mg, 43 μmol). The reaction mixture was heated at 80 °C under argon for 18 h. After cooling to room temperature, the reaction mixture was poured into 2N HCl solution (50 mL) and was extracted with dichloromethane. The organic solution was dried over anhydrous magnesium sulfate and was filtered. The solvent was removed and the residue was taken up with silica gel and was purified by column chromatography eluting with 1:1 dichloromethane/hexane. After removal of solvent, 0.25 g (62%) of a dark blue solid was obtained. ^1H NMR (300 MHz, CDCl_3): δ (ppm), 10.23 (d, $J = 8.1$ Hz, 2H), 8.97 (s, 2H), 8.77 (d, $J = 8.1$ Hz, 2H), 7.45 (m, 12H), 7.13 (bs, 8H), 6.89 (d, 10H), 3.82 (s, 12H), 2.78 (m, $J = 6.6$ Hz, 4H), 2.19 (d, 24H). HRMS (FAB): m/z calcd. for $\text{C}_{92}\text{H}_{76}\text{N}_4\text{O}_8$ 1364.5663; found 1364.5690. Elemental analysis: calcd. for $\text{C}_{92}\text{H}_{76}\text{N}_4\text{O}_8$, C 80.92, H 5.61, N 4.10; found C 80.84, H 5.64, N 4.13.



Synthesis of (4'-ethynyl-biphenyl-4-yl)-phenyl-*m*-tolyl-amine

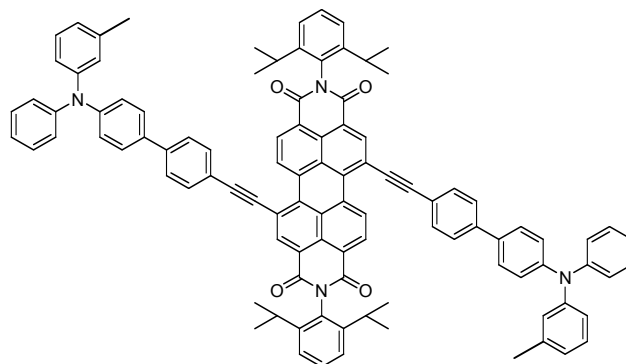
To a dry ampoule was added (4'-bromo-biphenyl-4-yl)-phenyl-*m*-tolyl-amine (2.02 g, 4.86 mmol) under nitrogen. Dichloro-bis(cyanophenyl) palladium (II) (57 mg, 0.15 mmol), copper (I) iodide (57 mg, 0.30 mmol) and piperidine (15 mL) were added. After the mixture was sparged with nitrogen for 10 min, tri-*tert*butylphosphine (0.59 g 10%wt hexane solution, 0.30 mmol) was added. The mixture was further deoxygenated for 15 min. Trimethylsilylacetylene (1.0 mL, 7.08 mmol) was added and the ampoule was capped. The reaction mixture was heated at 50 °C for 5 h and poured into 2 M HCl solution (75 mL) and was extracted with ethyl acetate. The combined organic solution was washed with 2 M HCl solution (50 mL) and water (100 mL), dried over anhydrous magnesium sulfate and filtered. After removal of solvent, the residue was taken up with silica gel and was purified by column chromatography eluting with hexane. After removal of solvent, the solid was recrystallized from ethanol.

To a solution of the obtained phenyl-*m*-tolyl-(4'-trimethylsilanylethynyl-biphenyl-4-yl)-amine (1.90 g, 4.40 mmol) in THF (10 mL) was added 1.0 M TBAF THF solution (10 mL). The resulting mixture was stirred at room temperature under nitrogen for 3 h. After 2 N HCl solution (5 mL) was added, the mixture was further stirred for 10 min and was extracted with dichloromethane. The organic solution was dried over anhydrous magnesium sulfate and was filtered. After the solvent was removed, the residue was recrystallized from ethyl acetate. 1.26 g (80%) of a brown solid was obtained. ¹H NMR (500 MHz, CDCl₃): δ (ppm): 7.52 (s, 4H), 7.44(d, *J* = 8.5 Hz, 2H), 7.25 (t, *J* = 8.0 Hz, 2H), 7.15 (t, *J* = 8.0 Hz, 1H), 7.10 (m, 4 H), 7.02 (t, *J* = 7.5 Hz), 6.94 (s, 1H), 6.91 (d, *J* = 8.0 Hz, 1H), 6.85 (d, *J* = 7.5 Hz, 1H), 3.09 (s, 1H), 2.26 (s, 3H). ¹³C NMR (125 MHz, CDCl₃): δ (ppm): 147.6, 147.4, 147.3, 140.9, 139.1, 133.4, 132.4,

129.2, 129.0, 127.5, 126.2, 125.3, 124.4, 124.0, 122.9, 121.8, 120.2, 83.7, 77.6, 21.5.

HRMS (EI): m/z calcd. for $C_{27}H_{21}N$ 359.1674; found 359.1661. Elemental Analysis:

calcd. for $C_{27}H_{21}N$, C 90.21, H 5.89, N 3.90; found C 89.94, H 5.88, N 3.90.



Synthesis of compound 4

1,7-Dibromo-bis(2,6-diisopropylphenyl)-3,4,9,10-tetracarboxy perylene diimide (0.22 g, 0.25 mmol) and (4'-Ethynyl-biphenyl-4-yl)-phenyl-*m*-tolyl-amine (0.22 g, 0.61 mmol) were dissolved in a mixture of toluene (10 mL), dioxane (5 mL) and diisopropyl-ethyl amine (10 mL). The solution was sparged with nitrogen and dichlorobis(cyanophenyl) palladium(II) (0.02 g, 0.05 mmol) and copper(I) iodide (0.01 g, 0.05 mmol) were added and the resulting mixture further sparged with nitrogen for 10 min. 10% (wt) tri(*tert*butyl)phosphine hexane solution (0.21 g, 0.1 mmol) was added. The reaction mixture was heated at 80 °C for 20 h. After cooling to room temperature, the reaction was diluted with chloroform and was washed over 2 N HCl solution. The organic layer was separated, dried over anhydrous magnesium sulfate and was filtered. The solvent was removed and the residue was purified by column chromatography eluting with chloroform. After removal of solvent, 0.27 g (76%) of a dark purple solid was obtained. 1H NMR (500 MHz, $CDCl_3$): δ (ppm): 10.25 (d, $J = 8.0$ Hz, 2H), 9.03 (s, 2H), 8.85 (d, $J = 8.5$ Hz), 7.73 (d, $J = 8.5$ Hz, 4H), 7.68 (d, $J = 8.5$ Hz, 4H), 7.52 (m, 6H), 7.37 (d, $J = 8.0$ Hz, 4H), 7.27 (m, 4H), 7.15 (m, 10H), 7.04 (t, $J = 8.0$ Hz, 2H), 6.96

(s, 2H), 6.93 (d, $J = 8.5$ Hz, 2H), 6.87 (d, $J = 7.5$ Hz, 2H), 2.79 (m, 4H), 2.27 (s, 6H), 1.20 (d, 24H). HRMS (MALDI): m/z calcd. for $C_{102}H_{80}N_4O_4$: 1424.6180; found: 1424.6104. Elemental Analysis: calcd. for $C_{102}H_{80}N_4O_4$, C 85.93, H 5.66, N 3.93; found C 85.88, H 5.66 N 3.91.

5.8 References

1. (a) Marcus, R. A. *J. Chem. Phys.* **1956**, *24*, 966. (b) Marcus, R. A. *J. Chem. Phys.* **1965**, *43*, 679. (c) Marcus, R. A. *Angew. Chem. Int. Ed. Engl.* **1993**, *32*, 1111. (d) Weller, A. *Z. Phys. Chem. Neue Folge* **1982**, *133*, 93.
2. Förster, T. *Discuss. Faraday Soc.* **1959**, *27*, 7.
3. (a) Rademacher, A.; Märkle, S.; Langhals, H. *Chem. Ber.* **1982**, *115*, 2927. (b) Feiler, L.; Langhals, H.; Polborn, K. *Liebigs Ann.* **1995**, 1229. (c) Quante, H.; Geerts, Y.; Müllen, K. *Chem. Mater.* **1997**, *9*, 495. (d) Lee, S. K.; Zu, Y.; Herrmann, A.; Geerts, Y.; Müllen, K.; Bard, A. J. *J. Am. Chem. Soc.* **1999**, *121*, 3513. (e) Ahrens, M. J.; Fuller, M. J.; Wasielewski, M. R. *Chem. Mater.* **2003**, *15*, 2684-2686. (f) Würthner, F. *Chem. Comm.* **2004**, 1564-1579.
4. (a) O'Neil, M. P.; Niemczyk, M. P.; Svec, W. A.; Gosztda, D.; Gaines III, G. L.; Wasielewski, M. R. *Science* **1992**, *257*, 63-66. (b) Wasielewski, M. R. *Chem. Rev.* **1992**, *92*, 435-461. (c) Serin, J. M.; Brousmiche, D. W.; Fréchet, J. M. J. *Chem. Comm.* **2002**, 2605-2607. (d) Wolf-Klein, H.; Kohl, C.; Müllen, K.; Paulsen, H. *Angew. Chem. Int. Ed.* **2002**, *41*, 3378-3380. (e) van der Boom, T.; Hayes, R. T.; Zhao, Y.; Bushard, P. J.; Weiss, E. A.; Wasielewski, M. R. *J. Am. Chem. Soc.* **2002**, *124*, 9582-9590. (f) Ahrens, M. J.; Sinks, L. E.; Rybtchinski, B.; Liu, W.; Jones, B. A.; Giaimo, J. M.; Gusev, A. V.; Goshe, A. J.; Tiede, D. M.; Wasielewski, M. R. *J. Am. Chem. Soc.* **2004**, *126*, 8284-8294. (g) Li, X.; Sinks, L. E.; Rybtchinski, B.; Wasielewski, M. R. *J. Am. Chem. Soc.* **2004**, *126*, 10810-10811. (h) Würthner, F.; Chen, Z.; Hoeben, F. J. M.; Osswald, P.; You, C.-C.; Jonkheijm, P.; v. Herrikhuyzen, J.; Schenning, A. P. H. J.; van der Schoot, P. P. A. M.; Meijer, E. W.; Beckers, E. H. A.; Meskers, S. C. J.; Janssen, R. A. J. *J. Am. Chem. Soc.* **2004**, *126*, 10611-10618.
5. Zhao, Y.; Wasielewski, M. R. *Tetrahedron Lett.* **1999**, *40*, 7047-7050.
6. Lukas, A. S.; Zhao, Y.; Miller, S. E.; Wasielewski, M. R. *J. Phys. Chem. B* **2002**, *106*, 1299-1306.
7. Giaimo, J. M.; Gusev, A. V.; Wasielewski, M. R. *J. Am. Chem. Soc.* **2002**, *124*, 8530-8531.
8. Fuller, M. J.; Sinks, L. E.; Rybtchinski, B.; Giaimo, J. M.; Li, X.; Wasielewski, M. R. *J. Phys. Chem. A* **2005**, *109*, 970-975.
9. Rybtchinski, B.; Sinks, L. E.; Wasielewski, M. R. *J. Am. Chem. Soc.* **2004**, *126*, 12268-12269.
10. Coakley, K. M.; McGehee, M. D. *Chem. Mater.* **2004**, *16*, 4533-4542.

11. Grätzel, M. *Prog. Photovolt. Res. Appl.* **2000**, *8*, 171-185.
12. Sonogashira, K.; Tohda, Y.; Hagihara, N. *Tetrahedron Lett.* **1975**, *16*, 4467
13. Böhm, A. ; Arms, H.; Henning, G.; Blaschka, P. DE 19547210 (US Patent 6184378), **2001**.
14. Rohr, U.; Kohl, C.; Müllen, K.; van de Craats, A.; Warman, J. *J. Mater. Chem.* **2001**, *11*, 1789-1799.
15. Hofkens, J.; Vosch, T.; Maus, M.; Köhn, F.; Cotlet, M. ; Weil, T. ; Herrmann, A. ; Müllen, K.; Schryver, F.C. *Chem. Phys. Lett.* **2001**, *333*, 255.
16. Jones, B. A.; Ahrens, M.; Yoon, M.-H.; Facchetti, A.; Marks, T. J.; Wasielewski, M. R. *Angew. Chem. Int. Ed.* **2004**, *43*, 6363-6366.
17. Hagfeldt, A.; Grätzel, M. *Acc. Chem. Res.* **2000**, *33*, 269-277.
18. Meier, H.; Gerold, J.; Kolshorn, H.; Baumann, W.; Bletz, M. *Angew. Chem. Int. Ed.* **2002**, *41*, 292-295.
19. Lee, S. K.; Zu, Y.; Herrmann, A.; Geerts, Y.; Müllen, K.; Bard, A. J. *J. Am. Chem. Soc.* **1999**, *121*, 3513-3520.
20. Jones, S. C. ; Coropceanu, V. ; Barlow, S. ; Kinnibrugh, T. ; Timofeeva, T. ; Brédas, J.-L. ; Marder, S. R. *J. Am. Chem. Soc.* **2004**, *126*, 11782-11783.

CHAPTER 6

CONCLUSIONS AND OUTLOOK

The research described in this thesis was focused on perylene-based materials. The objective of the research was to develop organic semiconducting materials that can be potentially used in organic electronics and optoelectronics. The research can be divided into two parts: (1) discotic liquid crystals as charge transport materials with perylene or coronene diimides as the aromatic cores and (2) charge-transfer chromophores with perylene diimide moiety as the electron acceptor.

In the project of discotic liquid crystals as charge transport materials, perylene diimide and coronene diimide discotic liquid crystals were designed, synthesized and characterized; their charge carrier mobilities were determined by SCLC method (by the Kippelen group). All of these materials can form columnar discotic liquid crystals over a wide temperature range; the two perylene diimides form liquid crystals at room temperature and most of the coronene diimides form liquid crystals at temperatures slightly higher than room temperature. Most of these discotic liquid crystals show high charge carrier mobilities. Mobilities as high as $2.2 \text{ cm}^2/\text{Vs}$ were found in one of the two perylene diimides; mobilities up to $6.6 \text{ cm}^2/\text{Vs}$ were found in one of the coronene diimides.

In order to gain understanding of the relationship between structural properties and charge transport properties of discotic liquid crystals, we examined the effect of the size of the aromatic core and the side groups on the charge transport properties of discotic

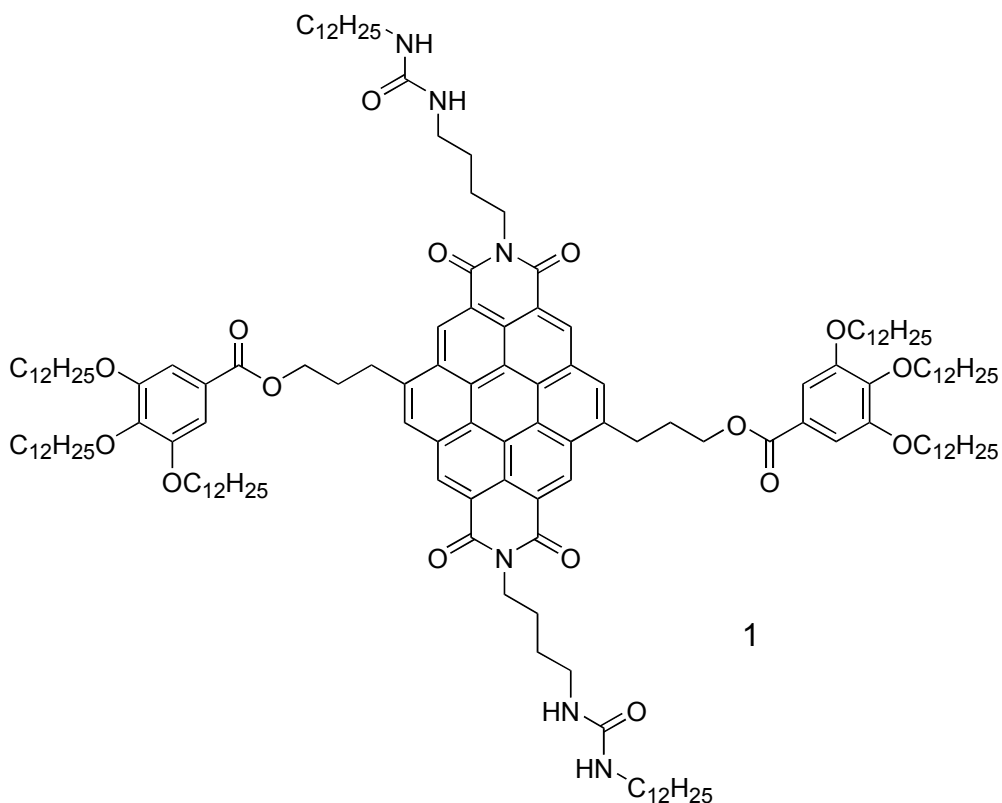
liquid crystals. The effect of the structural properties on the charge transport properties in the discotic liquid crystals can be addressed at two different levels.

At the material level (strictly speaking, on the micrometer scale, as indicated by the size of the optical textures of the liquid crystals that the liquid crystal domain size is on the micrometer scale), the ordering of the mesophase has an important effect on the charge transport properties. As evidenced mainly from XRD, for the perylene diimides, **PDI2** forms a more ordered mesophase and displays a higher charge carrier mobility than **PDI1**; for the coronene diimides described in Chapter 3, compound **6b** has the largest number of peaks in the low angle region of XRD and exhibits the highest charge carrier mobility among the four coronene diimides studied in Chapter 3; the mesophase order of the coronene diimide is further enhanced by incorporation of binary side chains and **CDI-F7** shows improved charge carrier mobility, compared to **CDI-C8**. We should realize that other factors (*vide infra*) need to be considered when trying to completely explain the charge transport behavior; however, the increase in the mesophase order is surely expected to lead to improved charge carrier mobilities. The ordering of the mesophase is the result of the interplay of the side chains and the aromatic core of discotic liquid crystals. From perylene diimides to coronene diimides, as the size of the aromatic core is increased, the mesophase changes from disordered columnar liquid crystals to ordered columnar liquid crystals. The presence of binary side chains can improve the mesophase order through fluorophobic interactions between the perfluoroalkyl groups and the hydrocarbon moieties (aromatic core and alkyl side groups).

At the molecular level, the charge carrier mobility is related to the reorganization energy and the intermolecular transfer integral. It remains unclear how the increase in the core size on going from perylene diimides to coronene diimides could affect the

reorganization energy. The intermolecular transfer integral is related to the distance and the overlap of neighboring discs within the same column. For ordered mesophases, the intermolecular distance can be experimentally probed by XRD. However, it is still a challenging issue as how to probe the overlap of neighboring discs by experimental techniques. Quantum calculation on these factors can help gain insightful understanding of the charge transport properties at the molecular level.

In order to force the molecules to have a large molecular overlap, anchoring points can be synthetically introduced into the side chains of the molecules through hydrogen bonding. Work has been initiated to try to reduce the rotational and lateral disorders of discotic liquid crystals by synthesizing a coronene diimide derivative with urea groups (compound 1). Hydrogen bonding is expected to form between urea groups of neighboring discs and can effectively reduce the rotational and lateral disorders of the discs. Such a design could be a meaningful way to experimentally test the effect of the rotational and lateral disorders on the charge carrier mobility, compared to compounds without hydrogen bonding.



In addition, material processing of discotic liquid crystals is an important aspect for practical applications. From the optical textures, we know that these high-mobility liquid crystals form liquid crystalline polydomains, rather than homeotropic or homogeneous monodomains. Therefore, alignment of discotic liquid crystals is an important research direction in order to control the orientation of the discs to improve the efficiency of the devices employing discotic liquid crystals.

In the project of charge-transfer chromophores, we have demonstrated that absorption into the NIR can be realized by a combination of electron-transfer process and conjugation extension. Chromophores **1 - 3** have strong absorption in the UV, visible and NIR region. Also, the charge recombination process of these chromophores is

substantially longer, compared to the charge-transfer process. These properties make these chromophores promising candidates for solar cell applications.

To continue the work on the charge-transfer chromophores, we can replace the 2,6-di(isopropyl)phenyl group used in chromophores **1** – **3** with tri(dodecyloxy)phenyl group (for example, compound **2**) to encourage self-assembly such that the chromophores can stack into columns. Taking advantage of the long-lived charge-separation state, we hope that the separated charges can move along the columns in the opposite directions; the electrons can move along the perylene diimide moiety and the holes can move along the amine moiety. Such bipolar columns can be potentially used as both light-harvesting and charge transport materials in solar cells.

